

THREE-DIMENSIONAL CHARACTERIZATION OF INHERENT AND INDUCED
SAND MICROSTRUCTURE

A Thesis
Presented to
The Academic Faculty

by

Xuan Yang

In Partial Fulfillment
of the Requirements for the Degree
Doctor of Philosophy in Civil and Environmental Engineering

Georgia Institute of Technology
December 2005

To my parents and family

Dad, thanks for working hard and making a perfect life for our family. I wish I had as much wisdom as you have and could be as successful as you are. Mom, thanks for your sacrifices and support to the whole family.

ACKNOWLEDGEMENTS

These past four and a half years have been filled with many challenges and I have been fortunate to have the support that allowed me to complete this work. I find myself extremely lucky to have the opportunity to have worked with my advisor Dr. J. David Frost. I enjoyed every moment of our discussions and certainly benefited a lot from his academic insight to complicated problems. His sound advice, encouragement and patience helped me build up my research skills and overcome many challenges and frustrations. He was always supportive in a respectful way whenever help was needed. I also appreciate his willingness to work with me on all issues, both personal and related to this research. He inspired and influenced me in many ways. I believe that the things that I learned from him will benefit me over the course of my lifetime.

I want to gratefully acknowledge my committee members, Dr. Arun N.Gokhale, Dr. Paul W. Mayne, Dr. Glenn J. Rix and Dr. James Tsai. I am thankful to Dr. Brent Lindquist of University of Stony Brooke for allowing me to use their research software 3DMA and providing timely assistance and insightful discussions.

I am indebted to Mr. Ken Thomas, Mr. Mike Sorenson, Mr. Leo DiPierro (Allied High Tech Products, Inc.), Mr. Jesse Lockwood (Allied High Tech Products, Inc.) and Mr. Gary Liechty (Allied High Tech Products, Inc.) for their assistance in conducting experimental works. I also want to thank Mr. Clarence C. Chan for helping me with solving triaxial test device issues. I'm grateful to Mr. Didier Contis and all the ISG members for processing my computer service requests in a timely manner and helping me

with patience. I am also thankful to the following researchers for their help and suggestions: Mr. Patrick Guerin (VayTek, Inc.), Dr. Jean-Francois Delerue, Dr. William D. Carlson (University of Texas, Austin), and Dr. Nicholas Petford (U.K.).

I would like to thank all the past and present members of geotechnical society of Georgia Tech for their encouragement and help, especially the members of Geomaterial Surface and Structure Characterization Lab: Andrew, Catherine, DuHwan, Greg and Matt. Bade, thanks for your thoughtful words and great friendship; Chien-Tai, thanks for teaching me so many things when I started my research in the lab and answering all my questions with patience even though you were thousands of miles away; Chien-Chang, Deh-Jeng and Jin-Young, thanks for providing help whenever I asked; DuHwan, Mehmet, and Topraj, thanks for the friendship in the office and all of the talks, encouragement, laughs and help; Matt, thanks for helping me whenever you could, answering my questions and sharing your knowledge; Ruiting and Tianyi, thanks for always being warm-hearted to me and I am grateful for all of your help during my stay in Atlanta.

I would also like to thank my good friends since high school and college, especially Dongning, Qing, Song, and Xin, who always stand by my side even though we do not live in the same city or dormitory any more. I also want to thank my older brother, Ming, for the happy childhood we shared.

Finally, I want to thank my husband, Jie, for your love...

TABLE OF CONTENTS

DEDICATION	ii
ACKNOWLEDGEMENTS	iii
LIST OF TABLES	viii
LIST OF FIGURES	x
SUMMARY	xvi
CHAPTER I INTRODUCTION	1
1.1 Motivation	1
1.2 Research Scope	2
1.3 Organization of the Dissertation	3
CHAPTER II LITERATURE REVIEW	4
2.1 Introduction	4
2.2 Specimen Preparation	5
2.2.1 Introduction	5
2.2.2 Triaxial Test Specimen Preparation	5
2.2.3 Specimen Preservation	7
2.3 Three-Dimensional Image Collection	8
2.3.1 Introduction	8
2.3.2 Non-destructive Method	9
2.3.3 Destructive Method	11
2.4 Microstructural Analysis of Triaxial Test Specimens	16
2.4.1 Introduction	16
2.4.2 2-D Image Analysis on Triaxial Test Specimens	17
2.4.3 Available 3-D Analysis Methods	19
CHAPTER III EXPERIMENTAL DEVELOPMENTS AND TECHNIQUES	25
3.1 Introduction	25
3.2 Materials	25
3.3. Triaxial Test Specimen Preparation and Preservation	27
3.3.1 Air Pluviation	27
3.3.2 Moist Tamping	29
3.3.3 Triaxial Test and Sample Preservation	31
3.4 Serial Grinding	34
3.4.1 Sample Position and Size	34
3.4.2 Serial Grinding	38

3.4.3 Image Capture and Mosaic Generation	41
3.5 Three-Dimensional Reconstruction	46
3.5.1 Alignment	46
3.5.2 Reconstruction	46
CHAPTER IV SIMULATED STRUCTURE STUDY	51
4.1 Introduction	51
4.2 Introduction to 3DMA Software Package	51
4.3 Medial Axis Analysis on Simple Cubic Packing	54
4.3.1 Structure Information	54
4.3.2 Medial Axis Analysis on SCP	55
4.4 Medial Axis Analysis on Face-Centered Cubic Packing	66
4.4.1 Structure Information	66
4.4.2 Medial Axis Analysis on FCP	68
4.5 Two-Dimensional Analysis of the Simulated Structures	73
4.5.1 Two-Dimensional Pore and Throat Analysis	73
4.5.2 Local Void Ratio Distribution Analysis	76
4.5.3 2-D Pore Size and Throat Size Analysis of SCP and FCP	77
4.5.4 Local Void Ratio Distribution of SCP and FCP	79
4.6 3-D Particle Size Analysis	82
4.6.1 Introduction	82
4.6.2 3-D Grain Size of SCP	82
CHAPTER V 2-D CHARACTERIZATION OF SPECIMEN MICROSTRUCTURE	87
5.1 Introduction	87
5.2 Local Void Ratio	89
5.2.1 Introduction	89
5.2.2 Local Void Ratio Measurement	89
5.2.3 Statistical Analysis	95
5.3 2-D Pore Size Distributions	100
5.3.1 Introduction	100
5.3.2 Pore Size Measurement	100
5.3.3 Statistical Modeling of Pore Size Distribution	104
5.4 Throat Size Distributions	107
5.4.1 Introduction	107
5.4.2 2-D Throat Size Measurement	107
5.5 Effects of Preparation Method and Shearing-Induced Evolution of Structure	110
5.5.1 Effects of Preparation Method	110
5.5.2 Shearing-Induced Structure Evolution	110
CHAPTER VI 3-D CHARACTERIZATION OF SPECIMEN MICROSTRUCTURE	112
6.1 Introduction	112
6.2 Visualization of Particles and Pores	113
6.3 Void Ratio	127

6.4 3-D Throat Size	128
6.5 3-D Pore Size	131
6.6 Tortuosity	135
6.6.1 Tortuosity Measurement	135
6.6.2 Size Analysis	135
6.6.3 Anisotropy of Tortuosity	138
6.6.3 Effects of Dilation Cycles on Tortuosity Measurement	141
6.7 Effects of Preparation Methods and Shearing on Microstructure	142
CHAPTER VII SUMMARY, CONCLUSIONS AND RECOMMENDATIONS	144
7.1 Summary and Conclusions	144
7.2 Recommendations	148
REFERENCES	150

LIST OF TABLES

Table 2.1 Porous Structures Parameters	21
Table 3.1 Index Properties of ASTM Graded Sand	27
Table 3.2 Moist Tamping Specimen Layer Density Information	30
Table 3.3 Four Specimens.....	33
Table 3.4 Polishing Procedure Using MultiPrep™ System.....	40
Table 3.5 Information of Three-Dimensional Structure	45
Table 4.1 SCP Structure Information.....	54
Table 4.2 3DMA Measurements of SCP	57
Table 4.3 Comparison between Theoretical Values and 3DMA measurements	58
Table 4.4 Mean, Standard Deviation and Coefficient of Variation of Tortuosity for Each Sub-Volume	63
Table 4.5 Structure Information of FCP	67
Table 4.6 Internal Pore Size Information from 3DMA.....	70
Table 4.7 Comparison between Theoretical Values and 3DMA Measurements.....	70
Table 4.8 SCP Particle Size Measurement Results.....	83
Table 4.9 Comparison between Theoretical Values and 3DMA Measurement Results on Particle Size	85
Table 5.1 Gamma and Lognormal Distribution Parameters of Local Void Ratio Distributions of the Four Samples	100
Table 5.2 2-D Pore Diameter (micron).....	103
Table 5.3 2-D Pore Diameter Statistical Parameters	107
Table 5.4 Statistical Parameters of 2-D Pore Throat Diameter (micron)	109

Table 6.1 Porosity Information of Four Samples.....	127
Table 6.2 Mean, Standard Deviation, and Coefficient of Variations of 3-D Pore Diameter of Four Samples	134
Table 6.3 Mean, Standard Deviation and Coefficient of Variation of R_L of Sub-Volume of Size 230x1100x230 Voxels	138
Table 6.4 Mean, Standard Deviation and Coefficient of Variation of R_L of Sub-Volume with Different Length (Width=1100 Pixel; Height=230 Pixel).....	138
Table 6.5 Mean Tortuosity.....	140
Table 6.6 Standard Deviation of Tortuosity	140
Table 6.7 Tortuosity Comparison	142

LIST OF FIGURES

Figure 2.1 Flow Chart of Typical Serial Sectioning Process.....	12
Figure 2.2 3-D Reconstructed Volume of Naturally Aged Composites with 10% Weight Fraction Si and Larger Particle Size (Li et al, 1998)	15
Figure 2.3 Surface rendering of limestone sample, after binary 3-D grow/shrink filtering and 3-D average filtering. Dimensions 341x431x180 voxels=2.90x3.66x1.53 cm, 8 bits per voxel, approximately 26.5 Mbyte (Marschallinger, 1998)	15
Figure 3.1 Grain Size Distribution of ASTM Graded Sand.....	26
Figure 3.2 Air Pluviation System (After Jang, 1997).....	28
Figure 3.3 Moist Tamping System (After Park, 1999).....	29
Figure 3.4 Specimen Drying System for Epoxy Impregnation (After Jang, 1997)	30
Figure 3.5 Stress Strain Relationship of Air Pluviated Specimen	31
Figure 3.6 Stress Strain Relationship of Moist Tamped Specimen	32
Figure 3.7 Epoxy Impregnation System for Specimen Preservation (After Jang, 1997) .	33
Figure 3.8 Schematic Sketch of the Coupon Position in Specimen AP0/MT0 and AP14	35
Figure 3.9 Schematic View of the Coupon Cut from Specimen MT14.....	35
Figure 3.10 Estimate Shear Band Position in the Coupon.....	36
Figure 3.11 Sample Block in Mounting Cup.....	37
Figure 3.12 Cylindrical and Conical Holes Drill Pattern.....	37
Figure 3.13 Illustration of Removal Thickness Calculation with Conical Holes	38
Figure 3.14 Dial Indicator and Remote Cable for Removal Thickness Measurement	40
Figure 3.15 Dimensions of the Holding Fixture	42
Figure 3.16 Holding Fixture to Ensure Correct Alignment of Specimen	43

Figure 3.17 Sketch of Mosaic Pattern.....	44
Figure 3.18 Illustration of Stitching of Four Neighboring Images	44
Figure 3.19 3-D Dimension Information of the Sample	45
Figure 3.20 An Example of the 3D Reconstructed Structure	47
Figure 3.21 Sub-volume of the Sample and Extracted Structures of Particles and Pores	48
Figure 3.22 Comparison between Different z Resolutions.....	50
Figure 4.1 Flow Chart of Medial Axis Analysis in 3DMA	53
Figure 4.2 3-D SCP Structure	54
Figure 4.3 Medial Axis of an SCP Structure	55
Figure 4.4 Throats of the Pore Space in an SCP Structure	56
Figure 4.5 Medial Axis and Throats of SCP.....	56
Figure 4.6 A Unit Pore Structure in SCP	57
Figure 4.7 3-D Pore Size Distribution of SCP	59
Figure 4.8 3-D Throat Size Distribution of SCP.....	59
Figure 4.9 Illustration of Path Length and Tortuosity Measurement in 3DMA	60
Figure 4.10 Sub-Volumes of SCP (a) Sub-Volumes of Same Size: 50 x 250 x 250; (b) Sub-Volumes of Various Length ($L \times 250 \times 250$; $L=i*50$, $i=1 \dots 5$).....	62
Figure 4.11 Mean Tortuosity for Each Sub-Volume of Size 50 x 250 x250	62
Figure 4.12 Mean Shortest Path Length for Each Sub-Volume of Various Lengths (50, 100, 150, 200 and 250 Pixel)	63
Figure 4.13 Mean Tortuosity for Each Sub-Volume of Various Lengths (50, 100, 150, 200 and 250 Pixel)	63
Figure 4.14 Coefficient of Variation of Tortuosity for Each Sub-Volume of Various Lengths (50, 100, 150, 200 and 250 Pixel).....	64
Figure 4.15 Shortest Path Characterization in SCP (a) Path Length Distribution for Shortest Paths of SCP; (b) Tortuosity Distribution for Shortest Paths of SCP.....	65

Figure 4.16 Shortest Paths in SCP	66
Figure 4.17 3-D Structure of FCP and Unit Information.....	67
Figure 4.18 Medial Axis of an FCP Structure	68
Figure 4.19 Throats of the Pore Space in FCP.....	69
Figure 4.20 Medial Axis and Throats of a Unit FCP Cell	69
Figure 4.21 3-D Pore Size Distribution of FCP	70
Figure 4.22 3-D Throat Size Distribution of FCP.....	71
Figure 4.23 Shortest Paths between Two Faces in FCP	72
Figure 4.24 Shortest Path and Tortuosity Characterization in FCP (a) Path Length Distribution for Shortest Paths of FCP; (b) Tortuosity Distribution for Shortest Paths of FCP	73
Figure 4.25 Illustration of 2-D Pore and Throat Calculation.....	75
Figure 4.26 Determination of Local Void Ratio Distribution Using Oda’s Method (After Jang, 1999).....	76
Figure 4.27 2-D Pore Size Distribution for SCP and FCP.....	78
Figure 4.28 2-D Throat Size Distribution of SCP and FCP.....	78
Figure 4.29 Example 2-D Slice Images of SCP and FCP (a) An Example 2-D Slice Image of SCP; (b) An Example 2-D Slice Image of FCP.....	79
Figure 4.30 Local Void Ratio Distribution of SCP (a) Local Void Ratio Distribution of SCP; (b) Solid Area Weighted Local Void Ratio Distribution of SCP	80
Figure 4.31 Local Void Ratio Distribution of FCP (a) Local Void Ratio Distribution of FCP; (b) Solid Area Weighted Local Void Ratio Distribution of FCP	81
Figure 4.32 Medial Axis of the Particle Space in SCP	83
Figure 4.33 A Unit of SCP (red: throats of a particle; purple: surrounded pore space) ...	84
Figure 4.34 Individual Particle Visualization	84
Figure 4.35 Particle Size Distribution of SCP	85

Figure 4.36 Visualization of Particle Size in SCP	86
Figure 5.1 Void Ratio of an ASTM Graded Sand Image	88
Figure 5.2 Local Void Ratio Distribution of AP0.....	90
Figure 5.3 Local Void Ratio Distribution of j18 (Air-pluviated, unsheared) (Jang, 1997)	90
Figure 5.4 Local Void Ratio Distribution of AP14.....	91
Figure 5.5 Local Void Ratio Distribution of j30 (Air-pluviated, sheared) (Jang, 1997) ..	91
Figure 5.6 Local Void Ratio Distribution of MT0.....	92
Figure 5.7 Local Void Ratio Distribution of m11 (Moist-tamped, unsheared) (Park, 1999)	92
Figure 5.8 Local Void Ratio Distribution of MT14.....	93
Figure 5.9 Local Void Ratio Distribution of m18 (Moist-tamped, Sheared) (Park, 1999)93	
Figure 5.10 Mean Local Void Ratio vs. Standard Deviation of Local Void Ratio of Air- Pluviated and Moist-Tamped Specimens.....	94
Figure 5.11 Mean Local Void Ratio vs. Standard Deviation of Local Void Ratio of Air- Pluviated and Moist-Tamped Specimens During Axial Compression Test	95
Figure 5.12 Relationship between Mean Local Void Ratio and Entropy	96
Figure 5.13 Evaluation of Local Void Ratio Distribution Models Using Space of Pearson's Probability Distributions (after Pearson and Hartley, 1972).....	97
Figure 5.14 2-D Pore Diameter Distribution of AP0 and MT0	101
Figure 5.15 Comparison of 2-D Pore Diameter Distribution of AP0 and AP14	102
Figure 5.16 Comparison of 2-D Pore Diameter Distribution of MT0 and MT14	102
Figure 5.17 Mean Pore Size vs. Standard Deviation of 2-D Pore Diameter	104
Figure 5.18 Cumulative Probability of the Actual Distribution of 2-D Pore Diameter of AP0 and the Fitted Lognormal Distribution	105
Figure 5.19 Evaluation of Pore Diameter Distribution Models Using Space of Pearson's Probability Distributions (after Pearson and Hartley, 1972)	105

Figure 5.20 2-D Throat Diameter Distributions of AP0 and MT0	108
Figure 5.21 2-D Throat Diameter Distributions of AP0 and AP14	108
Figure 5.22 2-D Throat Size Distribution of MT0 and MT14.....	109
Figure 6.1 Illustration of the View Locations of Particles in Figures 6.2 to 6.7.....	114
Figure 6.2 Particle 1	115
Figure 6.3 Particle 2.....	116
Figure 6.4 Particle 3.....	117
Figure 6.5 Particle 4.....	118
Figure 6.6 Particle 5.....	119
Figure 6.7 Particle 6.....	120
Figure 6.8 Observations of Pore Structure 1.....	122
Figure 6.9 Front Views of Pore Structure 1 at Different Depths.....	123
Figure 6.10 Observations of Pore Structure 2.....	124
Figure 6.11 Front Views of Pore Structure 2 at Different Depths.....	125
Figure 6.12 Visualization of Pore Structure and Medial Axis (a) Visualization of a Single Pore Body and Medial Axis from 3DMA; (b) Visualization of Medial Axis of a Single Pore Body from 3DMA	126
Figure 6.13 2-D and 3-D Void Ratio of Four Samples AP0, AP14, MT0 and MT14....	127
Figure 6.14 Throat Surfaces of AP0 (600 x 600 x 600 voxels)	128
Figure 6.15 Comparison of 3-D Throat Size of AP0 and MT0	129
Figure 6.16 Comparison of 3-D Throat Size of AP0 and AP14	130
Figure 6.17 Comparison of 3-D Throat Size of MT0 and MT14	131
Figure 6.18 Comparison of 3-D Pore Size Distribution of AP0 and MT0	132
Figure 6.19 Comparison of 3-D Pore Size Distribution of AP0 and AP14	133

Figure 6.20 Comparison of 3-D Pore Size Distribution of MT0 and MT14	133
Figure 6.21 Mean 3-D Pore Diameter vs. Standard Deviation of 3-D Pore Diameter ...	134
Figure 6.22 Sub-Volumes of Same Size: 230 x 1100 x 230	135
Figure 6.23 Sub-Volumes of Various Lengths ($L \times 1100 \times 230$; $L=i \times 230$, $i=1 \dots 7$).....	135
Figure 6.24 Tortuosity of 8 Sub-Volumes of AP0 with Size 230 x 1100 x 230 Voxel .	136
Figure 6.25 Mean Shortest Path Lengths for Each Sub-Volume of Various Length (230, 460, 690, 920, 1150, 1380, 1610 and 1800 Pixel)	137
Figure 6.26 Mean Tortuosity for Each Sub-Volume of Various Length (230, 460, 690, 920, 1150, 1380, 1610 and 1800 Pixel)	137
Figure 6.27 Tortuosity in x, y, and z Direction.....	139
Figure 6.28 Mean Tortuosity vs. Standard Deviation of Tortuosity.....	139
Figure 6.29 Effects of Number of Dilations Cycles on Tortuosity Measurement of AP0	141

SUMMARY

In the last decade, a significant amount of research has been performed to characterize the microstructure of unsheared and sheared triaxial sand specimens to advance the understanding of the engineering behavior of soils. However, most of the research has been limited to two-dimensional (2-D) image analysis of section planes that resulted in loss of information regarding the skeleton of the soil (pore structure) and other attributes of the three-dimensional (3-D) microstructure. In this research, the 3-D microstructures of triaxial test specimens were, for the first time, reconstructed with optical microscopy and characterized. A serial sectioning technique was developed for obtaining detailed 3-D microstructural images from 2-D sections of triaxial test specimens. The mosaic technique was used to yield high-resolution large field of view images. Various 3-D characterization parameters such as void ratio, pore size, throat size, and tortuosity, were used to study the microstructures of the specimens and the results from these studies were compared with those from 2-D analysis.

To study the preparation method induced variation in soil microstructure, two specimens prepared with air pluviation and moist tamping methods respectively were preserved with epoxy impregnation. A coupon was cut from the center of each specimen, and following a serial sectioning and image capture process, the 3-D structure was reconstructed. To study the evolution of structure during shearing tests, two additional specimens prepared to the same initial conditions with air pluviation and moist tamping methods respectively were subjected to axial compression loading under constant

confining pressure up to a global axial strain level of 14%. After shearing, the structures of these air pluviated and moist-tamped specimens were also preserved with epoxy resin impregnation and analyzed following the same procedures as the unsheared specimens. The evolution of both the particle and pore structures was investigated accordingly.

It was found that generally, moist tamped specimens were initially less uniform but had a more isotropic structure than air pluviated specimens. The standard deviations of 2-D local void ratio and 3-D pore size in dilated regions of sheared air pluviated and moist-tamped specimens were found to be smaller than those of as-consolidated specimens at a given void ratio. Tortuosity decreased with increasing pore size. It was also evident that the soil structures evolved differently depending on the initial structure. Comparison between 2-D and 3-D results indicated that it is not sufficient to use 2-D section information for characterizing some microstructural features.

CHAPTER I

INTRODUCTION

1.1 Motivation

It is well known that soil properties, such as strength, permeability, and compressibility, are directly related to soil fabric, composition, and inter-particle forces. In the last decade, a significant amount of research has been performed to characterize the microstructure of unsheared and sheared triaxial sand specimens to advance the understanding of the engineering behavior of soils. Parameters such as local void ratio and particle orientation have been extensively used in 2-D characterization of triaxial test specimens prepared by different methods such as air pluviation, moist tamping and water deposition (Kuo, 1994; Jang, 1997; Park, 1999; Chen, 2000; Yang, 2002). These studies have provided valuable insight into the microstructure of triaxial test specimens.

Walker and Trudgil (1983) have demonstrated the difficulties in understanding the physical properties of soils without the knowledge of the 3-D distributions of pores and soil aggregates. In particular, information concerning the skeleton of the specimen (pore) and other attributes for three-dimensional microstructure are lost when observations are limited to independent random two-dimensional sectioning planes. Therefore, three-dimensional characterization is of interest, not only to provide better quantification of the initial microstructure of a soil specimen but also to improve the understanding of the structure changes of soils specimens when loaded. With the recent

advances in imaging technology that has made handling of large volumetric datasets feasible, it becomes promising to apply 3-D image analysis technique to facilitate the studies of soil structure.

1.2 Research Scope

In this study, a serial sectioning technique was developed and implemented to reconstruct a detailed 3-D microstructural model from a series of 2-D section images from triaxial test sand specimens. This technique involves gradual removal of material layers to obtain a series of 2-D images that represent sections of a sand microstructure. To efficiently obtain high-resolution 2-D images with a large field of view, a mosaic technique was used. Three dimensional microstructure models are reconstructed by assembling the digitally stitched section images. A series of 2-D and 3-D analyses were performed on the reconstructed structure using various 2-D and 3-D characterization parameters, such as void ratio, pore size, throat size and tortuosity.

Four specimens prepared by air pluviation and moist tamping methods and sheared to different global axial strain levels (0% and 14%) were analyzed in terms of local void ratio distribution, 2-D and 3-D pore size distribution, 2-D and 3-D throat size distribution, and tortuosity distribution. Medial axis, which preserves the characteristics of the structure both topologically and geometrically, was used to quantify the pore space of the specimens. Through this study, the differences in results of the 2-D and 3-D analyses were investigated.

It was found that, generally moist tamped specimens were less uniform and more isotropic than air pluviated specimens. The standard deviations of local void ratio and 3-

D pore size distributions in dilated regions of strained air-pluviated and moist-tamped specimens were found to be smaller compared to those of as-consolidated specimens for a given void ratio. Tortuosity decreases with increasing pore size. It was also evident that the soil structures evolved differently depending on the initial structure based on a comprehensive comparison between the four samples and the corresponding data of previous studies. Direct comparison between 2-D and 3-D results indicated that it might not be sufficient to use 2-D section information for characterizing some microstructural features.

1.3 Organization of the Dissertation

The dissertation has been divided into 7 chapters. In Chapter 2, previous work on related subjects, with a focus on 2-D and 3-D microstructure characterization are reviewed. The procedures for applying the serial sectioning and the mosaic methods to triaxial test specimens are described in Chapter 3. The characterizations of two simulated structures (simple cubic packing and face centered packing) both two-dimensionally and three-dimensionally using a medial axis based research software program (3DMA) are presented in Chapter 4. Four specimens of real sand are quantified in Chapter 5 using 2-D image analysis to study the microstructure variations and evolution under triaxial compression. Chapter 6 presents 3-D image analysis on the reconstructed 3-D specimens. Finally, conclusions, contributions of the present study, and recommendations for future research are given in Chapter 7.

CHAPTER II

LITERATURE REVIEW

2.1 Introduction

The main goals of this research were to develop the experimental procedures to digitally reconstruct 3-D sand microstructure and to investigate the preparation-induced variation and shear-induced evolution in the microstructure of triaxial test specimens using a optical image analysis technique. The results obtained with the two-dimensional (2-D) analysis method used to date are compared with the 3-D analysis results. These goals require preparing triaxial test specimens with air pluviation and moist tamping methods, preserving the structure of the test specimens using an epoxy impregnation technique, preparing coupons cut from the specimens for image capture using serial grinding and polishing, and reconstructing the structure of the specimen using a three-dimensional image analysis technique. This chapter summarizes the relative background information about: (i) Specimen preparation; (ii) 3-D image collection; (iii) 2-D microstructural analysis of triaxial test specimens and (iv) 3-D reconstruction and characterization of microstructure.

2.2 Specimen Preparation

2.2.1 Introduction

The majority of laboratory tests on sand and gravel are performed on reconstituted specimens because obtaining samples of these materials in their undisturbed and natural state is very difficult due to the lack of natural cohesion. Several techniques have been developed to reconstitute soil specimens in an effort to create similar microstructures to natural soils since it has been qualitatively and quantitatively demonstrated using 2-D image analysis that the initial microstructure of reconstituted soil specimens affects shearing behavior of soil in triaxial tests (e.g. Jang, 1997; Park, 1999; Chen, 2000; Yang, 2002).

2.2.2 Triaxial Test Specimen Preparation

Pluviation and moist compaction methods are the two most commonly used techniques for reconstituting granular soil specimens in the laboratory (Chen, 2000). Pluviation methods are argued to effectively simulate the natural alluvial deposition. Air pluviated specimens are prepared by raining sand particles through air into a membrane-lined mold. The density of the specimen is controlled mainly by the kinetic energy of the sand particles, which in turn is a function of the deposition velocity (fall height) of particles and pluviation intensity (flow rate). Typically, large fall heights which result in high deposition velocities and hence high kinetic energies produce dense specimens, while high pluviation intensities produce loose specimens. The disadvantage of pluviation methods is that particle segregation will be present if the soil is well graded or contains fines (Chen, 2000).

A laboratory pluviation system capable of automatically controlling fall height and flow rate was developed by Jang (1997). Sand was poured into the pluviation container in which the opening block, dispersion screen and control plate are located. To maintain a constant fall height during specimen preparation, the pluviation container is raised continuously at the same rate as the rise in the surface of the sand being deposited in the specimen mold. By using an automatic motor-driven system, operator dependence is minimized. In this study, this system was used to air pluviated specimens.

Moist tamping is the preferred method for simulating in-situ microstructures densified by vertical tamping or vibration (Ladd, 1978). It is relatively easy to perform in the laboratory and particle segregation can be minimized (Chen, 2000). One of the disadvantages of the moist tamping method is that the density of a compacted specimen is not as uniform as that of specimens prepared by pluviation methods (Frost and Park, 2003).

Moist tamped specimens are constructed by compacting layers of moist soil into a membrane lined split mold with a circular tamper. The density of the specimen is predetermined and can be controlled by adjusting the dry weight and volume of sand placed in each layer. Undercompaction was developed to overcome the observed nonuniformity in the compaction method, (Mulilis et al., 1977; Ladd, 1978). In this technique, the lower layers are initially compacted to a looser than the final desired density by predetermined amounts so that the final density of each layer is equal to the target density. The difference in density between successive layers is defined as the undercompaction ratio (Ladd, 1978). The structure of specimens prepared by moist tamping may represent that of sand fills densified in layers (Mitchell et al., 1976).

However, the density distribution over the height of specimen has been qualitatively shown to be erratic and nonuniform (Mitchell et al., 1976; Frost and Park, 2003).

Park (1999) used a double membrane configuration in preparing dense moist tamped specimens. This configuration was believed to be able to seal any leaks in the inner membrane created by the friction between the sand particles, the membrane, and the tamping disc while the layers were being compacted. Also, it was found that a moisture content of 5% was adequate for moist tamping the ASTM graded sand (Park, 1999).

2.2.3 Specimen Preservation

It is well accepted that the behavior of granular soil is not only controlled by the density and confining stress, but also depends on the arrangement of particle and pore space, i.e. soil fabric. Therefore, it is important to be able to preserve the actual state of granular soil, either prior to testing or after testing, to enable study of the microstructure. Preservation of particulate materials specimens can be accomplished either by freezing or by impregnating a curing agent into the specimen, which can incorporate artificial cohesion into the soils by changing the nature of the pore fluid or by replacing the pore fluid with another material (Jang, 1997).

The freezing technique involves lowering the temperature of the soil mass by circulating a coolant inside a pipe embedded into the soil mass and turning the pore water into ice, with the integrity of the soil structure being preserved accordingly (Chen, 2000). Freezing techniques have been adopted, especially in the field, to obtain undisturbed granular samples. However, this technique could not be utilized in the present research because the frozen sample would not remain in a frozen state during the coupon surface preparation process associated with sectioning, grinding, and polishing (Jang, 1997).

Chemical preservation involves using chemical liquid to give cohesion to granular materials and impart rigidity into the soil mass. Although chemical impregnation is arguably more complicated than the freezing method, it is relatively inexpensive and thin sectioning is possible (Chen, 2000). The criteria for choosing suitable chemical agents are: low viscosity to reduce the potential disturbance on the structure and to maximize the replacement of pore fluid; non-reactive with either the soil or the pore fluid; durability, noncorrosive and nontoxicity; rapid hardening after a suitable period which allows impregnation of a desired volume of soil; limited volume change during hardening; sufficient stiffness after hardening. Jang (1997), Park (1999), Chen (2000) and Yang (2002) have performed extensive experimental work on sand specimen preservation. They successfully preserved sand specimens with an epoxy resin and quantified the microstructure of sand specimens by using two-dimensional image analysis techniques. During their research, they used the epoxy resin to preserve reconstituted triaxial specimens both before shearing and after shearing. Even though, the preservation is irreversible and has some volume limitations, it causes minimum disturbance during impregnation and can impart sufficient stiffness for thin sectioning.

2.3 Three-Dimensional Image Collection

2.3.1 Introduction

The use of 2-D image analysis to represent both the grains and the pores in soils has been practiced for more than twenty years (Ismail, 1975; Ringrose-Voase and Bullock, 1984; Moran and McBrantney, 1992; Kuo and Frost, 1995; Jang, 1997; Park, 1999; Chen, 2000; Yang, 2002). However, Walker and Trudgil (1983) have demonstrated

the difficulties in understanding the physical properties of soils without the knowledge of the 3-D distributions of pores and soil aggregates. Recently, volumetric digital images have started to play an important role in many applications, especially in medical image processing, microstructure study of various materials, and seismic data processing among other fields. This is due to advances in imaging technology that has made handling of large datasets feasible.

Computer-aided 3-D reconstruction in geomaterials study is still a relatively new field, even though the necessary analytical and data-processing equipment are available and the application of computerized 3-D micro- and macrostructure reconstruction is becoming wide-spread in many other disciplines (Wong et al., 1983; Tewari, 1999; Sutton et al., 2001; Brey et al., 2002; Cooper et al., 2003; Lund and Voorhees, 2003; Maire et al., 2003; Chawla et al., 2004; Singh and Gokhale, 2005). Recent applications of computer-based 3-D reconstruction of geomaterials demonstrate the advantages and versatility of this technique. These applications involve using mathematical morphology and X-ray computed tomography to measure pore size distribution in sandy loam soil cores (Herman et al., 2002), quantification of macropore networks in undisturbed soil cores by reconstructing 3-D structure from 2-D matrices generated by an X-ray CAT scanner (Perret et al., 1999), and characterization of reservoir rocks in terms of chamber-and-throat networks (Tsakiroglou and Payatakes, 2000),

A three-dimensional digital image consists of a stack of two-dimensional slices or images. Generally, there are two ways to collect these 2-D images: non-destructive and destructive methods.

2.3.2 Non-destructive Method

Magnetic resonance imaging (MRI) is one of the more common methods in 3-D imaging. An MRI scanner contains magnetic coils that produce magnetic fields (Lichtenbelt et al., 1998). With spatial and amplitude control over the gradients of signals, arbitrary planes of data can be isolated. The main application of this method is in medical biophysics.

Another class of non-destructive techniques is based on ultrasonics or its variants, such as acoustic microscopy or laser ultrasonics. The laser-based ultrasonics rely on good reflection properties of the specimen. The development of confocal microscopes with computer control has brought about the recent use of optical sectioning for 3-D image reconstruction of tissues and materials (Menendez et al., 2001)

X-Ray Computed Tomography was initially developed for clinical use in radiology in the 1970's. In the 1980's the availability of synchrotron X-Ray sources made high spatial resolution X-ray transmission measurements possible. It is a nondestructive technique for visualizing features in the interior of opaque solid objects and for obtaining digital information on their 3-D geometries and properties. X-Ray CT provides non-destructive volumetric data of elemental composition, by creating images that map the variation of X-ray attenuation within objects, that in turn relates closely to density variations. Because density transitions usually correspond to boundaries between materials or phases, these data are often straightforward and intuitive to interpret (Ketcham and Carlson, 2001). The technique is useful for a wide range of materials, including rock, bone, ceramic, metal and soft tissue.

High-resolution X-ray CT differs from conventional medical CAT-scanning in its ability to resolve details as small as a few microns in size, even when imaging objects

made of high density materials. Currently, a third-generation X-ray CT instrument is capable of producing tomographic volumes of 1-2 micron resolution over a 2-3 mm field of view (Dowd et al., 1999).

However, the resolution of the 3-D image obtained from X-ray CT is limited by sample size (i.e., a larger sample volume results in larger voxel size). It is important to consider the trade-off between the optimum sample volume and the desired resolution for a particular study. Furthermore, artifacts such as beam hardening, ring artifacts and a variety of other artifacts cannot be completely resolved, which sometimes obscures details of interest (Denison et al., 1997). This can cause problems during subsequent data rendering and quantitative analysis.

2.3.3 Destructive Method

Serial sectioning is a well-established destructive technique for obtaining 3-D microstructural data. The first 3-D reconstructions with the serial-sectioning method and a wax plate technique were made in 1883 (Kriete, 1992). In its simplest form, the technique involves the careful removal of a layer of material, followed by imaging of the freshly created surface. This is repeated many times in order to build up a series of 2-D images which are then reconstructed (i.e., stacked) to form a 3-D volume. A flow chart of a typical serial sectioning process is shown in Figure 2.1. This serial sectioning method has had wide application in a variety of fields, such as metals (Bystrzycki and Prezetakiewicz, 1992; Ammann et al., 1996), geological materials (Bryon et al., 1995; Vogel, 1997; Marschallinger, 1998), and biomedical study (Odgaard et al., 1990; Bystrzycki and Prezetakiewicz, 1992; Streicher et al., 1997).

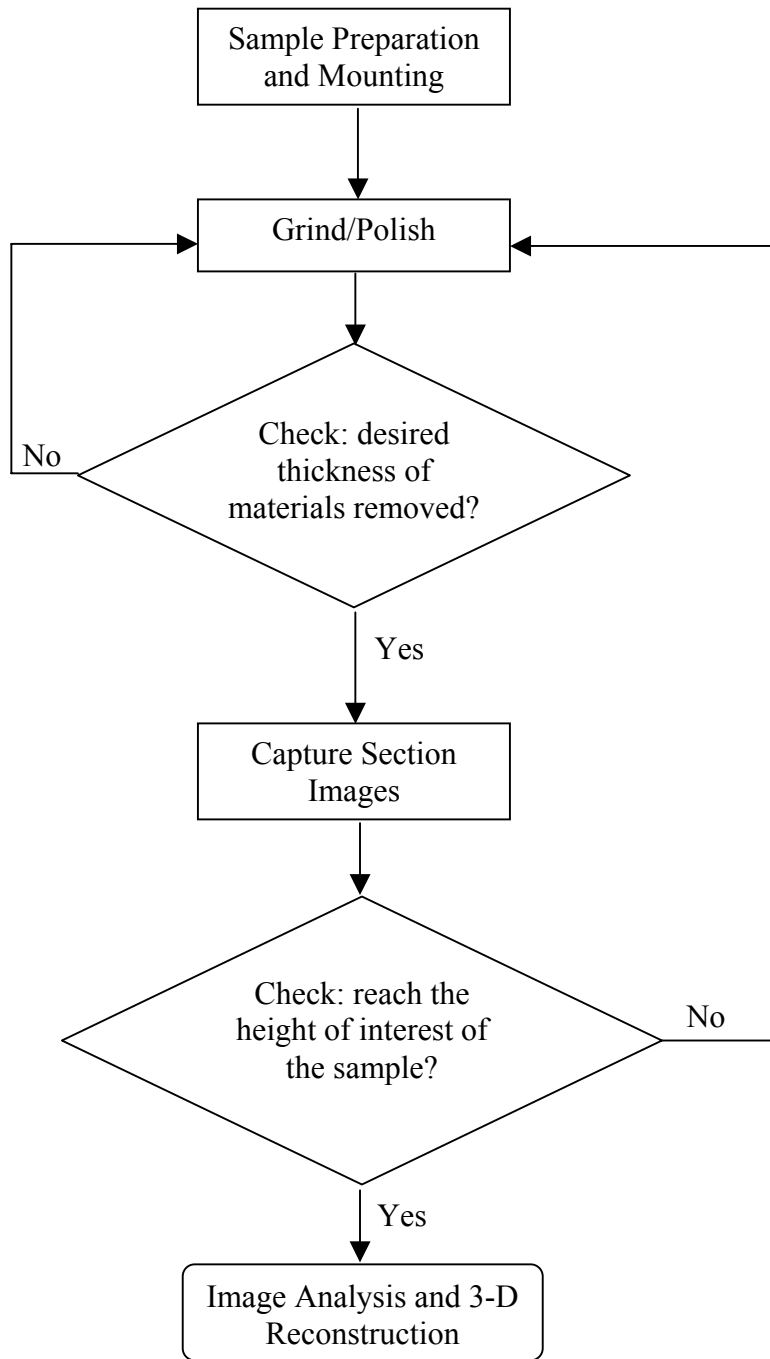


Figure 2.1 Flow Chart of Typical Serial Sectioning Process

Yanuka et al (1984) proposed a procedure for serial sectioning of impregnated porous media. Between forty-six to eighty cross-sections were prepared by parallel

polishing off of between 10 and 50 micron per cycle. With the limitations of computing and imaging technology at that time, no true three-dimensional image was presented.

However from the study of the pore sizes by obtaining the lengths in orthogonal x, y and z directions at each point sampled, they concluded that the serial sectioning and imaging method provided a powerful tool for investigating three-dimensional geometrical and topological properties of pore space.

Marschallinger (1998) introduced a method for 3-D reconstruction of macroscopic features in geological materials. The features of interest in the material were macroscopically distinguishable by their color. Samples were subject to cycles of precision serial lapping and subsequent data acquisition by a flatbed color scanner. Spectral characteristics of features subject to 3-D reconstruction were defined by training sets that controlled batch-supervised image classification by the maximum-likelihood algorithm. They used two exactly matching, fixed reference systems to precisely relocate the sample during data acquisition. The method provided considerable detail of the reconstructed structure of samples.

Mangan et al (1997) applied the three-dimensional reconstruction of serial sections to examine Widmanstatten plates in a high-manganese steel. They used microhardness indentation to calculate the thickness of each section. For the sample microstructure investigated by them, the existence of three nonparallel plates allowed consecutive serial sections to be manually aligned by obtaining a best fit between the sections.

Li et al (1998) developed a serial sectioning method for constructing 3-D microstructures of Si-reinforced Al-Si-Mg alloys. Specimens were cut into blocks of

about 5mm x 5mm x 2mm by using a Buehler Isomet low-speed saw. The specimen was then mounted using a Metaserv automatic press. A Buehler Ecomet IV polisher and grinder was used to polish the specimen. Approximately 15-20 sections were stacked to create three-dimensional specimens.

In the past, layer removal was typically accomplished by hand, using standard metallographic polishing techniques, which is extremely time-consuming. In addition, the minimum slice thickness that could be repeatedly obtained in practice was 5–10 μm (Spowart et al., 2003). However, it is now possible to remove one micron per cycle with some delicate precision surface preparation machines. Tewari and Gokhale (2000) used 90 serial sections, one micron apart to study a volume segment of the liquid-phase sintered microstructure of a tungsten heavy alloy. They concluded that the reconstructed volume could be used to study the connectivity of phases in three-dimensions.

The advantages of the serial sectioning method are accuracy, no artifacts such as those resulting from X-ray CT, and cost-effectiveness. It is highly accurate for particle sizes in the 1–3 μm range (Li et al., 1998). Two examples of 3-D reconstructed structure are shown in Figure 2.2 and Figure 2.3 respectively.

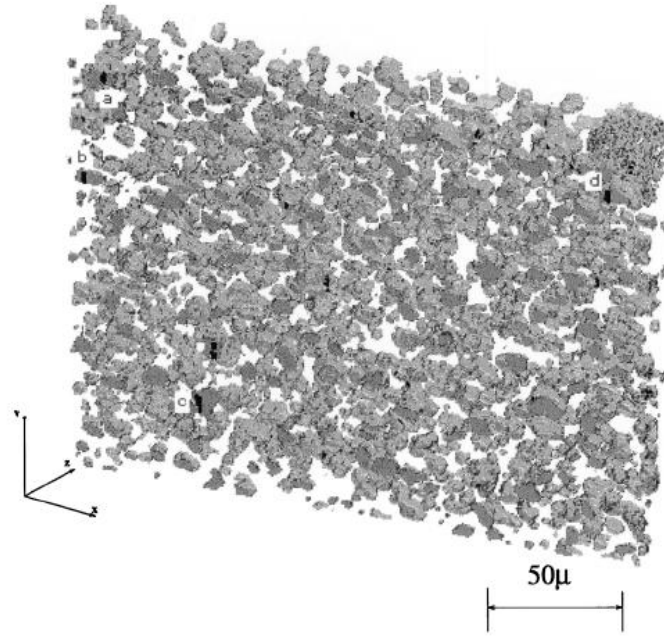


Figure 2.2 3-D Reconstructed Volume of Naturally Aged Composites with 10% Weight Fraction Si and Larger Particle Size (Li et al, 1998)

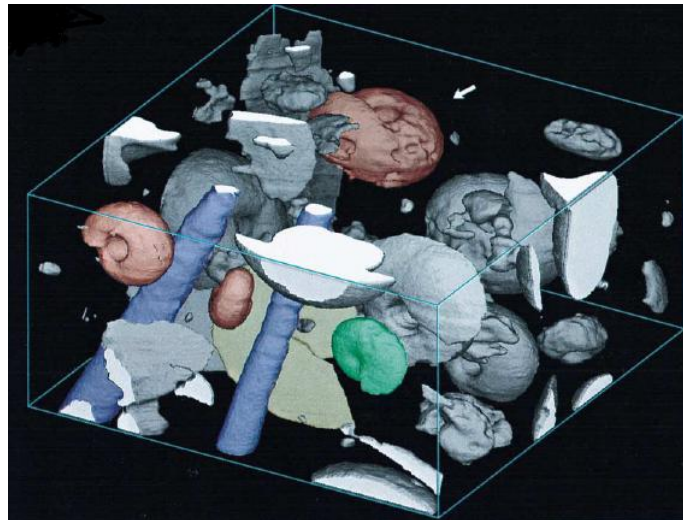


Figure 2.3 Surface rendering of limestone sample, after binary 3-D grow/shrink filtering and 3-D average filtering. Dimensions 341x431x180 voxels=2.90x3.66x1.53 cm, 8 bits per voxel, approximately 26.5 Mbyte (Marschallinger, 1998)

2.4 Microstructural Analysis of Triaxial Test Specimens

2.4.1 Introduction

Image analysis has been a useful tool during the last two decades for microstructural analysis because of the rapid development of the computer software and hardware.

Image processing includes five primary steps: acquisition of images, image storage, image enhancement, image binarization, and feature measurement (Russ, 1995). In 3-D imaging, an additional step called image reconstruction is needed to visualize the 3-D volume. Most of the processing tools for 2-D images can be applied directly in 3-D image analysis (Russ, 1995).

A large amount of 2-D microstructure analysis of triaxial test specimens have been performed in the past decade at the Georgia Institute of Technology. Local void ratio distribution and particle orientation amongst other parameters have been quantified to characterize the microstructure of triaxial test specimens (Kuo, 1994; Jang, 1997; Park, 1999; Chen, 2000; Yang, 2002). Both inherent and induced microstructures have been studied.

Three-dimensional characterization of microstructure has been used to study consolidated porous media for some time (Yanuka et al., 1986; Lymberopoulos and Payatakes, 1991; Zhao et al., 1994; Baldwin et al., 1996; Coles et al., 1998; Delerue et al., 1999; Lindquist, 2001; Oren and Bakke, 2003; Lin and Miller, 2004). Quantifying the pore structure of a triaxial test specimen is considered to be a promising way to study the microstructure of both as prepared and post-shearing sand specimens.

2.4.2 2-D Image Analysis on Triaxial Test Specimens

Frost and Kuo (1996) developed methodologies to automatically quantify aspects of the fabric/structure of cohesionless materials based on mathematical morphology. The automated algorithms eliminated the problems associated with the significant amount of manual work and subjective decisions required by others in making the measurements. Parameters such as local void ratio and particle orientation have been extensively used in characterization of triaxial test specimens prepared by different methods such as air pluviation, moist tamping and water deposition.

The research work that have been performed by Jang (1997), Park (1999), Chen (2000) and Yang (2002) are summarized as follows:

- Local void ratio distribution was shown to be a reliable measure of soil structure. Statistical parameters, the mean and the standard deviation of local void ratio distribution, were found to be a function of the specimen preparation methods and specimen density. The characteristics of these two parameters with respect to air pluviation, moist tamping and water deposition of ASTM graded sand were identified.
- The degree of disorder in the frequency histograms of local void ratio was quantified in terms of local void ratio entropy. It was found that water deposition yields more uniform specimens than both the moist tamping and air pluviation methods. Local void ratio entropy was shown to be an effective parameter for describing the degree of dispersion in the local void ratio distribution

- The effect of specimen preparation method on the orientation of sand particles was studied based on orientation entropy and anisotropy. It was shown that particles in moist tamped specimens were more isotropically oriented than those in air pluviated and water deposited specimens. It was also found that, air pluviation and water deposition produced specimens with sand particles more horizontally oriented.
- The evolution of sand structure along a stress path was studied using a series of specimens preserved at different states of triaxial shearing. It was found that water-deposited specimens exhibited a similar global shearing response to air-pluviated specimens, which is consistent with the similarity in initial microstructure. Water-deposited and air-pluviated specimens displayed a barrel shape at a global axial strain level of 14%. However, moist-tamped specimens developed a distinct shear band and most dilated regions appeared to be located in the lower half of the specimens. This can be attributed to the difference in initial soil structure, particularly the uniformity with respect to density and particle orientation distribution.
- According to the local void ratio distributions, as the shearing progressed, the standard deviation of void ratios in the failing (central) region increased at a smaller rate compared to the general trend for specimens. In other words, while sand particles dilated and approached critical state, void ratios became more uniform.
- Based on the study of evolution of spatial void ratio distribution, the dilation in air-pluviated and water-deposited specimens expands uniformly toward both ends of the specimens. Moist-tamped specimens developed less uniform dilation regions due to the genesis of a shear band.

- Induced entropy is lower than inherent entropy. In addition, induced standard deviations of local void ratios were smaller than inherent standard deviations. This means the uniformity in terms of void ratio within the dilated regions is higher.
- More concentrated deformation towards the middle of the $H/D=2$ specimen is due to end platens effect, which also resulted in the largest spatial and local variations of void ratio. Less lateral deformation is observed in the $H/D=1$ specimens with non-lubricated ends compared to the $H/D=2$ specimens with the same end conditions.
- Particle orientation studies showed that obvious particle rearrangement during shearing occurred in loose specimens with an initial isotropic microstructure. Due to the looser particle packing in the loose specimens, the end platens had less influence on the specimens in terms of deformed shape and particle orientation compared to dense specimens.

2.4.3 Available 3-D Analysis Methods

The two-dimensional image analysis based studies discussed above have provided valuable insight into the microstructure of triaxial test specimens. However no studies on the pore structure of triaxial test specimen have been performed to date. For example, information regarding the pore structure of soils, which is important in simulating fluid flow through the soil is not available. There are quantitative tools, such as the stereology method, that can be used to measure some geometric parameters (e.g., porosity and specific surface area) from 2-D images and used to estimate equivalent 3-D parameters (Underwood, 1970). A list of some of the more frequently used parameters for pore structure is shown in Table 2.1. However, it is limited to study of spherical or irregular, but always convex pores (Lymeropoulos and Payatakes, 1991). Dullien (1992) also

summarized the following shortcomings of stereology based methods to determine important pore structure parameters such as pore size distribution:

- No information on pore throat sizes;
- Two or more adjacent pores may be counted as one pore;
- All pores are assumed to be geometrically similar;
- The pore shape function derived from 2-D photomicrographs is assumed to represent the shape function of 3-D pores;
- A great deal of the detailed geometry of the pore space remains unknown.

Some geometric and morphological information describing a three-dimensional structure cannot be inferred from observations on two-dimensional sectioning planes (Fredrich, 1999; Moreau et al., 1999; Tewari and Gokhale, 2000). Li et al (1998) found that microstructural parameters, such as particle size, shape, orientation and spatial distribution, obtained from observations on polished two-dimensional surfaces, are likely to be inconsistent with observations from the real three-dimensional microstructure. In particular, information concerning the skeleton of the sand specimen (pore) and other attributes for three-dimensional microstructure are lost when observations are limited to independent random two-dimensional sectioning planes. Therefore, three-dimensional characterization is of interest, not only to provide better quantification of the initial microstructure of a soil specimen but also to improve the understanding of the structure changes of soils specimens when loaded.

Table 2.1 Porous Structures Parameters

Parameter Name	Definition	Comments
Porosity (ϕ)	The fraction of the bulk volume of the porous sample that is occupied by pore or void space.	2 kinds of pore: interconnected; isolated (cannot contribute to transport of matter across the porous medium)
Specific Surface Area	The interstitial surface area of the voids and pores either per unit mass (S) or per unit bulk volume (S_v) of the porous material	A measure of the adsorption capacity of various industrial adsorbents; Related to the permeability
Connectivity	The number of nonredundant closed-loop paths by which all regions inside the shape can be inspected	A topological parameter that measures the degree to which a structure is multiply connected. In a homogeneous, macroscopic, porous medium the numerical value of the connectivity is proportional to the size of the sample.
Coordination Number	The average number of branches (or bonds) meeting at a node.	
Genus (G)	The largest number of cuts that may be made through parts of the shape without totally disconnecting any part from the rest	
Throat Size	Throat: the minimal cross-sectional area of each channel in the void space	Effective Pore Throat Radius: Assuming circular throats, each throat area is converted to an effective radius.
Pore Size (Operational Definition)	The pore space is divided into a series of pore bodies separated by throat surfaces.	Effective Pore Radius: Assuming spherical bodies, each pore body volume is converted to an effective radius.
Shortest Path and Tortuosity	Geometrical Tortuosity: Ratio between the actual path length and the linear separation of two parallel planes.	

(Dullien, 1992; Lindquist, 1999)

Some 3-D investigations incorporating geometry (Lin and Cohen, 1982; Yanuka et al., 1984) were based on extensive sampling of the pore space data. The resulting

interconnected model pore space was then studied. However, since the actual pore space was not formally identified, the model could not be evaluated by comparison with real examples.

Baldwin et al (1996) used morphological thinning to partition the void space in 3-D volumetric images obtained from MRI. The thinning process also identified the regions which formed the pores and pore necks. Distribution of pore size, coordination number and pore surface area between interfaces with solid phase and those with neighboring pores was obtained from the partitioned data. The results from the algorithm agreed quantitatively with their earlier analyses of the pore space of packed beads.

Perret et al (1999) developed a set of programs to study macropore networks in soil. The macropores are identified by using two clustering algorithms. After a filtering program is applied to remove those networks having a length $\leq 10\text{mm}$, a large 3-D matrix that contains matrix elements of 0 (i.e., soil matrix domain) and 1, 2, 3, ..., n for the macropore domain can be obtained. The polygons formed by these macropores are identified to reconstruct the exact 3-D network. Pore size, number, tortuosity, connectivity and hydraulic radius can be measured from the model.

Vogel and Roth (2001) used connectivity function (Vogel, 1997), which is defined by the 3-D-Euler number of the pore space which is dependent on the pore radius, to measure pore topology directly. In the network model, the concepts of pore bodies and pore throats are omitted. It is believed that the model is more suitable for natural soil that contain large pores, which are continuous over a considerable length (i.e. root channels or burrows of animals).

Herman et al (2002) studied the pore size distribution and connectivity of three heterogeneous sand loam soil cores using X-ray CT with a resolution of approximately 50 micron. Mathematical morphology (erosion and dilation with spheres of growing diameters) was performed on the binary volumes. It was shown from the pore size distribution that the amount of bigger pores (in the range of 1-2 mm) decreases as the soil gets wetter.

Lindquist et al (1996) introduced medial axis to study pore structure from X-ray CT scanning. The medial axis traces the fundamental geometry of the void pathways. The medial axis is constructed during an iterative erosion procedure which, at each step, replaces the image of the void structure with a smaller version obtained by eroding its surface layer of voxels. The algorithm was applied to high (5 μm) resolution microtomographic images of two rock chips (Berea sandstone and Danish chalk) and a sample of uniform (100 μm) diameter, packed glass beads. They statistically investigated several geometrical properties of the structure of the resulting medial axes. It was found that the distributions for the two real rock samples were exponential and for the packed glass beads was normal. A geometric tortuosity was measured by shortest paths through the medial axis. The tortuosity distribution appears well described by a gamma distribution.

Lindquist et al (1999) also developed a software package, 3DMA, to analyze the geometry of a randomly shaped object in two- and three- dimensional images. The input to the package is a 2 or 3-D digitized, gray-scale, image of the object. Specifically it is assumed that the image consists of two populations of voxels comprising an object and its background. The package has many functions such as segmentation of the images, medial

axis construction, trimming of medial axis, throat construction, and pore network construction. 3DMA allows statistical analyses including porosity, connectivity of the void paths, the distribution of lengths and tortuosities of the shortest connected pathways through the skeleton between planar sides of the image, as well as position, shape and area of grain-grain contact surfaces.

CHAPTER III

EXPERIMENTAL DEVELOPMENTS AND TECHNIQUES

3.1 Introduction

As discussed in Chapter 2, soil fabric is one of the important factors affecting soil behavior during shearing. The initial structure of the specimen is determined by the preparation method. The subsequent structure evolution during shearing is also affected by this initial structure. To study the preparation induced variation and shearing induced evolution of the structure of triaxial test specimens, two sets of specimens were prepared using air pluviation and moist tamping, respectively, to similar initial global void ratios. One of the air pluviated and one of the moist tamped specimens were preserved at this stage (0% global axial strain) using resin impregnation. The other air pluviated and moist tamped specimens were sheared to 14% global axial strain under axial compression loading. These specimens were then also preserved using epoxy impregnation. Serial slicing was performed on all four specimens to get a series of 2-D images that could be used to reconstruct the 3-D structure.

3.2 Materials

The material tested in the research is ASTM graded sand, composed of poorly graded, sub-rounded quartz sand. The grain size distribution that was determined with US standard sieve analysis according to ASTM D422-63 is shown in Figure 3.1. The median

grain size D_{50} is 0.35mm. The coefficient of uniformity C_u ($=D_{60}/D_{10}$) is 1.65. The coefficient of curvature C_c ($=D_{30}^2/(D_{10}*D_{60})$) is 1.06. The minimum and maximum void ratios were determined to be $e_{min}=0.50$ and $e_{max}=0.82$ according to ASTM D4253-93 and D4254-91 respectively. This information is listed in Table 3.1.

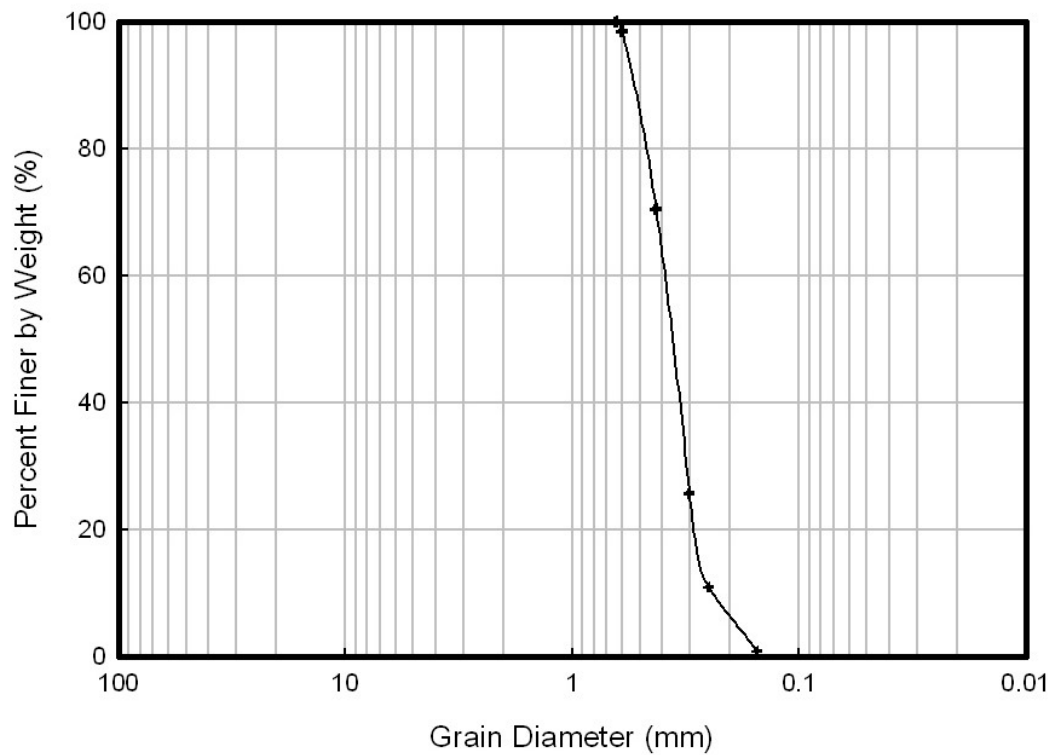


Figure 3.1 Grain Size Distribution of ASTM Graded Sand

Table 3.1 Index Properties of ASTM Graded Sand

Material Property	D_{50}^1 (mm)	C_u^2	C_c^3	G_s^4	e_{max}^5	e_{min}^6
ASTM Graded Sand	0.35	1.65	1.06	2.67	0.82	0.50

Note:

1. Median Grain Size;
2. Coefficient of uniformity;
3. Coefficient of curvature;
4. Specific gravity;
5. Maximum void ratio;
6. Minimum void ratio

3.3. Triaxial Test Specimen Preparation and Preservation

Due to the difficulty of obtaining samples of undisturbed particulate soils, most laboratory tests are performed on reconstituted specimens. There are a wide variety of methods that can be used to prepare these particulate specimens. These methods can be categorized based on the moisture condition of the soil (dry, moist, or wet), the method of soil placement (pluviation, spooning, or tubing), and the medium through which the soil is placed (air or water) (Frost, 1989). In this research, specimens prepared using air pluviation and moist tamping were investigated to study preparation induced variation and shearing induced evolution of the 3-D structure of these specimens.

3.3.1 Air Pluviation

The air pluviation system used is shown in Figure 3.2. The speed with which the sand pluviator is raised and the mass flow rate of sand into the specimen mold control the resulting density of the specimen. Sand is poured into the pluviation container in which

the opening block, dispersion screen and control plate are located. The opening block used in this study had 3 openings each with an 0.5” diameter. A screen (8 x 8 mesh) was used to disperse and uniformly distribute the sand. To maintain a constant fall height during air pluviation, the pluviation container was raised continuously at the same rate at which the surface of the sand in the mold rose. This had been previously calibrated to a rate of 130.4 g/sec. The initial total mass of sand in the pluviator was almost 960g.

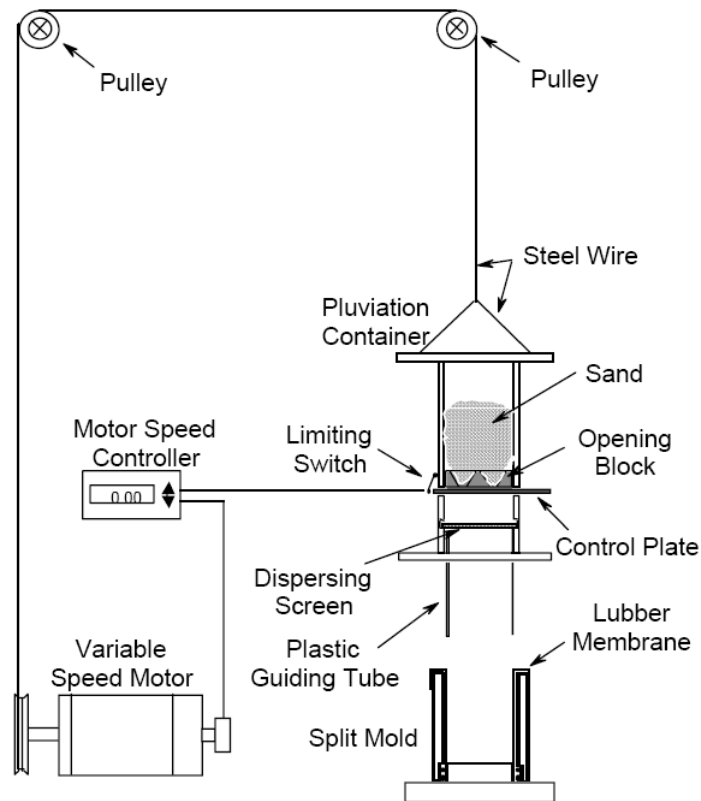


Figure 3.2 Air Pluviation System (After Jang, 1997)

3.3.2 Moist Tamping

In this research, the undercompaction technique (undercompaction ratio=3%) was used to prepare moist tamped specimens with the modified device shown in Figure 3.3. Predetermined amounts of soils were compacted into seven layers of equal thickness. To obtain the same height for each layer, seven spacer blocks with a thickness of 20mm (0.8in) each, and a platform with an acrylic cylinder were used. A reference collar was attached to the tamping rod so that the tamping disc would reach exactly the same location during the compaction of each layer. The initial moisture content of the soil of 5% was found adequate for ASTM graded sand (Park, 1999) and was used in this study. The target relative density of 75% was located in the middle layer of the specimen. The initial density target of each layer is shown in Table 3.2.

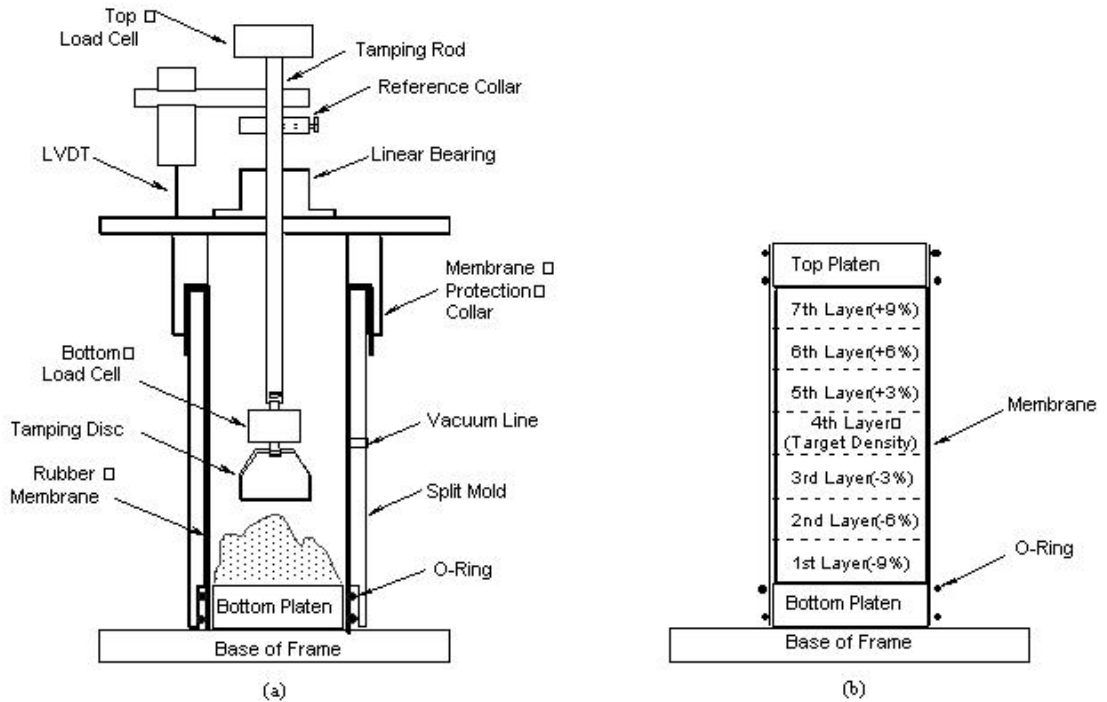


Figure 3.3 Moist Tamping System (After Park, 1999)

Table 3.2 Moist Tamping Specimen Layer Density Information

Layer	D _R (%)	e	Dry Sand Weight (g)	Water Weight (g)	Total Weight per Layer (g)
1	66	0.609	134.18	6.71	140.89
2	69	0.599	134.98	6.75	141.73
3	72	0.590	135.80	6.79	142.59
4	75	0.580	136.62	6.83	143.45
5	78	0.570	137.46	6.87	144.33
6	81	0.561	138.30	6.92	145.22
7	84	0.551	139.16	6.96	146.12

After compaction, the specimen was dried for subsequent epoxy impregnation by using the drying system shown in Figure 3.4. Dry air was drawn through the specimen by applying a low vacuum (15kPa) downstream of the specimen. It usually took 24 hours to completely dry a moist tamped specimen that had an initial moisture content of 5%.

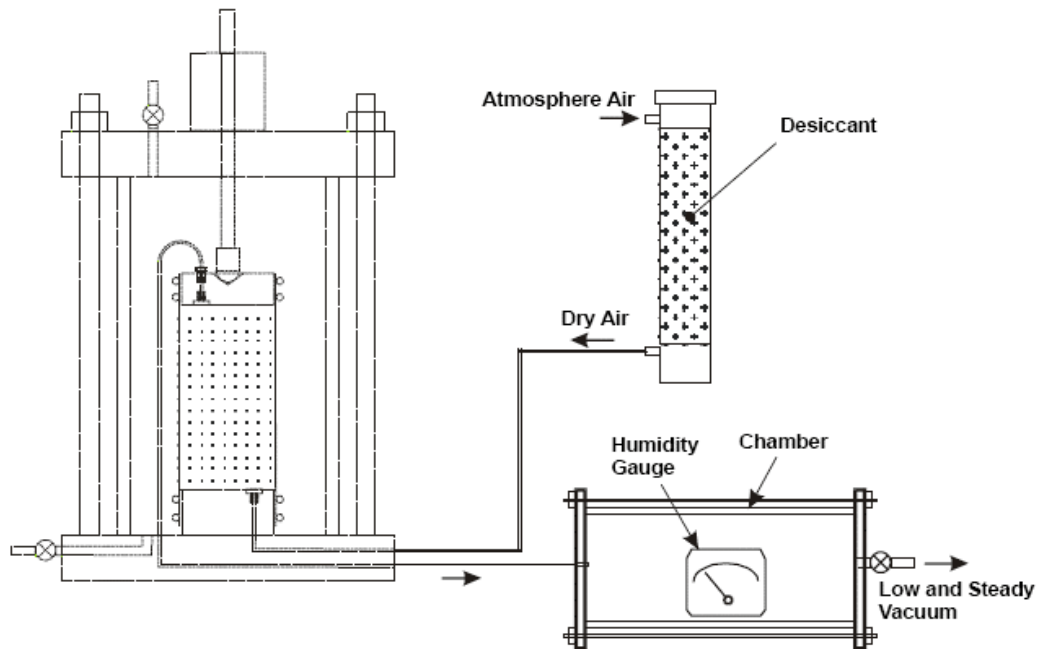


Figure 3.4 Specimen Drying System for Epoxy Impregnation (After Jang, 1997)

3.3.3 Triaxial Test and Sample Preservation

The triaxial test device used in this research is a CKC automated triaxial system manufactured by Soil Engineering Equipment Company. The device consists of a loading system together with a triaxial cell and a loading piston, a signal conditioning unit, a process interface and a computer. The output signals from the transducers are received by the interface unit that establishes the communication link between the loading system and the computer. The computer regulates the testing process by issuing control signals input by the operator, and also receives, stores and displays the data in real time during the test. In the triaxial tests, an initial confining pressure of 50kPa was applied. The stress-strain response from axial compression triaxial tests on air pluviated and moist tamped specimens are shown in Figures 3.5 and 3.6, respectively.

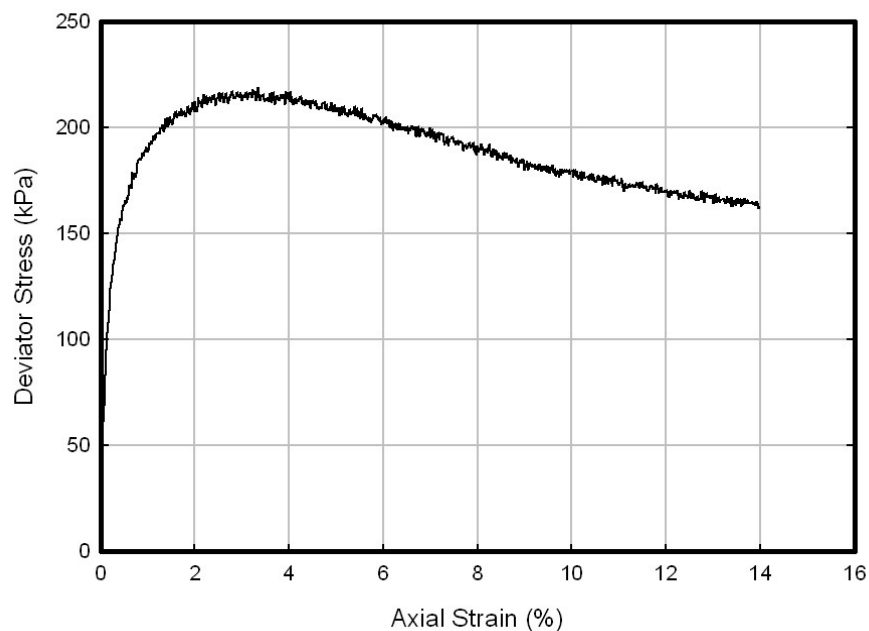


Figure 3.5 Stress Strain Relationship of Air Pluviated Specimen

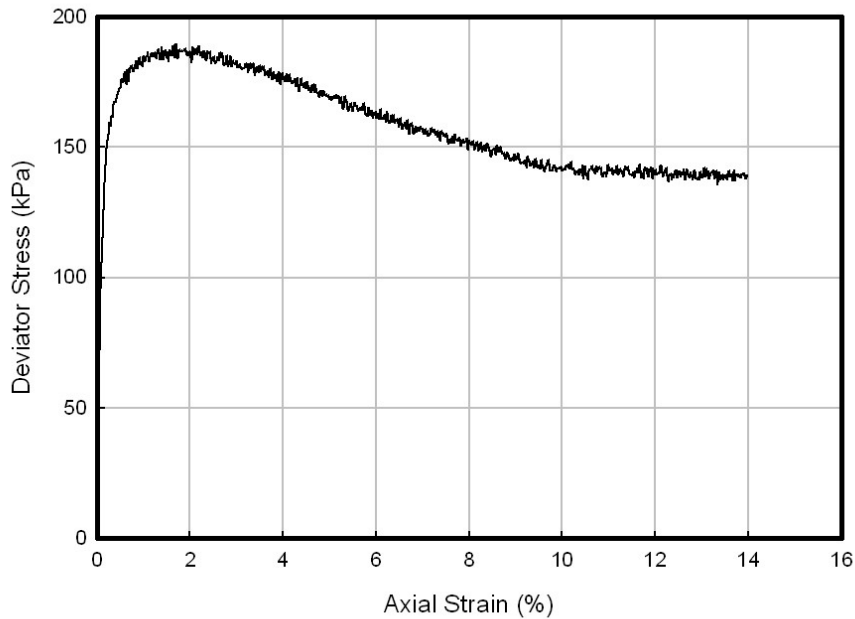


Figure 3.6 Stress Strain Relationship of Moist Tamped Specimen

Sample preservation was accomplished by epoxy impregnation, which has been proven to be able to provide the soil with sufficient stiffness to undergo the processes of sectioning and surface preparation (Jang, 1997). EPO-TEK 301, a two-part epoxy resin, manufactured by Epoxy Technology Inc., was identified as the most suitable impregnation material because of its low viscosity (100cps at 25°C), low shrinkage (about 2% of linear shrinkage) and excellent bonding strength and hardness (Shore D Hardness=81). Since epoxy resin does not cure well in moist environment, it is important to dry any moist tamped specimens before impregnation. The sample preservation system used in this study is shown in Figure 3.7. Information of the four specimens tested is listed in Table 3.3.

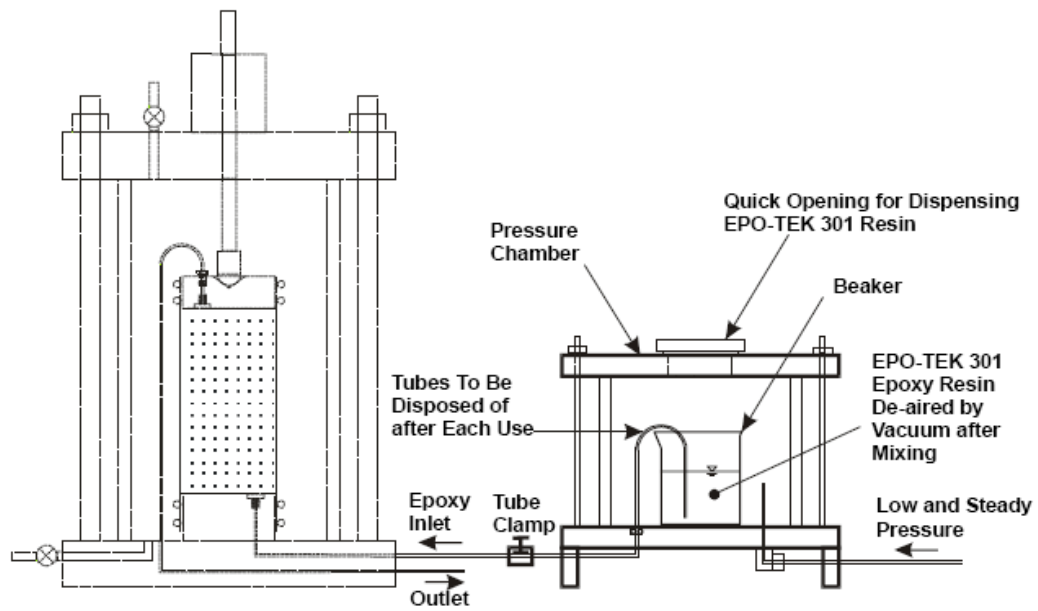


Figure 3.7 Epoxy Impregnation System for Specimen Preservation (After Jang, 1997)

Table 3.3 Four Specimens

Sample ID	Preparation Method	Confining Pressure (kPa)	Axial Strain Level (%)	L/D Ratio	Sand Type	Initial Void Ratio e_0
AP0	Air Pluviation	50	0	2:1	ASTM Graded Sand	0.582
AP14	Moist Tamping	50	14	2:1	ASTM Graded Sand	0.579
MT0	Air Pluviation	50	0	2:1	ASTM Graded Sand	0.580
MT14	Moist Tamping	50	14	2:1	ASTM Graded Sand	0.583

3.4 Serial Grinding

To reconstruct a three-dimensional structure, a set of two-dimensional images are required. In this research, a small coupon of sample was cut from each impregnated triaxial test specimen. Then a serial grinding method was applied to yield the required 2-D surface from which images were captured. For each surface, a mosaic technique was used to get an image with high resolution and large area at the same time. The three-dimensional structure of the sample was reconstructed from these high-resolution 2-D images.

3.4.1 Sample Position and Size

During this first application of 3-D reconstruction techniques to study the structure of triaxial test specimens, a portion of each specimen was extracted for analysis instead of analyzing the whole specimen. Even a small volume can require in excess of 10 hours of processing time for certain calculations. For specimens AP0, AP14 and MT0, a coupon of size 19mm x 11mm x 5mm was cut from the center, as shown in Figure 3.8. For specimen MT14, a coupon of the same size was taken from the shear band zone as shown in Figure 3.9. An estimation of the position of the shear band is shown in Figure 3.10. This will be further examined after the three-dimensional structure of the sample is constructed.

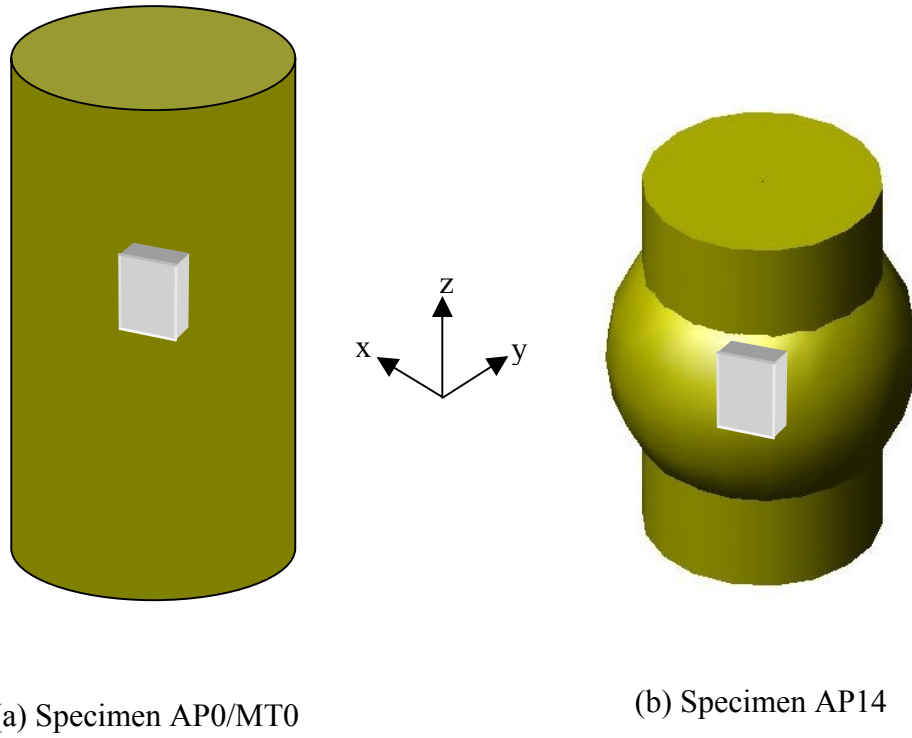


Figure 3.8 Schematic Sketch of the Coupon Position in Specimen AP0/MT0 and AP14

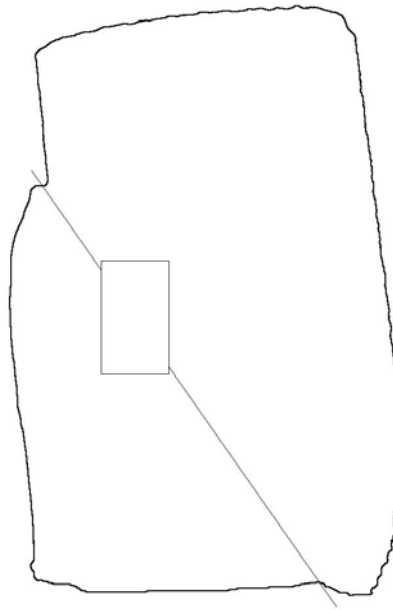
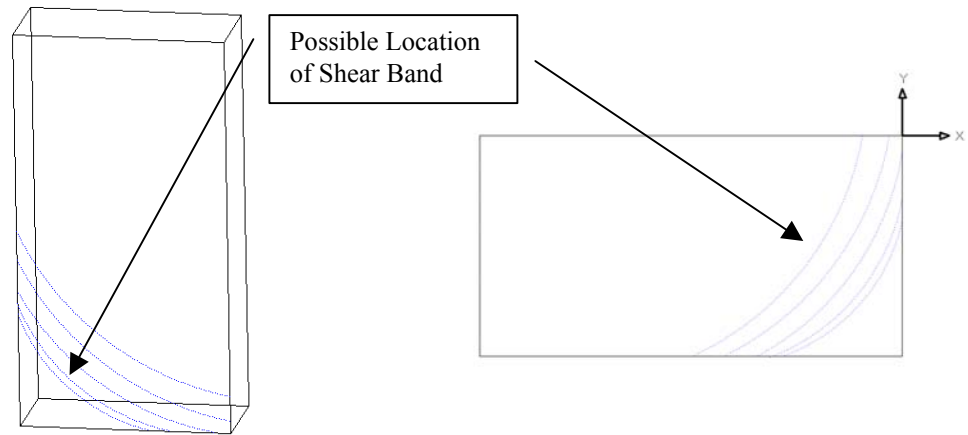


Figure 3.9 Schematic View of the Coupon Cut from Specimen MT14



(a) 3D View of the Coupon Cut from MT14 and the Possible Shear Band

(b) 2D View of the Coupon and the Possible Shear Band Direction

Figure 3.10 Estimate Shear Band Position in the Coupon

After cutting, the coupon was placed in a mounting cup with epoxy for later serial grinding (Figure 3.11). Four conical and four cylindrical holes were drilled through the sample before processing. The four cylindrical holes were used to align the slices during 3-D reconstruction. The four conical holes were used to check the removal thickness between two adjacent slices. A schematic sketch of the drilling pattern is shown in Figure 3.12. The vertex angle of the cones is 60° . The removal thickness was determined based on the change of the diameter of the base circle of the cone on each slice. An explanation of the calculation of slice distance is shown in Figure 3.13.

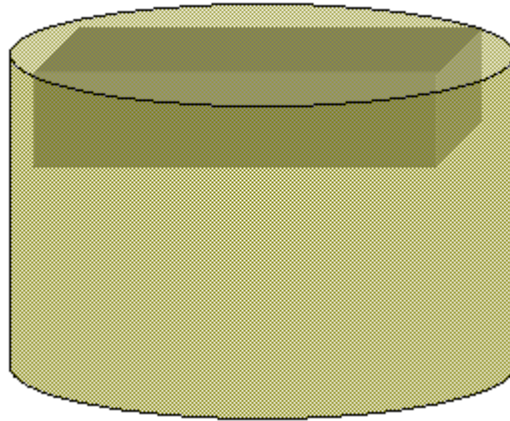


Figure 3.11 Sample Block in Mounting Cup

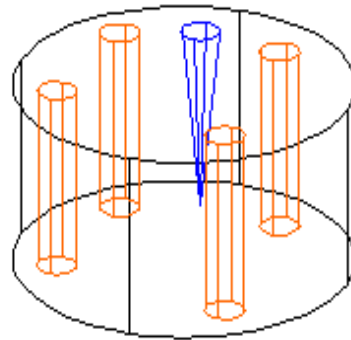


Figure 3.12 Cylindrical and Conical Holes Drill Pattern

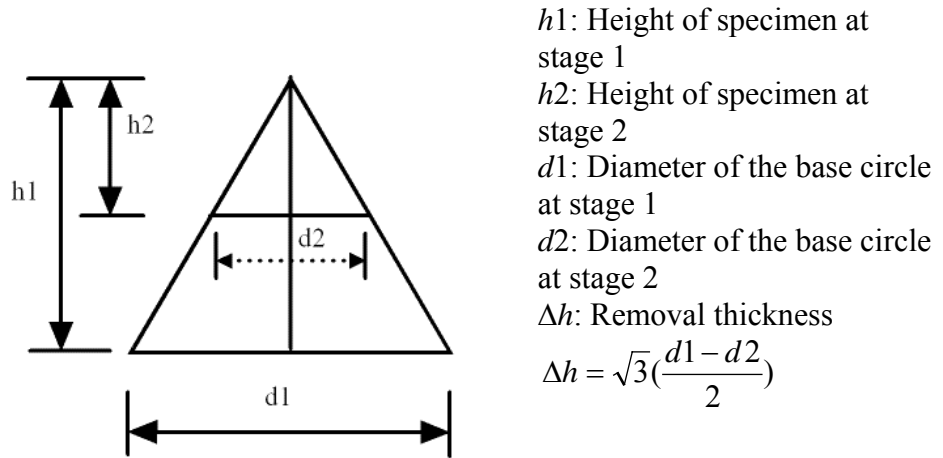


Figure 3.13 Illustration of Removal Thickness Calculation with Conical Holes

3.4.2 Serial Grinding

Serial grinding has been extensively used in the field of biomedical science, materials science and palaeontology. However, this is the first time it has been applied in the study of structure of sand. Serial grinding involves removing a small thickness of material sequentially by abrasion and capturing an image of the surface at each stage.

In this study, a MultiPrep™ system from Allied High Tech Products Inc. was used to grind and polish the specimen. The polishing procedure materials are summarized in Table 3.4. The polishing steps are as follows:

1. Calibrate the MultiPrep™ system with two different platens.
2. Mount the sample to the polishing fixture.
3. Attach the 6 micron Dia-Grid to one platen and the Gold Label polishing cloth to the other.

4. Attach the polishing fixture to the MultiPrep™ and begin to polish with the Dia-Grid until the specimen surface is parallel to the disc.
5. Place the fixture into the Dial Indicator system (Figure 3.14) and “zero” it.
(The dial indicator is used with the remote cable which allows lifting of the spindle without altering dial position during the measurement of the removal thickness. The dial indicator displays both metric and standard in 1 micron/0.00005" increments.)
6. Reattach the fixture to the MultiPrep™ and grind for about two minutes. Due to condition and wearing of the polishing cloth, the time may vary. Adjustment may be needed at different stages of grinding.
7. Clean the sample with water and re-measure with the Dial Indicator system.
8. Verify that approximately 8 micron has been removed.
9. Proceed with 1 micron compound on the Gold Label Cloth following the parameters in the polishing procedure for about 30 seconds.
10. Capture images and check the removal thickness by measuring the diameter of the cone holes.

For the four specimens in this study, at least 600 slices were obtained from each sample by serial grinding and polishing.

Table 3.4 Polishing Procedure Using MultiPrep™ System

Step	1	2
Abrasive Size and Type	6 micron Dia-Grid Diamond Discs	1 micron Diamond Compound
Polishing Cloth	N/A	Gold Label
Extender	BlueLube™	BlueLube™
Head Rotation	Full (High Speed)	Full (High Speed)
Head Oscillation	1" range	1" range
Sample Load	Full	Full



Figure 3.14 Dial Indicator and Remote Cable for Removal Thickness Measurement (Allied High Tech, Inc.)

3.4.3 Image Capture and Mosaic Generation

At the end of each grinding step, images were taken for each section. A Leica DM4000 microscope and Leica QWin software were used to capture the images. The resolution used was 7.83 micron per pixel. The size of each image was 640 x 480 pixel which covers an area of 5.01 x 3.76 mm. It is noted that the removal thickness of 8 micron at each stage was determined based on the 2-D resolution of the image. In this way, the reconstructed three-dimensional structure had equal resolution in the x, y, and z directions which was crucial for further analysis of the structure. The details of this process will be discussed later.

To make sure the images of each section were captured at the same position (no translational or rotational movement allowed), a fixture was designed to hold the polishing fixture and the sample on the microscope stage. This is important for the later automatic alignment of the slices. The dimensions of the fixture are shown in Figure 3.15. A 3-D schematic sketch of the fixture and a photo showing the fixture holding the polishing fixture and a sample on the microscope stage are shown in Figure 3.16.

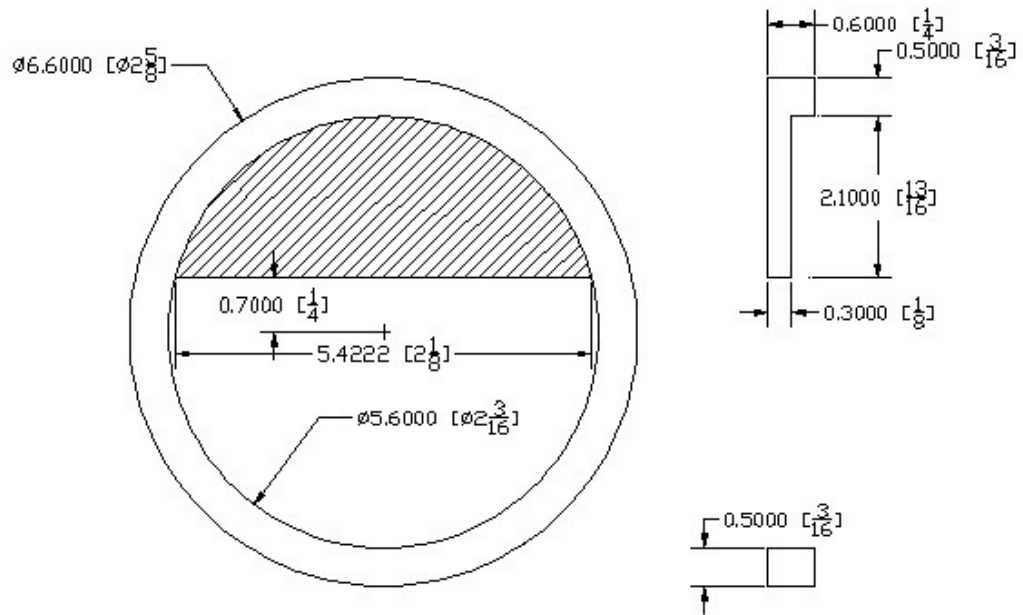
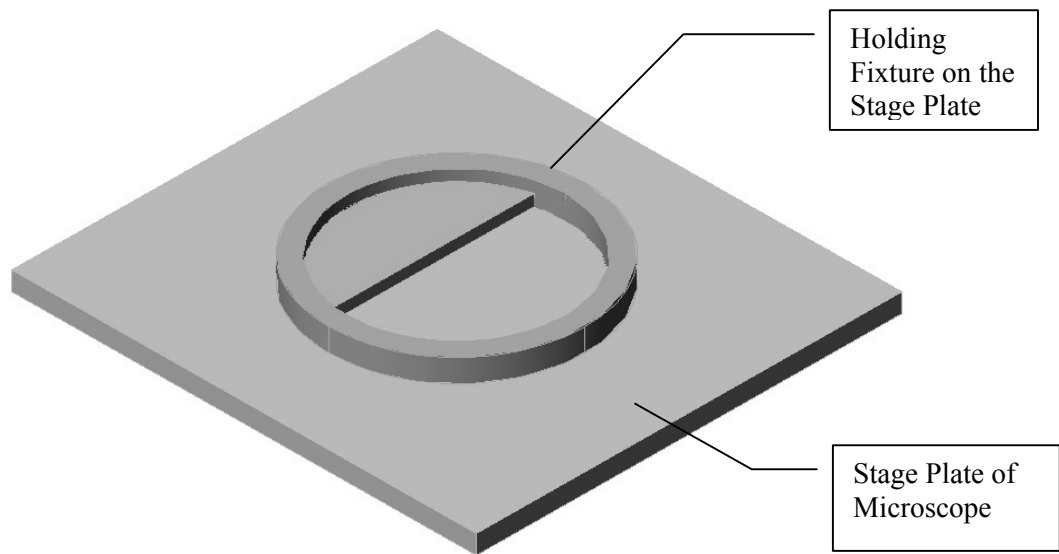
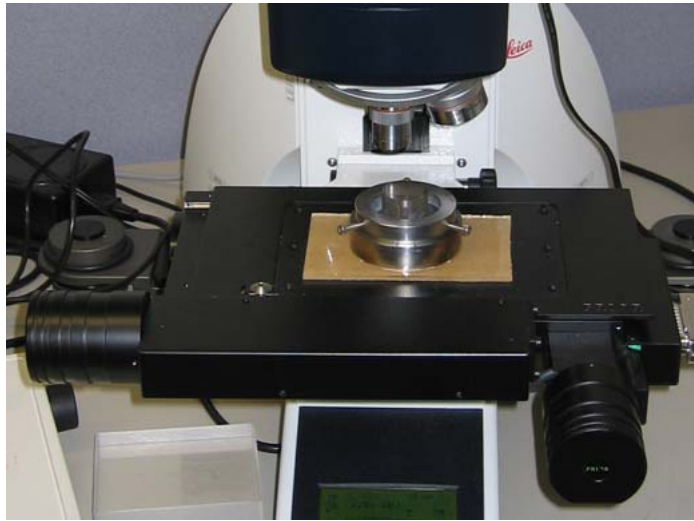


Figure 3.15 Dimensions of the Holding Fixture



(a) 3D Schematic Sketch



(b) Holding Fixture and Specimen on the Microscope Stage

Figure 3.16 Holding Fixture to Ensure Correct Alignment of Specimen

In 2-D imaging, to get a large area view of an object, a lower magnification is used which means a low resolution. Consequently, this may result in loss of some details and accuracy of measurement of features. To obtain both a large field of view and a high resolution, a mosaic technique was applied. For each section, about 20 images in a 5 x 4 pattern (Figure 3.17) were captured contiguously with an overlap of about 20% of each edge of an image with the adjacent images.

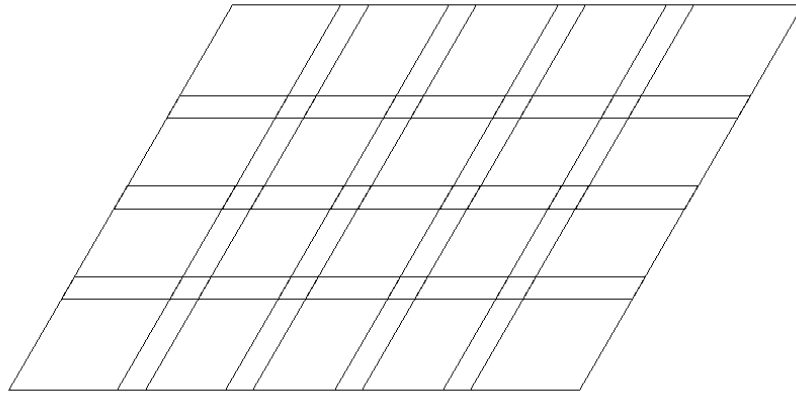


Figure 3.17 Sketch of Mosaic Pattern

An example of the overlap between four neighboring images is shown in Figure 3.18. This process was automated by setting up the program through the Leica Qwin system that controls the movement of the microscope stage in x and y directions precisely. The sample dimension information is listed in Table 3.5 and illustrated in Figure 3.19.

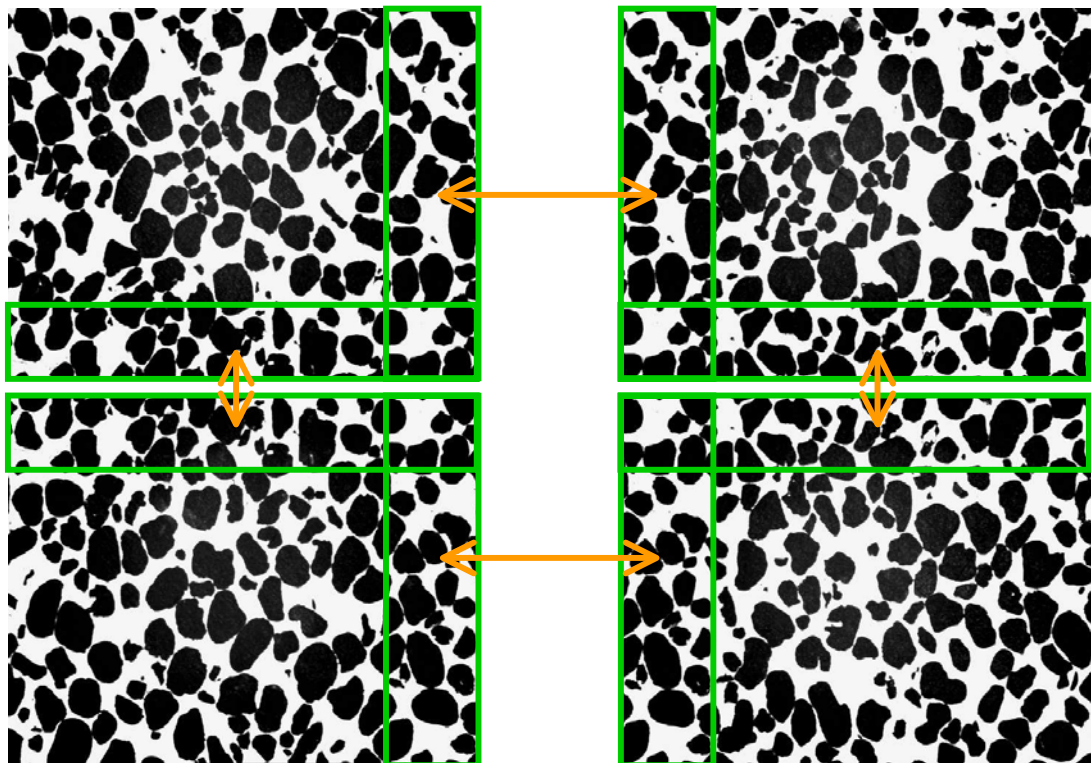


Figure 3.18 Illustration of Stitching of Four Neighboring Images

Table 3.5 Information of Three-Dimensional Structure

Property	Dimensions
Height	5 mm
Slice Spacing	8 micron
Pixel Resolution	8 micron
Total Pixel Area	2465 x 1465
Serial Sections	600
No. of Features in sample	35,000 ~ 40,000

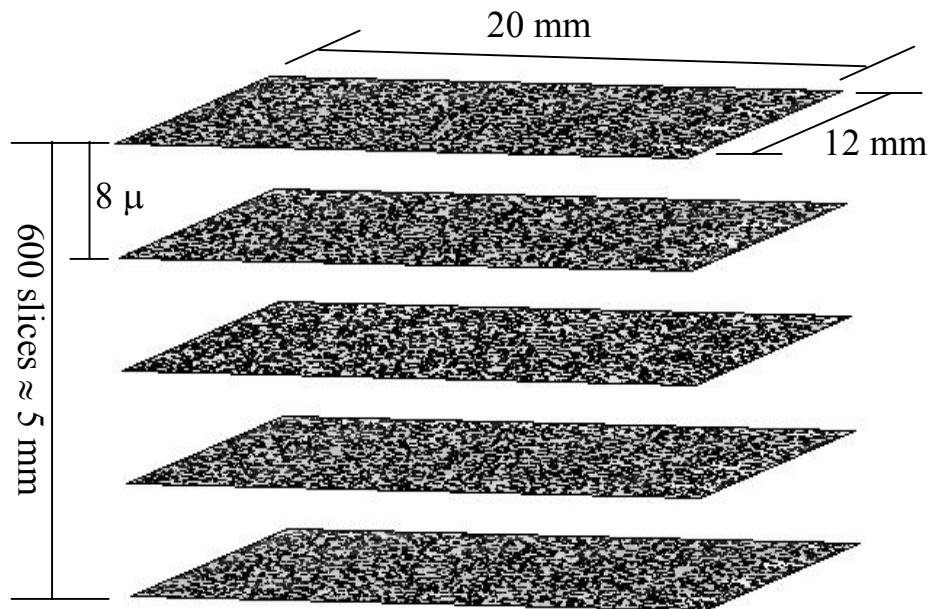


Figure 3.19 3-D Dimension Information of the Sample

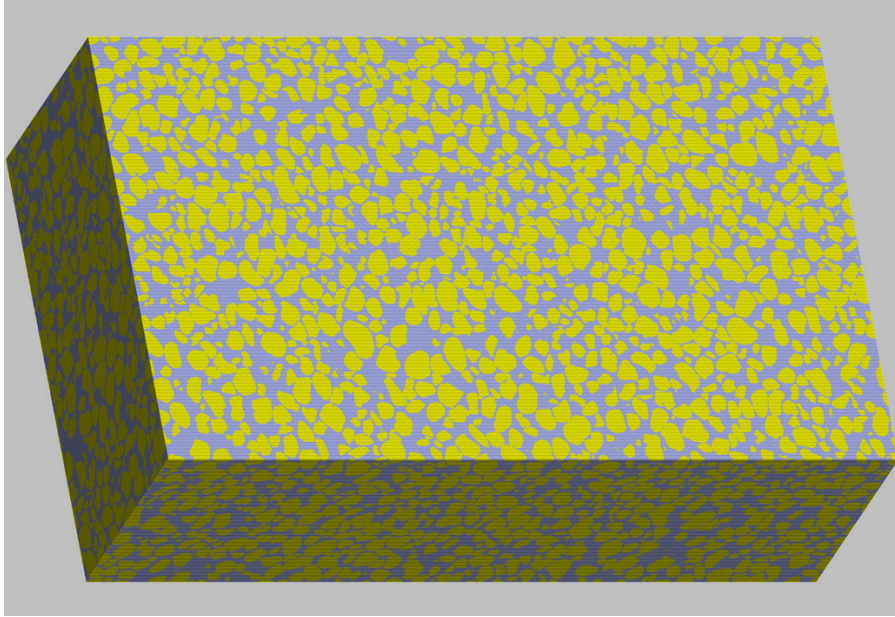
3.5 Three-Dimensional Reconstruction

3.5.1 Alignment

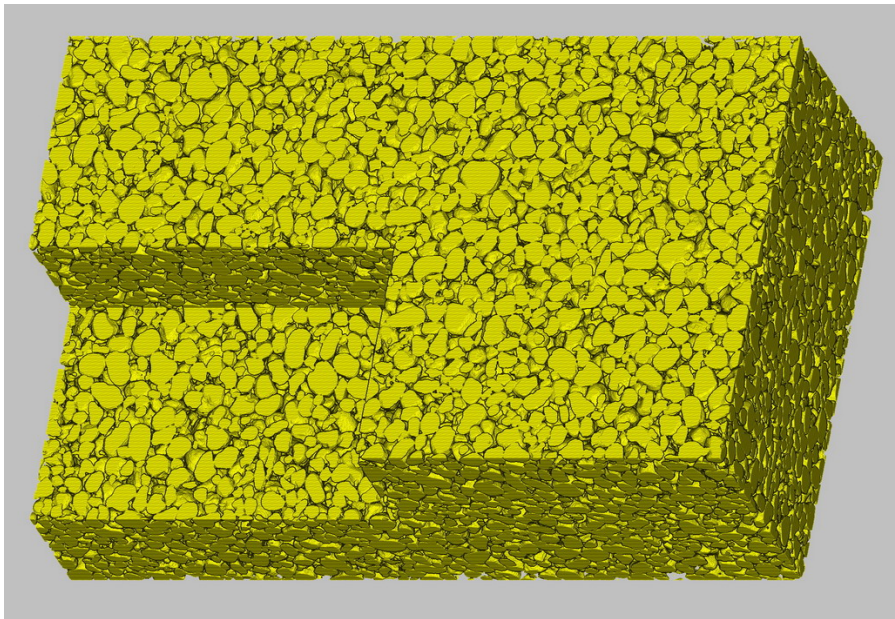
After a set of 2-D slices were obtained and before reconstruction of the 3-D structure, alignment was performed to correct any possible small movement that occurred during the capturing of the images within one pixel. In this research, the software ImageJ from NIH with the plugin RegisterROI by Abramoff (2004), was applied to align the slices.

3.5.2 Reconstruction

After alignment, slices were loaded into the software VoxBlast for reconstruction. VoxBlast used these stacks of aligned 2-D images to create 3-D projections from any viewpoint using an alpha blending or surface rendering algorithm. Figure 3.20 (a) is an example of the reconstructed 3-D structure from 600 image slices. Each image slice consists of 1800 x 1100 pixels. This structure represents a sample coupon size of 14mm x 9mm x 5mm. There are approximately 20,000 sand particles in the volume and it is based on about 12,000 individual images captured from the microstructure. Figure 3.20 (b) is a reconstructed volume with 1/8 of the volume cut from a corner to show the inside particles. A small sub-volume is shown in Figure 3.21. This shows the complete structure (particles and pores) in Figure 3.21(a) as well as the particles (Figure 3.21 (b)) and pore structure (Figure 3.21 (c)) separately.

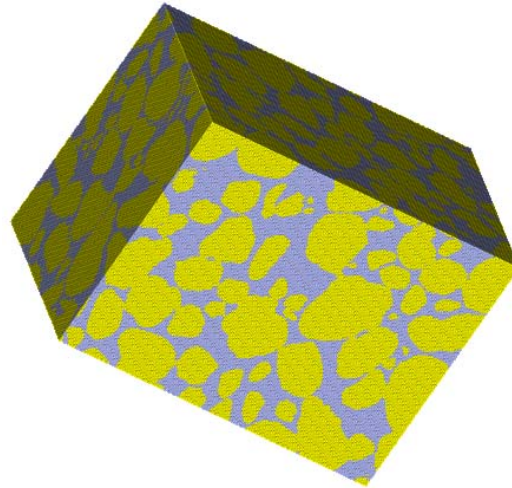


(a) 3D Reconstructed Structure (Yellow: Sand Grains; Blue: Pore Space)

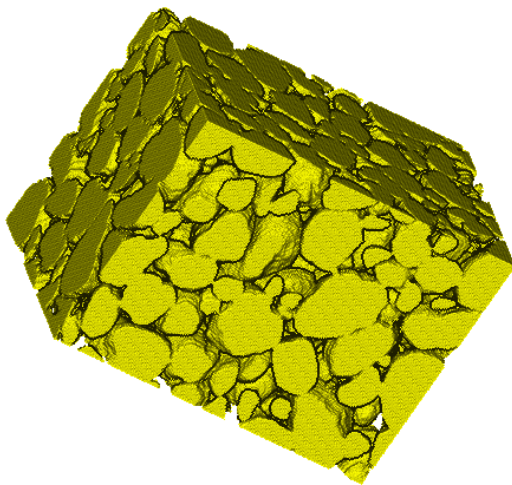


(b) An Inside View of the 3D Structure

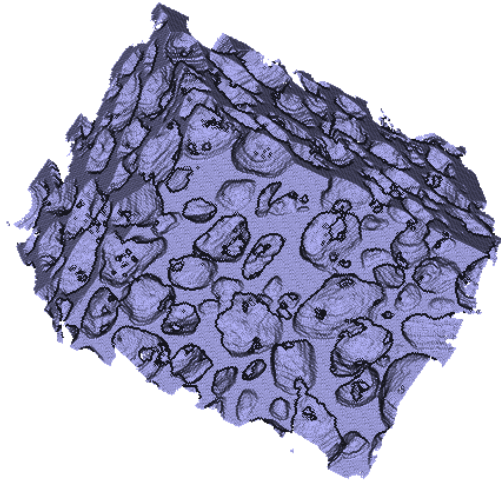
Figure 3.20 An Example of the 3D Reconstructed Structure



(a) Sub-Volume



(b) Particles

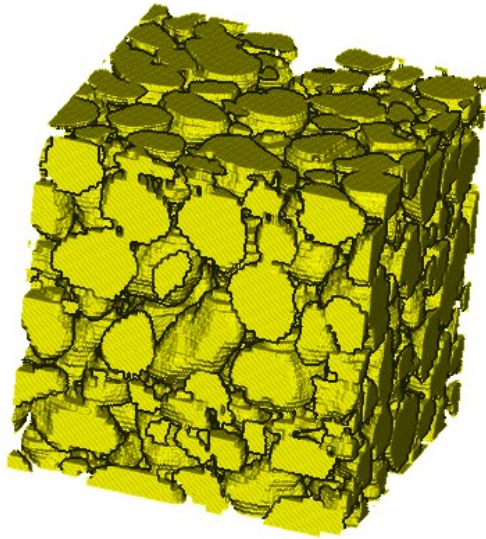


(b) Pores

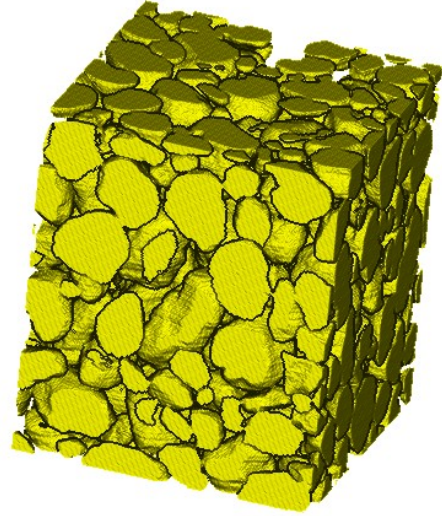
Figure 3.21 Sub-volume of the Sample and Extracted Structures of Particles and Pores

In this study, an 8 micron slice spacing was used during serial grinding, which ensured the same resolution was used in the reconstructed structure in the x, y and z directions. If a spacing of value larger than 8 micron were used, it would mean that the

volume would be undersampled in the z direction. VoxBlast can add interpolated slices in the z direction between the real slices when the resolution in z direction is lower than that in x-y plane. This will stretch the volume and make the reconstructed structure appear correct. However, when subsequently reslicing the volume in an arbitrary direction (Figure 3.22), it would result in a blurred image (Figure 3.22) and this image can not be efficiently used in further 2-D image analysis. With the reconstructed 3-D volume, it is possible to quantify the features of interest in the specimen.



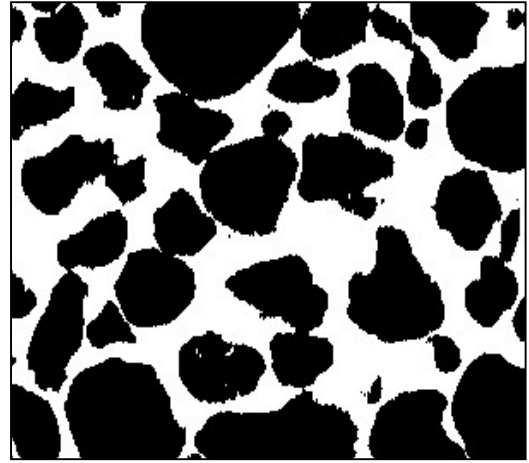
(a) 3D Structure with z Resolution of 40 micron



(b) 3D Structure with z Resolution of 8 micron



(c) 2D x-z Image with z Resolution of 40 micron



(d) 2D x-z Image with z Resolution of 8 micron

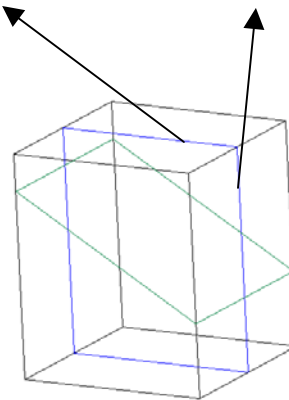


Figure 3.22 Comparison between Different z Resolutions

CHAPTER IV

SIMULATED STRUCTURE STUDY

4.1 Introduction

Once the three-dimensional coupon is reconstructed from the series of 2-D slices as described in Chapter III, it is possible to characterize both the solid and pore phases of the structure. In this study, a research software package, 3DMA (Lindquist, 1999), was used to quantify the structure three-dimensionally. Before the program was utilized with the coupons sectioned from the four triaxial test specimens, two simulated structures of idealized sphere packings were used to validate the program operation. In this chapter, an introduction to the package 3DMA is presented. This is followed by the 3-D characterization of two idealized sphere packing structures: simple cubic packing (SCP) and face-centered packing (FCP). Furthermore, a series of 2-D analysis were performed on the 2-D slices of the SCP and FCP structures.

4.2 Introduction to 3DMA Software Package

The 3DMA software package is based on the application of medial axis analysis to quantify a 3-D bi-phase structure. It is important to note that 3DMA is currently a research software package. In other words, the software has a current set of capabilities however it is very much in a development stage. The application of the software in this

present study has identified some scenarios that it could not resolve and these have led to enhancements made by the developer.

The first step in analyzing a volume with 3DMA is to obtain the skeleton or medial axis of the phase of interest in the material. The medial axis can preserve the characteristics of the structure both topologically and geometrically. It is defined as the “spine” of the object running along its geometric centers (Lindquist and Lee, 1996) and can be created using a process called skeletonization. Skeletonization is a thinning process and has been described by Fisher et al (2003): “Imagine that the foreground regions in the input binary image are made of some uniform slow-burning material. Light fires simultaneously at all points along the boundary of this region and watch the fire move into the interior. At points where the fire traveling from two different boundaries meets itself, the fire will extinguish itself and the points at which this happens form the so called ‘quench line’. This line is the skeleton. Under this definition it is clear that thinning produces a sort of skeleton.” This skeletonization process is also called medial axis transformation.

After the medial axis is constructed, the minimum cross sectional area (called throat) of each channel in the pore space is determined. This involves two steps (Lindquist, 1999): (1) determining the throat perimeter; (2) spanning the throat surface. Three algorithms can be used to calculate the throats. One is a “wedge finding” algorithm (Shin, 2002) which uses wedges in a cylindrical coordinate system to construct throats. The second one was developed by Lindquist and Venkatarangan (1999) by applying the Dijkstra shortest path algorithm to locate the bounding perimeter of the throat surfaces.

The third is a sub-sectioning throat algorithm for higher porosity media (Prodanovic, 2005). In this present research, the “wedge finding” algorithm was used.

After the throats are constructed, the pore space is partitioned into a series of pore bodies separated by the throat surfaces (Lindquist 1999). Throat/pore body network statistics can be obtained from the partitioned structure. This whole pore space characterization process is demonstrated and validated for two idealized specimen structures in this chapter. The path lengths and tortuosity based on the medial axis between two opposite faces in a structure can also be calculated after the medial axis is constructed. The process using 3DMA to characterize a bi-phase structure is summarized in Figure 4.1.

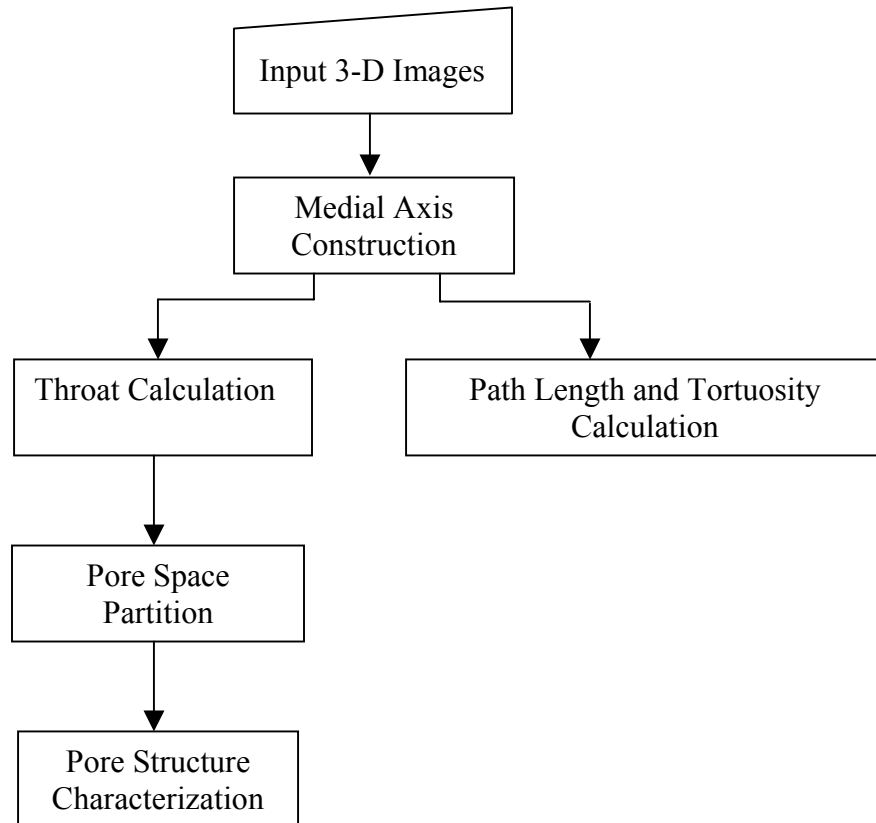


Figure 4.1 Flow Chart of Medial Axis Analysis in 3DMA

4.3 Medial Axis Analysis on Simple Cubic Packing

To evaluate the performance of the 3DMA software program, analysis was first conducted using a simple cubic packing (SCP) specimen.

4.3.1 Structure Information

The simple cubic packing consists of 5 x 5 x 5 spheres each with a radius of 25 pixels. The theoretical porosity of an SCP structure is 0.476. The 3-D SCP structure is visualized in Figure 4.2. A summary of the structure information is listed in Table 4.1.

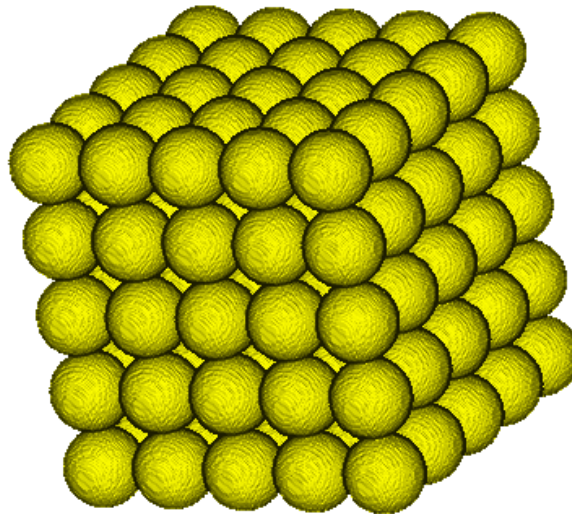


Figure 4.2 3-D SCP Structure

Table 4.1 SCP Structure Information

Sphere Radius	25 pixels	
Sphere Size	65,449 voxels	
Packing size	5x5x5 spheres	
Total Volume	250x250x250=	15,625,000 voxels

4.3.2 Medial Axis Analysis on SCP

Figure 4.3 represents the medial axis or skeleton of the entire SCP structure (internal and external) obtained from 3DMA. An integer distance value is assigned to each pore voxel. Colors on the medial axis voxels represent the relative distance (red - close, blue - far) from the voxel to the nearest particle surface (Lindquist, 1999).

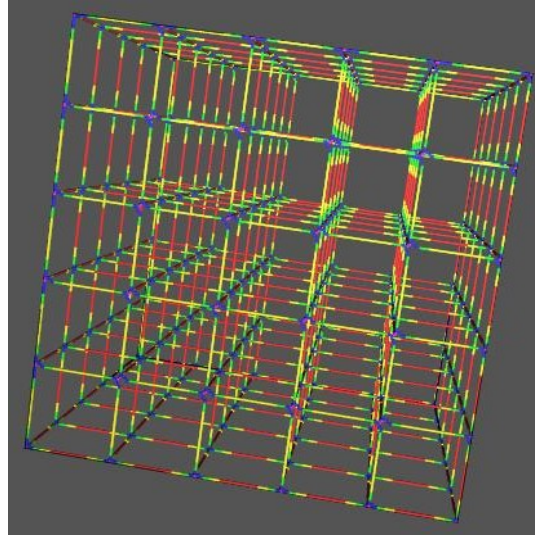


Figure 4.3 Medial Axis of an SCP Structure

The internal throats of the structure are shown in Figure 4.4. The medial axis and the throats are plotted together (Figure 4.5) for a clear representation of the relative positions of the throats and the medial axis. A single pore that is surrounded by the parts of the adjacent spheres and the calculated throats is shown in Figure 4.6.

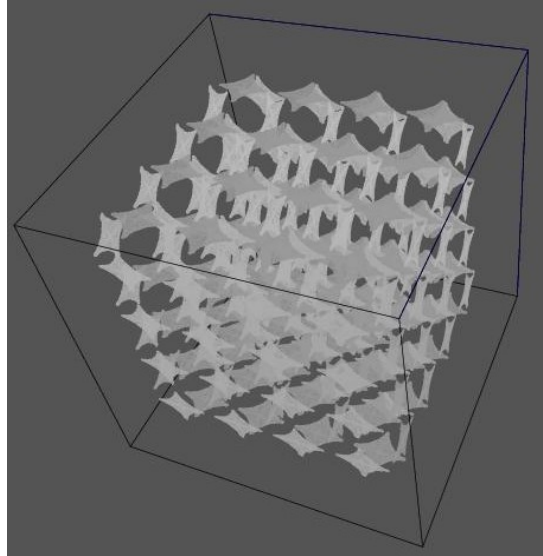


Figure 4.4 Throats of the Pore Space in an SCP Structure

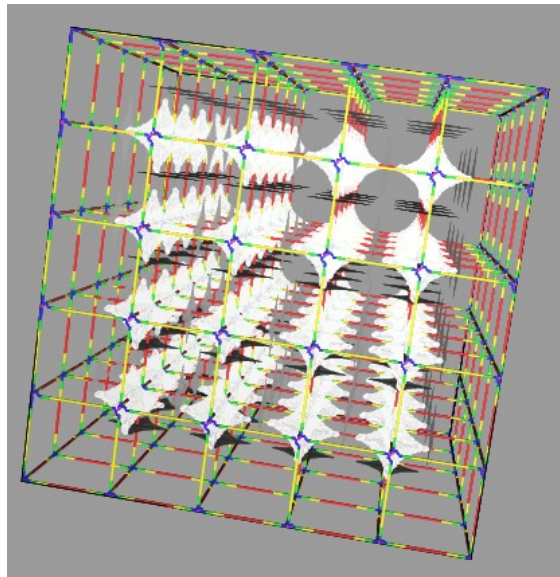


Figure 4.5 Medial Axis and Throats of SCP

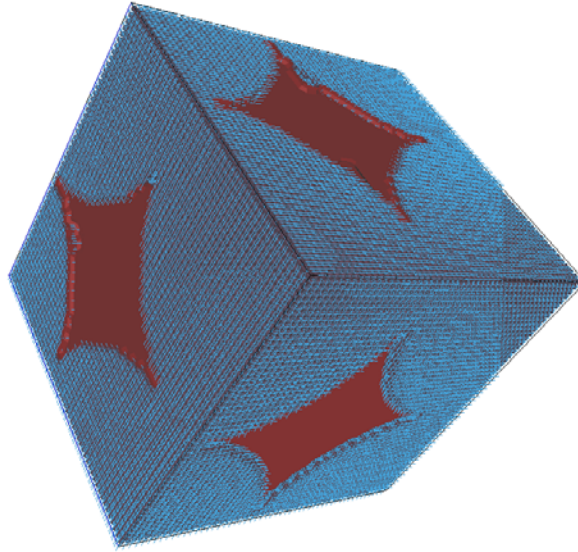


Figure 4.6 A Unit Pore Structure in SCP

3DMA correctly identified 64 internal pores (no throats touching the edge) in this 5 x 5 x 5 SCP structure. In this symmetrical structure, each pore has the same volume of 57,688 voxels. The total volume of the exterior pores that touch the boundary is 3,554,993 voxels. The pore structure quantification results are listed in Table 4.2. The total volume of the pore space is 7,247,025 voxels.

Table 4.2 3DMA Measurements of SCP

		Volume (voxels)
Individual Interior Pore	64 internal pores	57,688
		57,688
		57,688
		...
		57,688
		57,688
		57,688
		57,688
	Total→	3,692,032
Pores that touch the edge		3,554,993
Total Pore Volume		7,247,025
Porosity		0.464

The measurement results are also compared with the theoretical values of SCP, and are listed in Table 4.3. The theoretical porosity of SCP is 0.476, while the 3DMA measurement result is 0.464. The difference of 2.5% is attributed to digitization error (e.g. the finite size of a voxel).

Table 4.3 Comparison between Theoretical Values and 3DMA measurements

	Theoretical Values		3DMA Values	Error (%)
Porosity	$1-\pi/6$	0.476	0.464	2.5
Total Pore Size (voxels)		7,437,500	7,247,025	2.6
Each Unit Size (voxels)	50^3	125,000	N/A	N/A
Each Pore Size (voxels)		59,500	57,688	3.0

The individual internal pore volume measured by 3DMA is about 3% less than the theoretical value. Recognizing the aforementioned digitization error of about 2.5%, it can be concluded that pore space is partitioned accurately by 3DMA.

The pore size distribution plot and the throat surface area distribution are shown in Figure 4.7 and 4.8, respectively. It can be seen from Figure 4.7 that all pores have the same nominal size. For SCP, the throat size is expected to be the same for all of the throat surfaces found in the structure. However as shown in Figure 4.8, there are two values for throat surface area. This error results from the structure itself rather than the program because SCP was not constructed perfectly symmetrically due to the fact that the voxel size is finite.

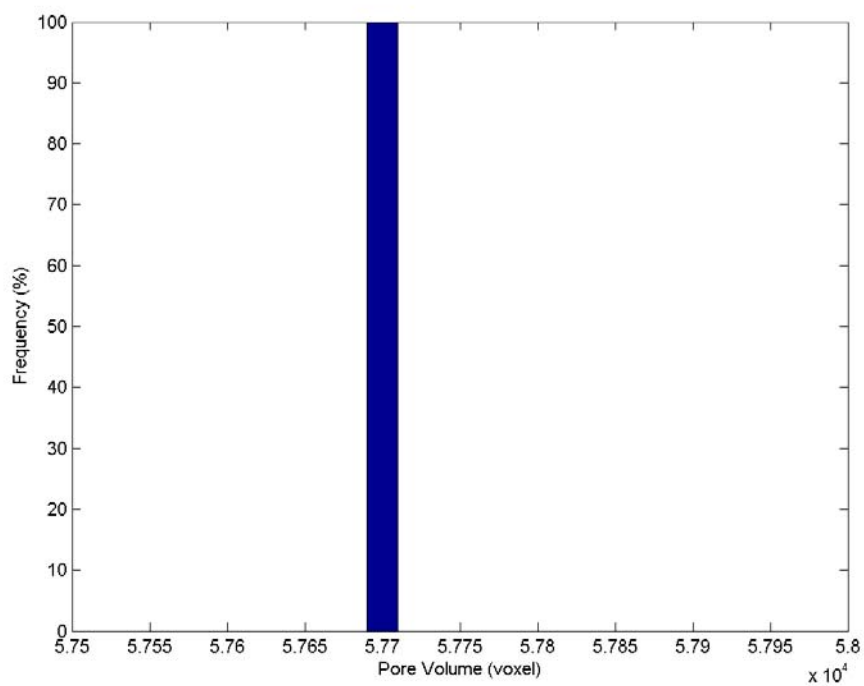


Figure 4.7 3-D Pore Size Distribution of SCP

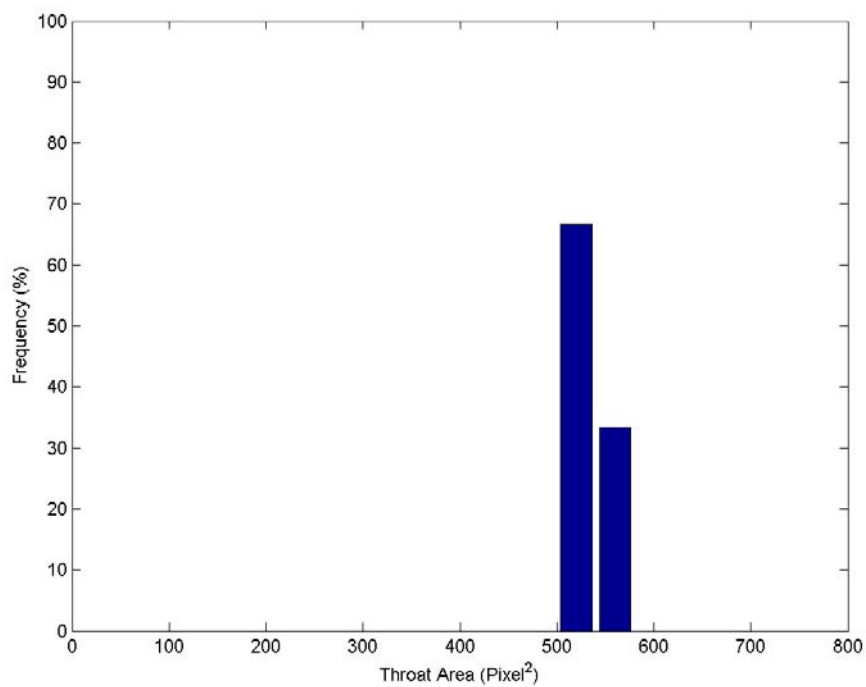
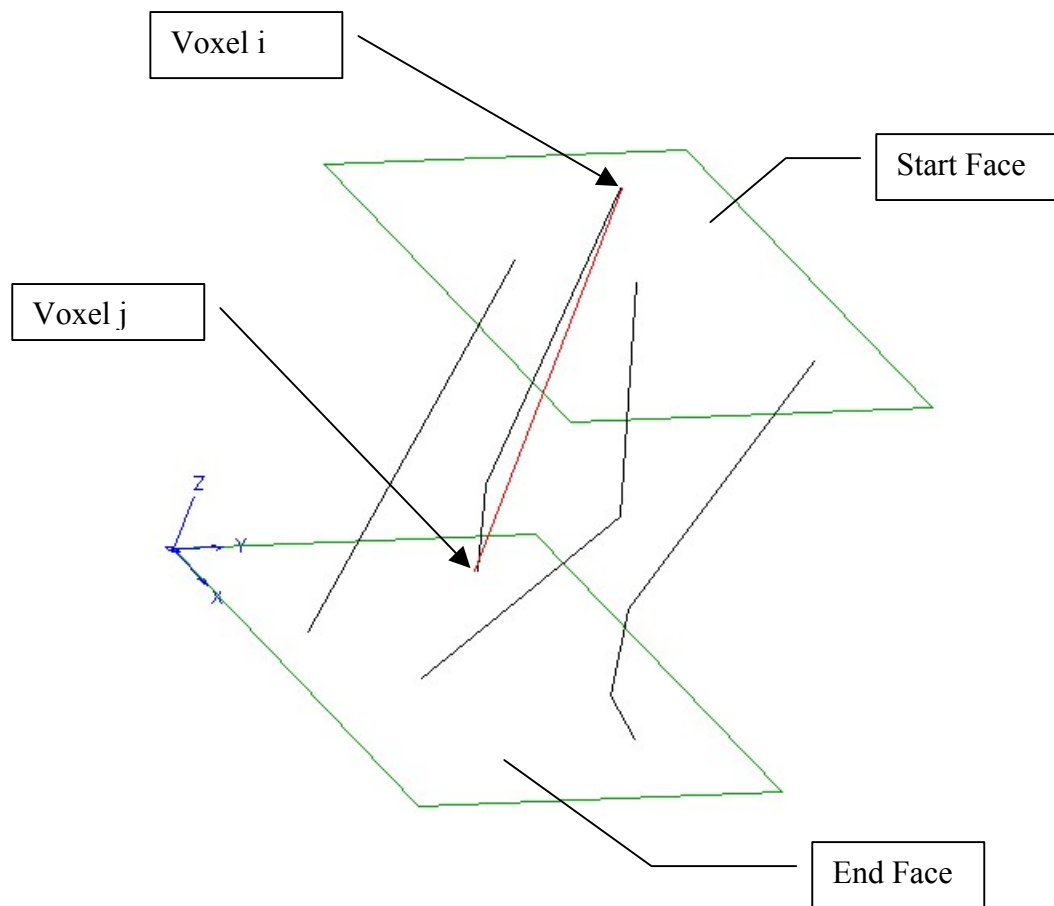


Figure 4.8 3-D Throat Size Distribution of SCP

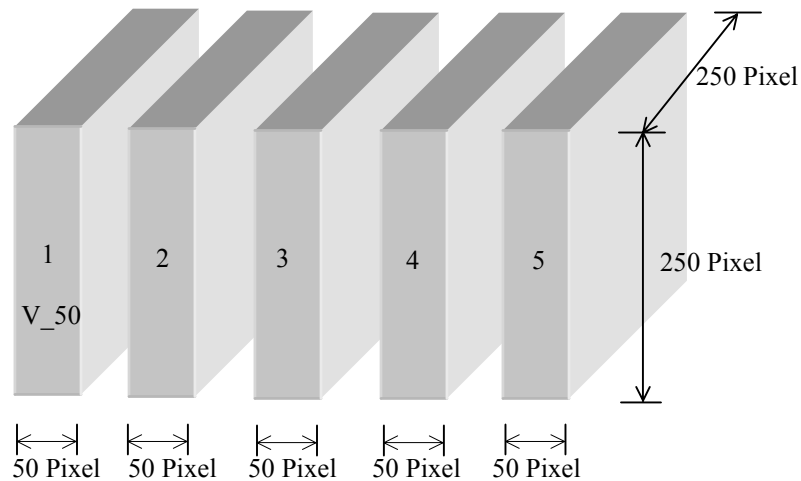
In 3DMA, the tortuosity of paths between two faces of interest can be calculated using the medial axis network. An illustration of the process is shown in Figure 4.9. From all the connected medial axis paths between each medial axis voxel i on the start face and each voxel j on the end face, 3DMA will find the shortest path between the pair of voxels i and j (Lindquist, 1999). The shortest path tortuosity is defined as the ratio between the shortest path length and the Euclidean distance between the voxels (Lindquist, 1999).



l_{ij} : Length of the shortest path between voxel i on the start face and voxel j on the end face;
 d_{ij} : Euclidean distance between voxels i and j ;
 t_{ij} : Tortuosity of the shortest path;
 $t_{ij} = l_{ij} / d_{ij}$;

Figure 4.9 Illustration of Path Length and Tortuosity Measurement in 3DMA

To study the effects of volume size (especially the length between two faces of interest) on the tortuosity calculation, measurements were performed on a series of sub-volumes (Figure 4.10 (a)-(b)) of the SCP structure. The mean tortuosity for each sub-volume of size 50 x 250 x 250 is 1.203, and is the same for all the sub-volumes as shown in Figure 4.11. The mean tortuosity and coefficient of variation for each sub-volume of cumulative size are listed in Table 4.4. Figure 4.12 and Figure 4.13 show that the mean shortest path increases linearly with the length between the two faces and the mean shortest path tortuosity decreases and gets close to a stable value when the length between two faces grows. The coefficient of variation of tortuosity (Figure 4.14) of each sub-volume decreases with the increased length between two faces. On the bases of the results presented in Figure 4.13, it can be seen that edge effects must be carefully considered in volume size used for analysis purpose.



(a)

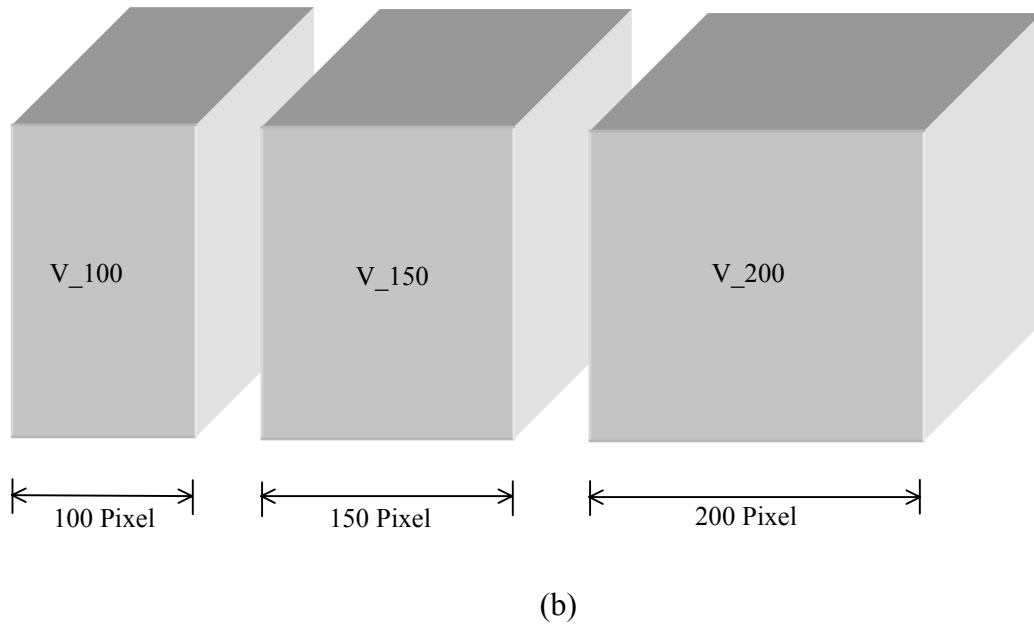


Figure 4.10 Sub-Volumes of SCP (a) Sub-Volumes of Same Size: 50 x 250 x 250; (b) Sub-Volumes of Various Length ($L \times 250 \times 250$; $L=i*50$, $i=1 \dots 5$)

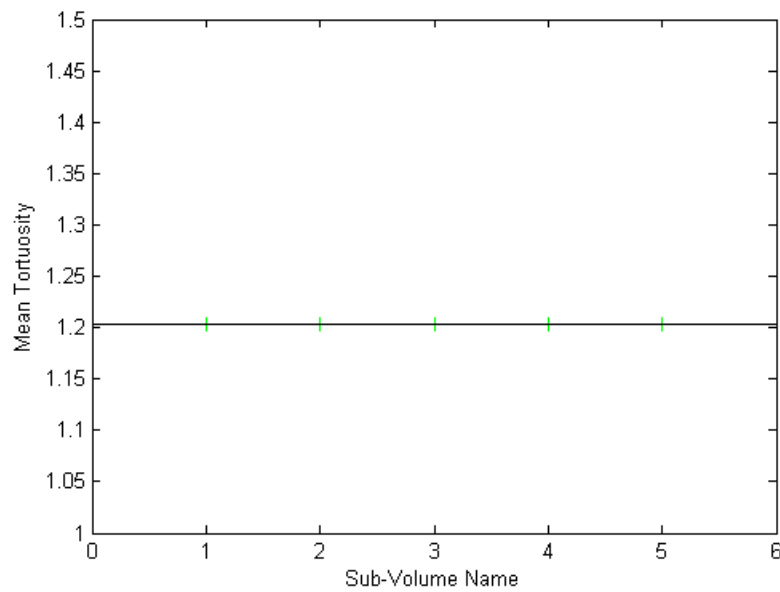


Figure 4.11 Mean Tortuosity for Each Sub-Volume of Size 50 x 250 x 250

Table 4.4 Mean, Standard Deviation and Coefficient of Variation of Tortuosity for Each Sub-Volume

Sub-Volume	V 50	V 100	V 150	V 200	V 250
μ	1.203	1.224	1.089	1.072	1.061
σ	0.100	0.062	0.044	0.034	0.028
CV (%)	8.30	5.06	4.05	3.21	2.67

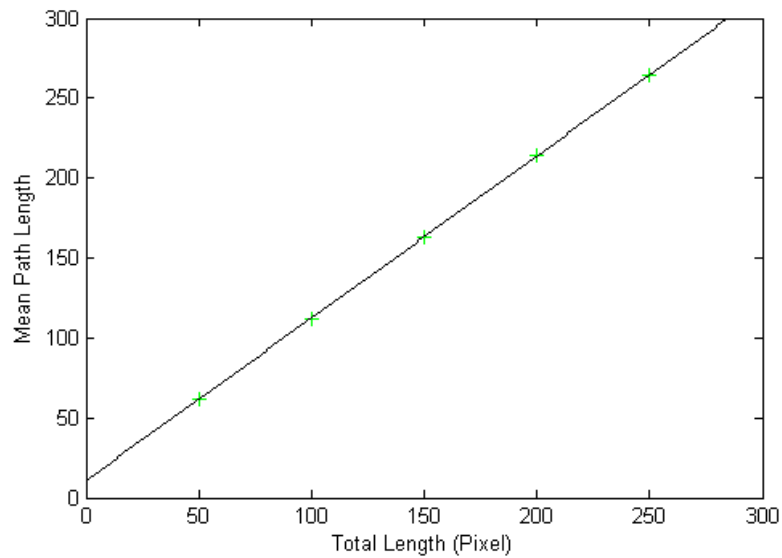


Figure 4.12 Mean Shortest Path Length for Each Sub-Volume of Various Lengths (50, 100, 150, 200 and 250 Pixel)

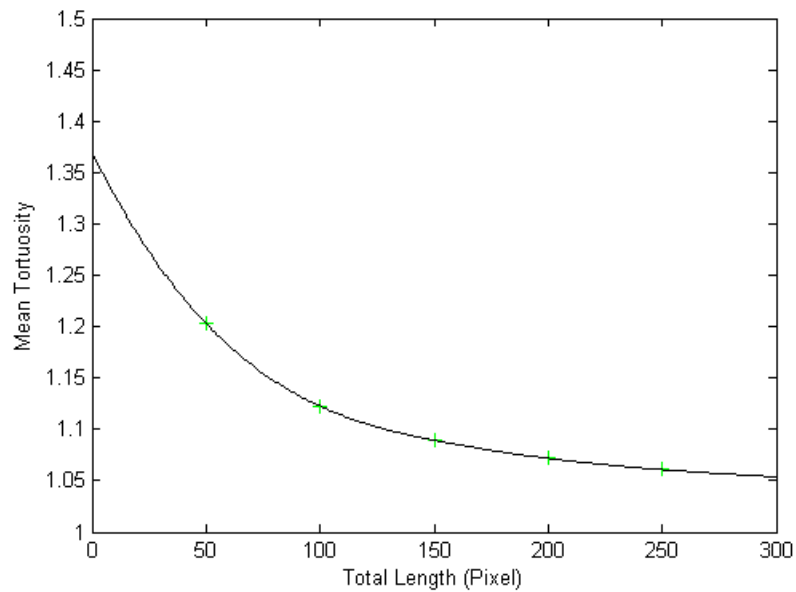


Figure 4.13 Mean Tortuosity for Each Sub-Volume of Various Lengths (50, 100, 150, 200 and 250 Pixel)

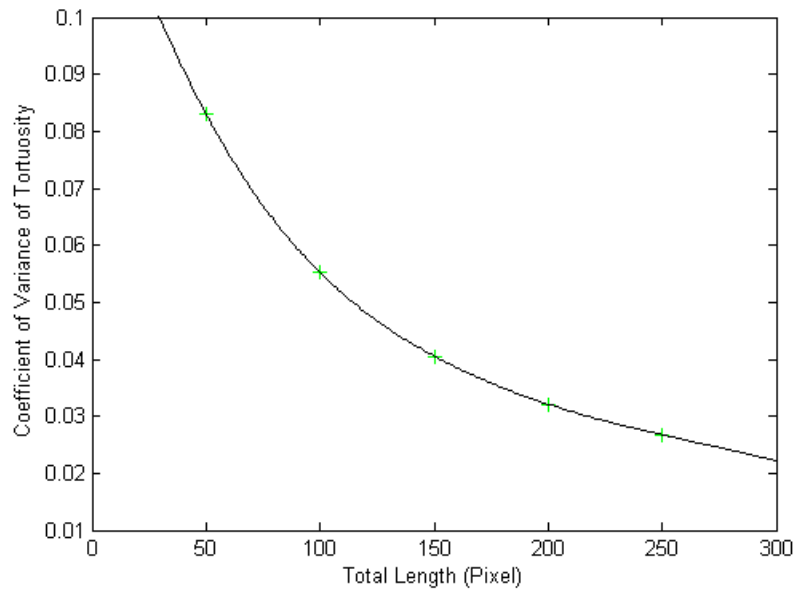
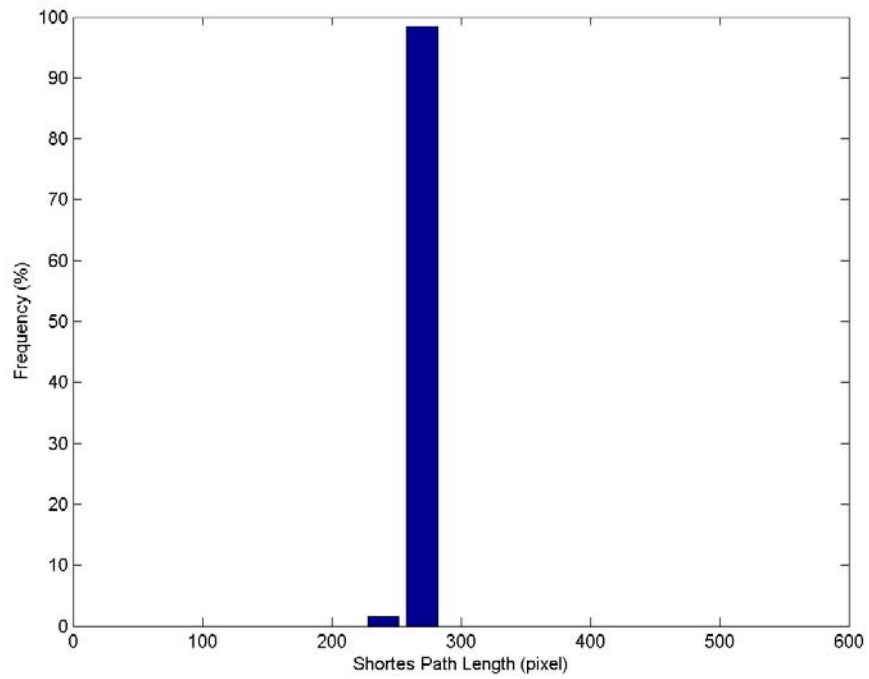
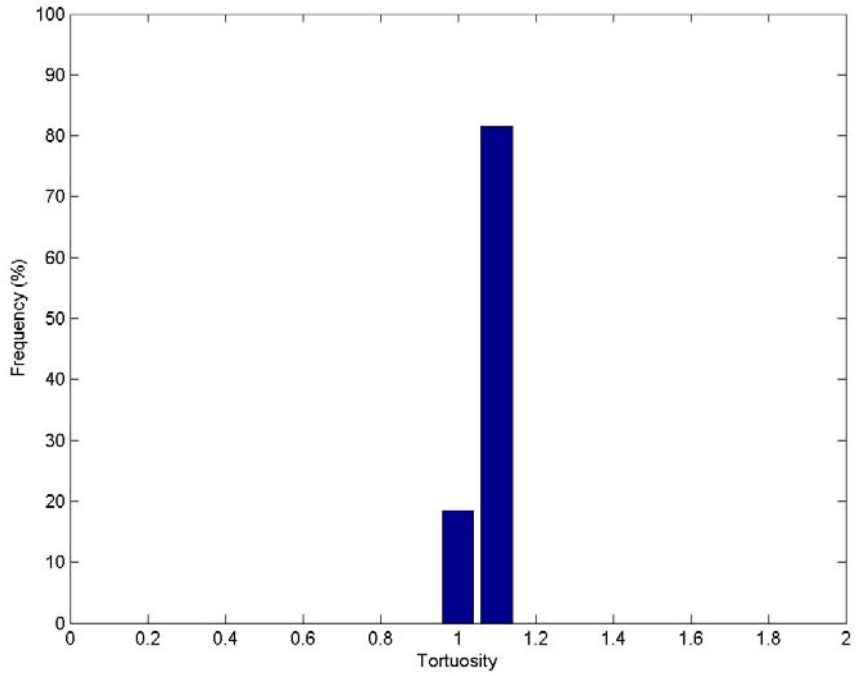


Figure 4.14 Coefficient of Variation of Tortuosity for Each Sub-Volume of Various Lengths (50, 100, 150, 200 and 250 Pixel)

The shortest path lengths and the corresponding tortuosities for SCP are shown in Figure 4.15. A total of 2900 starting nodes were identified which resulted in 2900 shortest paths being identified. The shortest path in an SCP structure is the path perpendicular to both the start face and the end face. Therefore, the relevant tortuosity should be 1. Most of the tortuosity values for the minimum shortest path in Figure 4.15 are between 1 and 1.1. If the structure is perfectly symmetrical everywhere, the values would be a single value of 1, instead of a range of the values. Figure 4.16 shows the shortest paths between two faces in the SCP specimen.



(a)



(b)

Figure 4.15 Shortest Path Characterization in SCP (a) Path Length Distribution for Shortest Paths of SCP; (b) Tortuosity Distribution for Shortest Paths of SCP

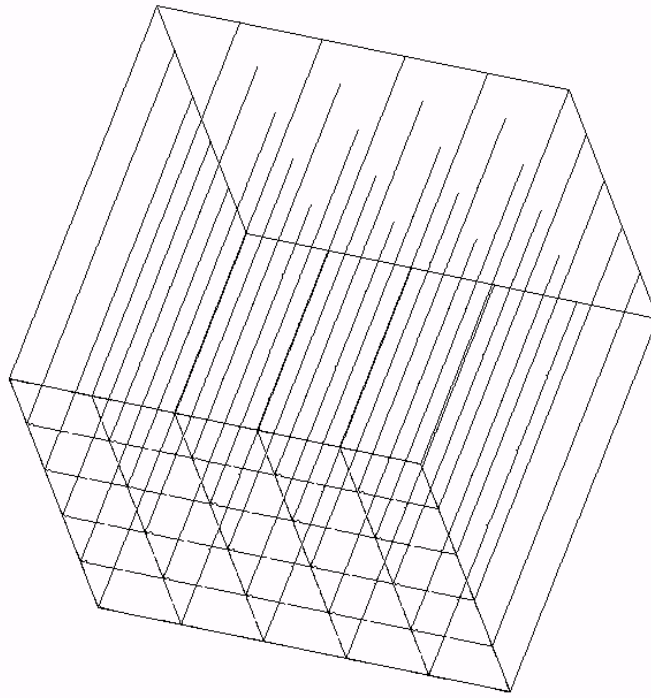


Figure 4.16 Shortest Paths in SCP

4.4 Medial Axis Analysis on Face-Centered Cubic Packing

A similar analysis was conducted with a face-centered cubic packing (FCP). The purpose of this additional validation study was to evaluate the 3DMA package where no straight paths existed between 2 faces of the specimens.

4.4.1 Structure Information

The specimen consists of spheres with radius of 25 pixels. The theoretical porosity of an FCP structure is 0.260. The FCP structure used in this study is shown in Figure 4.17. A unit of the FCP structure and the geometric information of the unit are also included in Figure 4.17. The information of the structure is listed in Table 4.5.

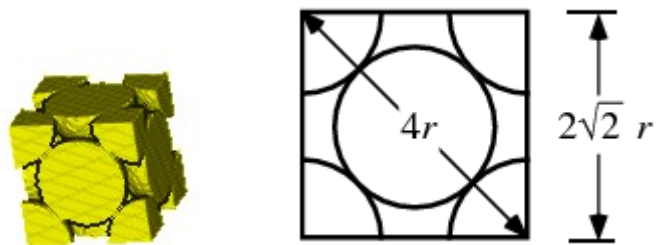
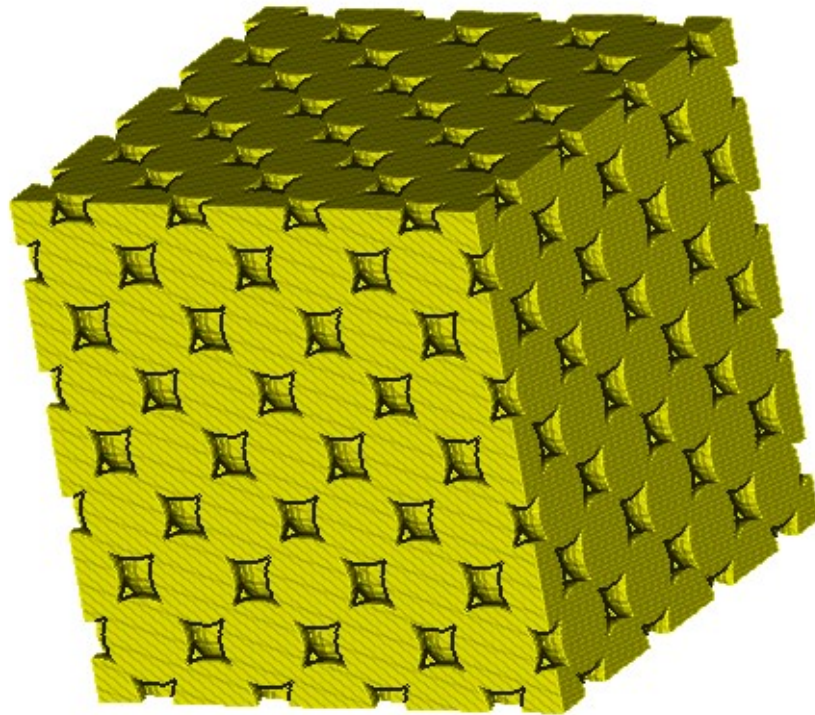


Figure 4.17 3-D Structure of FCP and Unit Information

Table 4.5 Structure Information of FCP

Sphere Radius	25 pixel	
Sphere Size (voxels)	65450	
Packing size	4x4x4 units (Unit Size= 70x70x70)	
Total Volume (voxels)	280x280x280=	21,952,000

During the pore-throat network analysis with 3DMA, it was found that if no contact or only a small contact area (say one voxel) exists between the spheres in the structure, no throats would be constructed with the algorithm provided in 3DMA. This was found to be due to the design logic of 3DMA that assumes that it is not possible to have isolated particles in geomaterials in 3-D space (Lindquist, 2005).

Accordingly, during the construction of the FCP structure, contacts of several voxels were created to get a reasonable pore space partition from 3DMA in the subsequent analysis. This explains the difference of porosity between the theoretical value and the calculated value from 3DMA.

4.4.2 Medial Axis Analysis on FCP

The medial axis of the entire FCP structure is shown in Figure 4.18, while the throats of the pore space are shown in Figure 4.19. Figure 4.20 represents the medial axis and throats of a unit cell of the FCP structure.

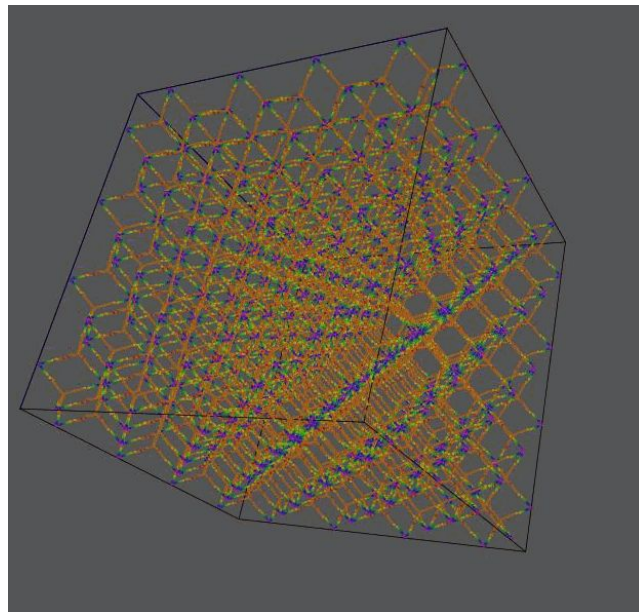


Figure 4.18 Medial Axis of an FCP Structure

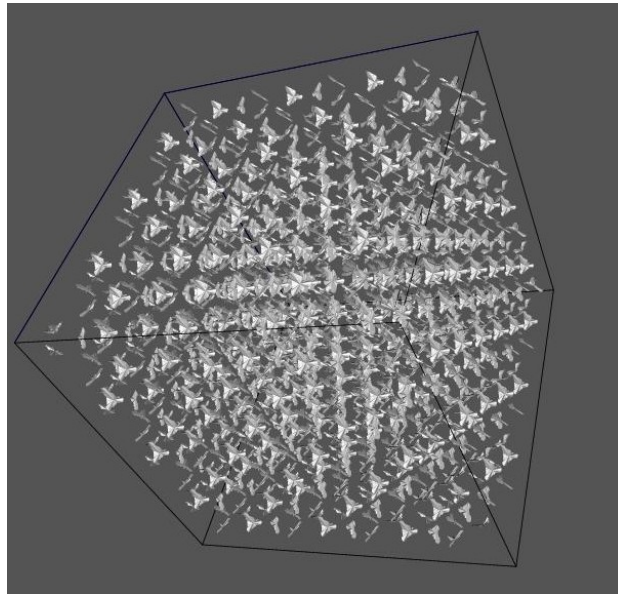


Figure 4.19 Throats of the Pore Space in FCP

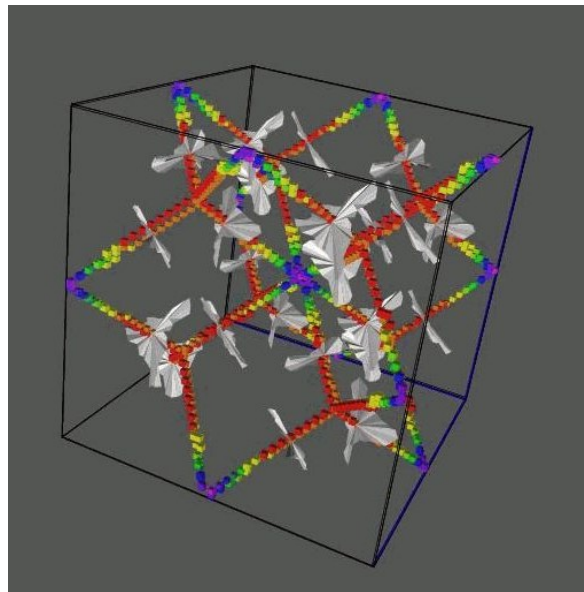


Figure 4.20 Medial Axis and Throats of a Unit FCP Cell

Pore structure characterization results are listed in Table 4.6 and Table 4.7. There are 165 internal pores found in the structure. The pore size distribution and throat size distribution are shown in Figure 4.21 and Figure 4.22 respectively. For pore size

distribution, if the structure were constructed perfectly symmetrically, the distribution of the throat size would be one single value.

Table 4.6 Internal Pore Size Information from 3DMA

Internal Pore Volume (voxels)	20010	20020	20277	20381	20978	20988	Total: 3,380,085
Number of Pores	9	63	3	18	9	63	Total: 165

Table 4.7 Comparison between Theoretical Values and 3DMA Measurements

	Theory Values	3DMA Result
Porosity	0.259	0.239
Total Pore Size (voxels)	5,860,501	5,248,982
Each Unit Size (voxels) $(2\sqrt{2}r)^3$	353,553	343,000

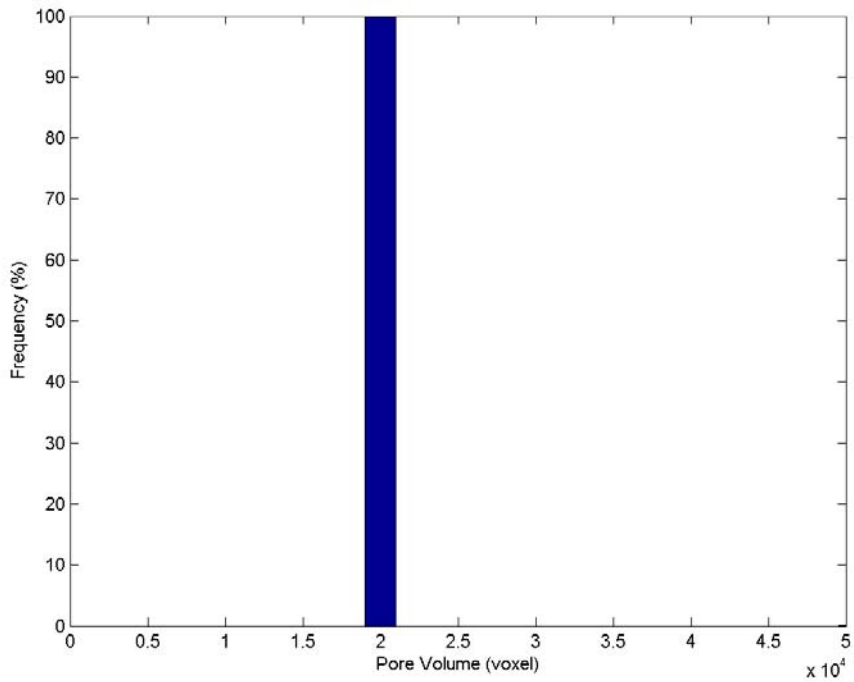


Figure 4.21 3-D Pore Size Distribution of FCP

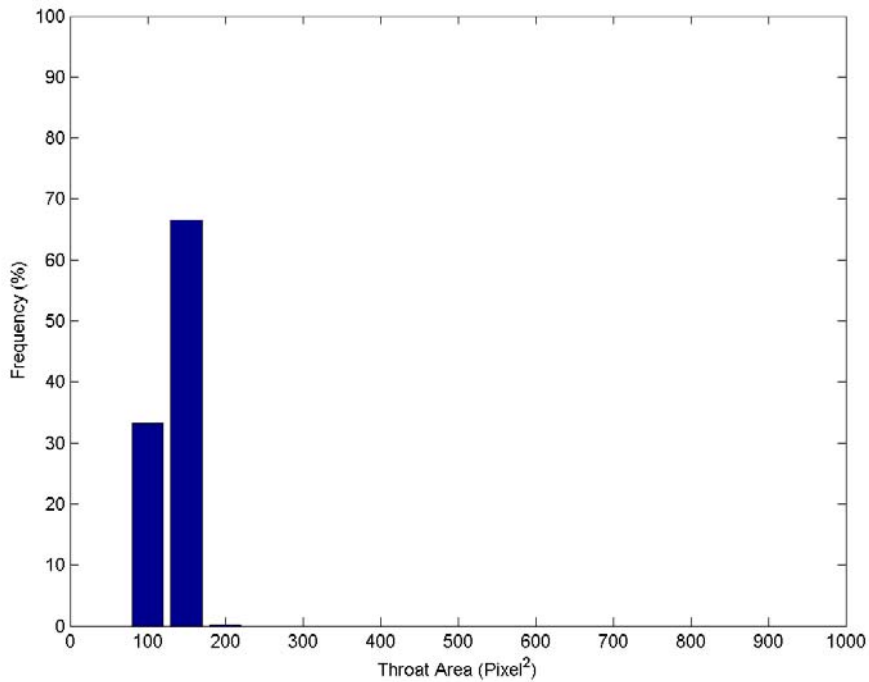


Figure 4.22 3-D Throat Size Distribution of FCP

The shortest paths between the two opposite faces are shown in Figure 4.23. The shortest path length and corresponding tortuosity is shown in Figure 4.24. From Figure 4.23, it can be seen that all the shortest paths display the same pattern. Therefore, the minimum shortest path lengths are expected to be the same for all the shortest paths. Figure 4.24 (a) is showing that all of the shortest path lengths of FCP are located in one bin. The tortuosities for these paths are also in a very narrow range (around 1.7), even though theoretically, they should be equal.

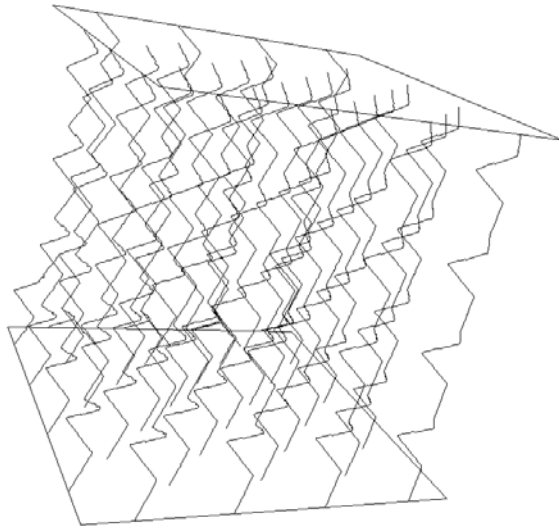
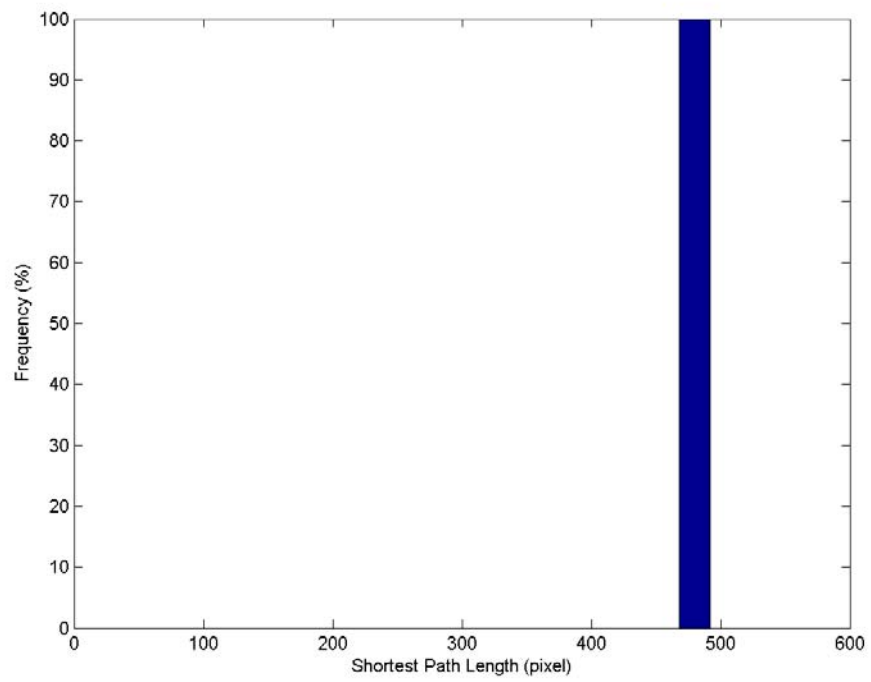
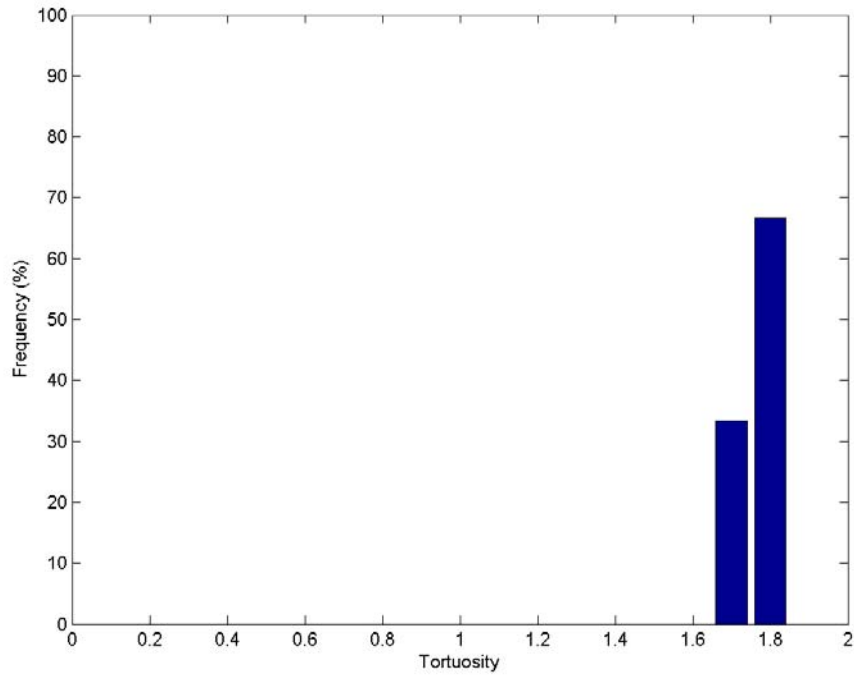


Figure 4.23 Shortest Paths between Two Faces in FCP



(a)



(b)

Figure 4.24 Shortest Path and Tortuosity Characterization in FCP (a) Path Length Distribution for Shortest Paths of FCP; (b) Tortuosity Distribution for Shortest Paths of FCP

4.5 Two-Dimensional Analysis of the Simulated Structures

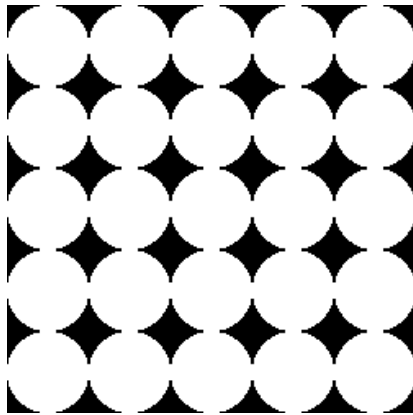
To complement the 3-D analysis results presented in this thesis, a number of 2-D analyses were also conducted to allow comparison of the results of the present study with those from earlier 2-D studies by Kuo (1994), Jang (1997), Park (1999), Chen (2000) and Yang (2002).

4.5.1 Two-Dimensional Pore and Throat Analysis

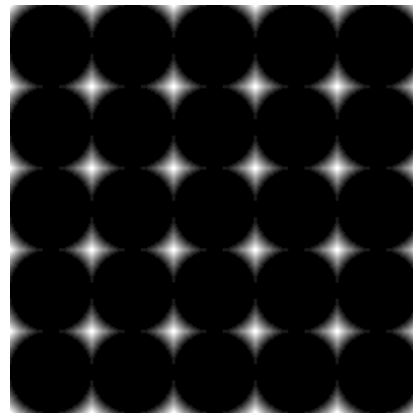
Two-dimensional calculations of pore and throat size measurement begin with identifying the skeleton of the pore space. The skeletonization process is implemented by using the public domain NIH Image program (developed at the U.S. National Institutes of

Health and available on the Internet at <http://rsb.info.nih.gov/nih-image/>). The skeleton was obtained by repeatedly removing pixels from the edges of objects in a binary image until they are reduced to single pixel wide skeletons. Objects are assumed to be black and the background is white. From the skeleton of the pore space, all of the nodes with three or more branches were chosen as the “center” of all the pores. Each branch connected to this node is identified as a throat. The Euclidean Distance Map (EDM) of the 2-D image, in which each pixel has the value of the distance from the node of the skeleton to the pore/particle boundary was obtained. (Each foreground (black) pixel in the binary image is replaced with a gray value equal to that pixel's distance from the nearest background (white) pixel.). This distance is defined as the pore radius. The minimum distance along each branch is the throat size. This calculation process was programmed using Matlab.

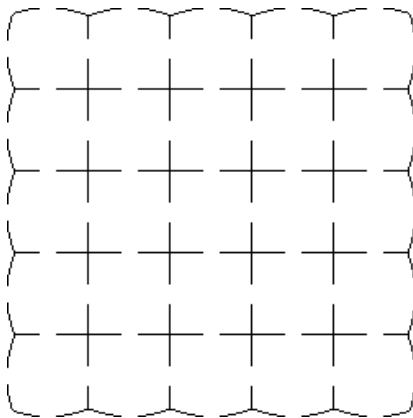
Visual illustration of the process is shown in Figure 4.25 (a-e). Figure 4.25(a) is the original 2-D image. A 2-D image used in reconstructing the SCP structure is used as an example. All the circles are of the same size. Figure 4.25 (b) is the Euclidean Distance Map of the 2-D image, in which each pixel value represents the corresponding distance in the original image from the point to the nearest grain boundary. Figure 4.25(c) is the skeleton of the image in Figure 4.25(a). Figure 4.25(d) shows all the pore centers identified. Figure 4.25(e) shows all the branches correspond to each pore center. From these branches and the EDM, the throat size can be calculated.



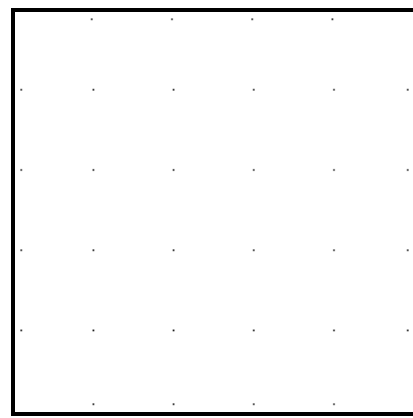
(a) 2-D Original Image of SCP



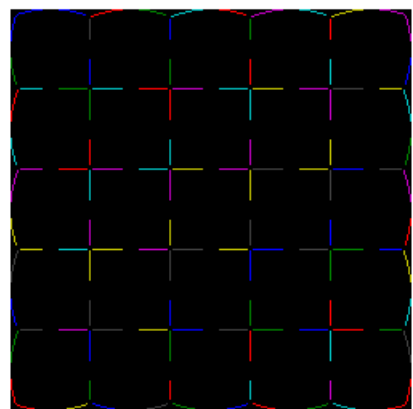
(b) EDM of the 2-D Image



(c) Skeleton of the Image



(d) Identified Pore Centers



(e) Branches (Throats) of Each Pore

Figure 4.25 Illustration of 2-D Pore and Throat Calculation

4.5.2 Local Void Ratio Distribution Analysis

An automated image processing and analysis procedure was developed and implemented by Kuo (1994) following the concept proposed by Oda (1976), which consists of dividing an image into polygons that connects centers of gravity of the soil particles (Figure 4.26). The local void ratio distribution can be obtained by calculating the void ratio of each polygon. Statistical analyses can be performed to model the distributions as a function of sample preparation method. Automating the process involved a series of morphological operations and a methodology to form the polygon network (Frost and Kuo, 1996).

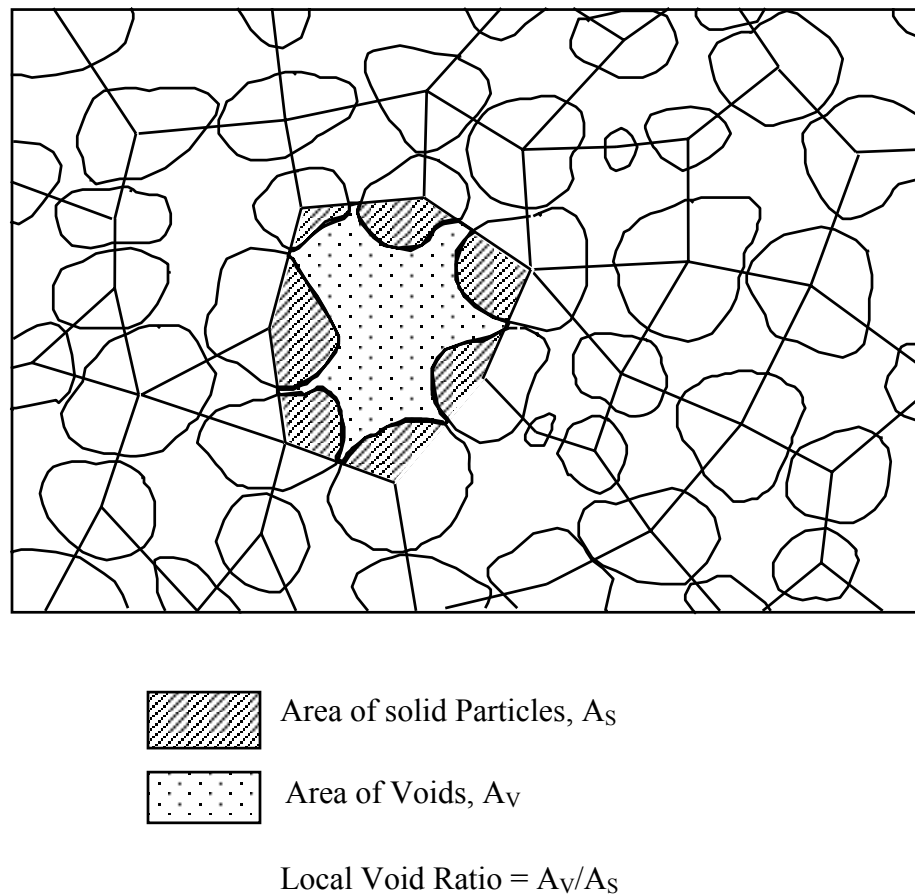


Figure 4.26 Determination of Local Void Ratio Distribution Using Oda's Method (After Jang, 1999)

4.5.3 2-D Pore Size and Throat Size Analysis of SCP and FCP

The 2-D pore size and throat size measurement results of SCP and FCP are shown in Figure 4.27 and 4.28 respectively. For the two structures with different porosity (SCP: 0.46; FCP: 0.26), it can be seen that SCP has more large pores than FCP. Most of the pores inside FCP are very small, with a diameter of about 10 pixels. However SCP has some very larger pores. This is because in the slices at some depth in SCP, only small size circles exist (Figure 4.29 (a)). This is not the case for FCP (Figure 4.29 (b)), where any slice will contain circles of multiple sizes. The large throats in SCP, result from the same condition. Both SCP and FCP 2-D pore size and throat size distributions display different structure information from the corresponding 3-D analysis. For example, in 3-D, SCP has pores of same size. However, in 2-D image, SCP has a range of pore size values. FCP has relatively less variation in 3-D in terms of pore size than that in 2-D. This is because of the fact that the structure is relatively uniform from a 3-D point of view, but in 2-D, the slices display different information at different depths in the volume.

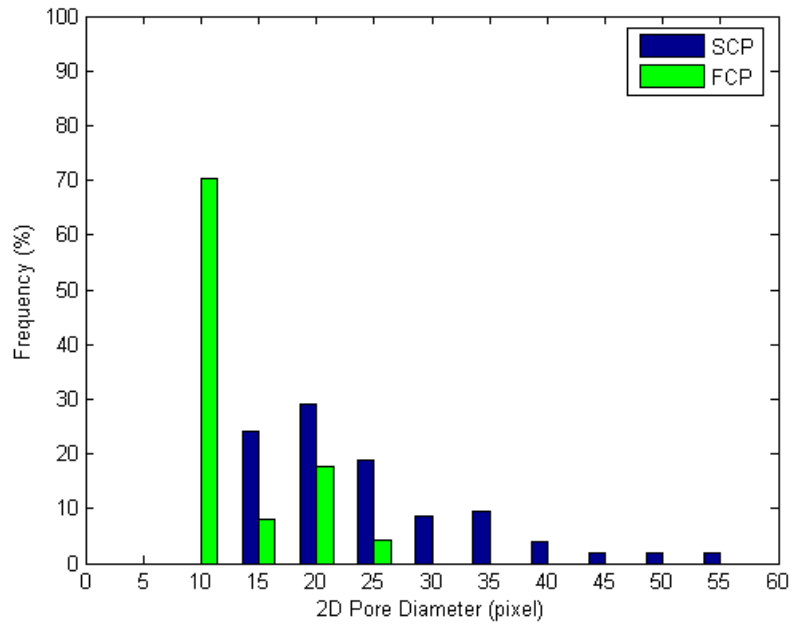


Figure 4.27 2-D Pore Size Distribution for SCP and FCP

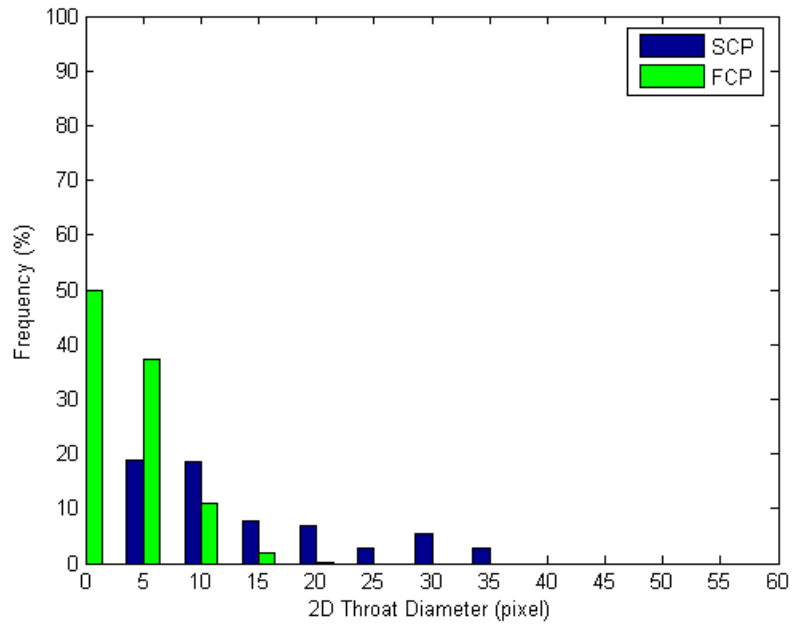
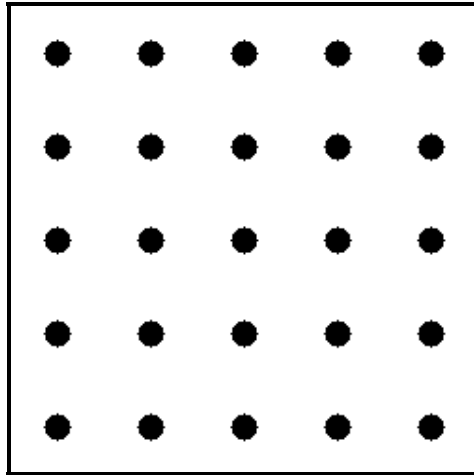
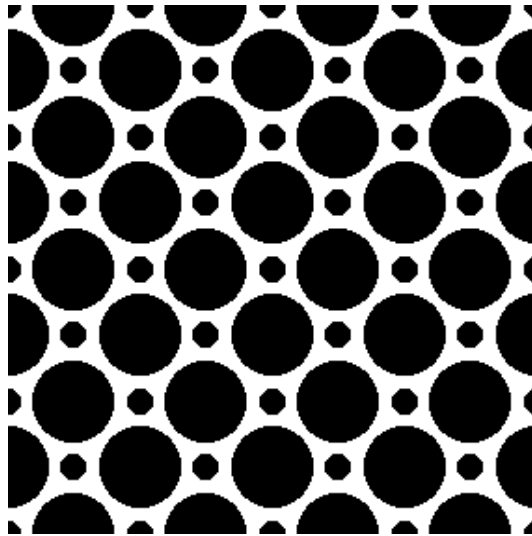


Figure 4.28 2-D Throat Size Distribution of SCP and FCP



(a)

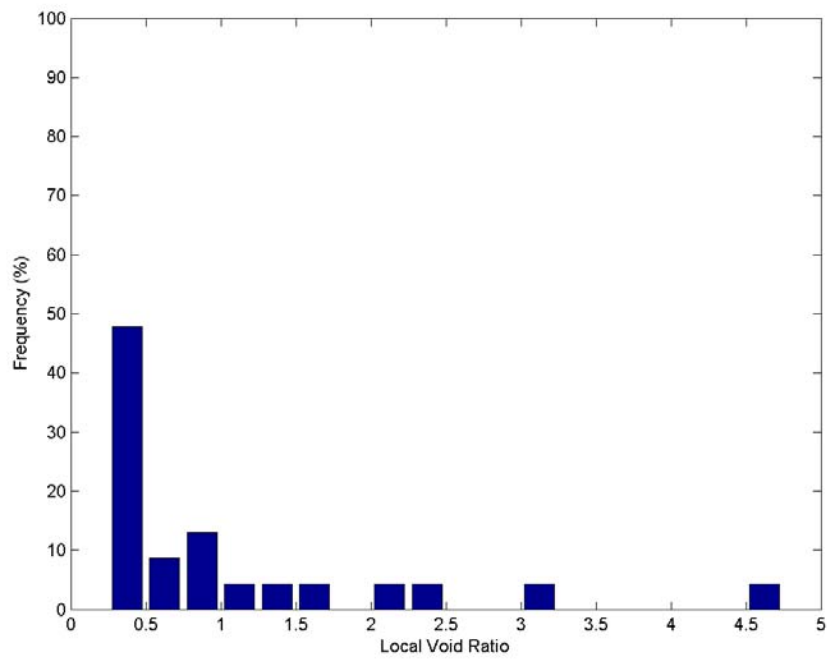


(b)

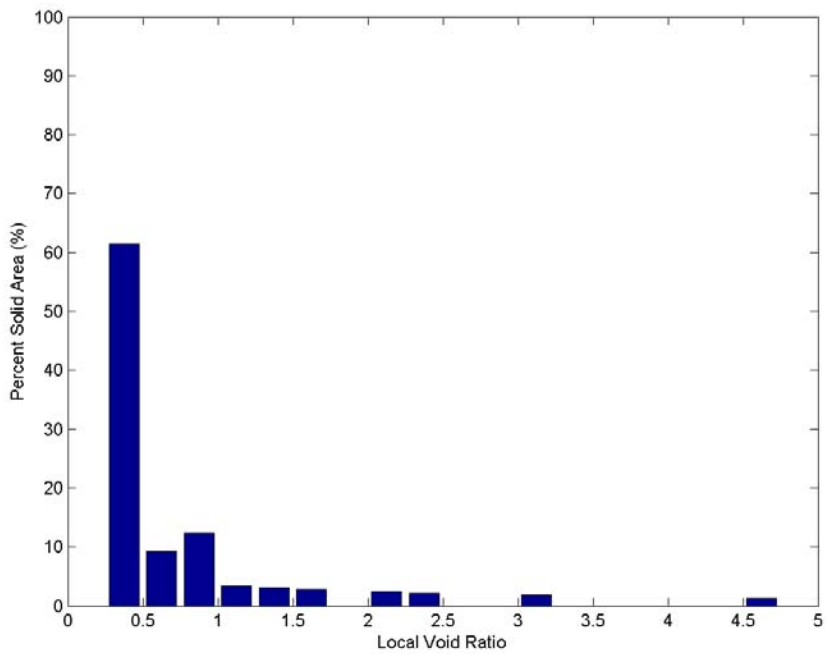
Figure 4.29 Example 2-D Slice Images of SCP and FCP (a) An Example 2-D Slice Image of SCP; (b) An Example 2-D Slice Image of FCP

4.5.4 Local Void Ratio Distribution of SCP and FCP

Local void ratios for all of the 2-D slices of the two simulated structures were measured. Local void ratio distribution and solid area weighted local void ratio (Frost and Kuo, 1996) distribution plots for SCP and FCP are shown in Figures 4.30 and 4.31 respectively.

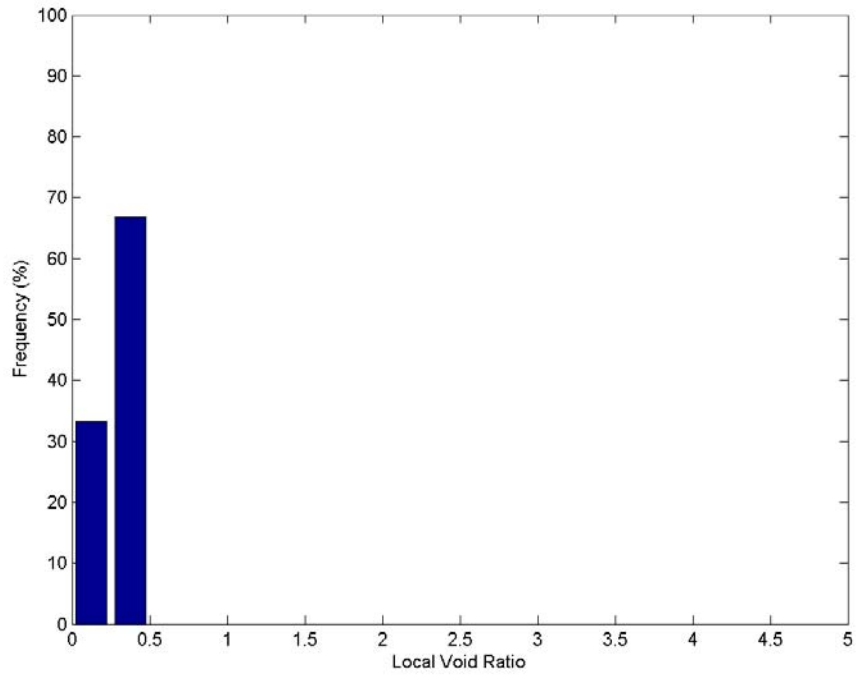


(a)

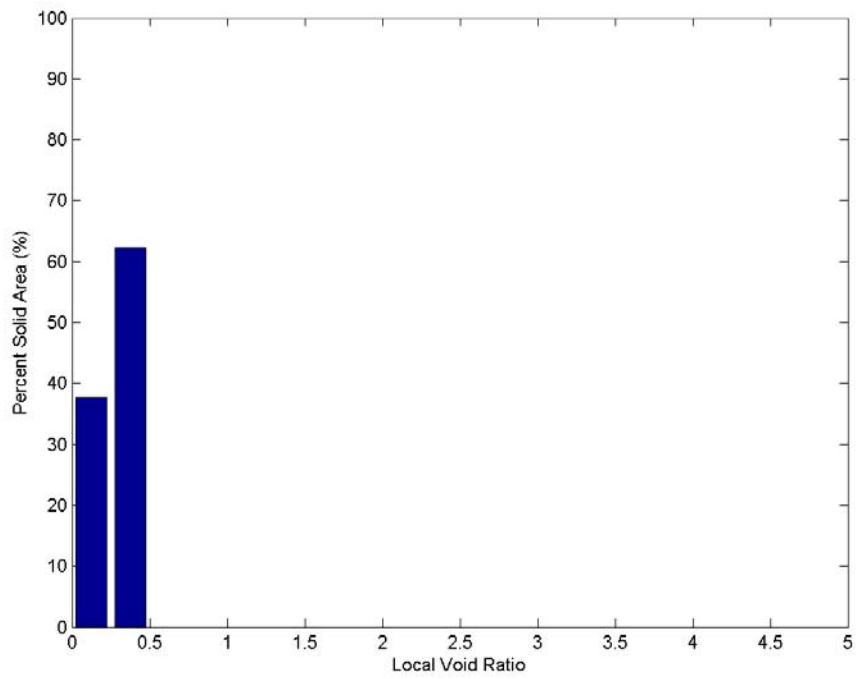


(b)

Figure 4.30 Local Void Ratio Distribution of SCP (a) Local Void Ratio Distribution of SCP; (b) Solid Area Weighted Local Void Ratio Distribution of SCP



(a)



(b)

Figure 4.31 Local Void Ratio Distribution of FCP (a) Local Void Ratio Distribution of FCP; (b) Solid Area Weighted Local Void Ratio Distribution of FCP

It is clearly shown in the four graphs that local void ratio distribution exhibits similar patterns as the 2-D pore size distribution. SCP has more large local void ratios than FCP. Large pore size corresponds to large local void ratio. All of the local void ratios of FCP are less than 1, which reflects less variation in 2-D FCP images.

4.6 3-D Particle Size Analysis

4.6.1 Introduction

3DMA is designed to quantify the pore structure of any bi-phase material. If the information provided to the program represents the particles as pores and vice versa, it is possible to measure the particle size distribution instead of the pore size distribution with 3DMA. In this research, SCP is used to validate the program's ability to quantify the particle size in a bi-phase material.

4.6.2 3-D Grain Size of SCP

The same SCP (5 x 5 x 5) structure used in pore size distribution (Figure 4.3) is used in particle size analysis (Table 4.8). The medial axis of the particle space is shown in Figure 4.32. They connect the centers of the neighboring spheres. A unit of the particle unit in SCP structure is shown in Figure 4.33. Red represents the boundary (throat) of the individual particle. The purple shows the pore space around the particle. Figure 4.34 is shows a single particle, which is a sphere in the original SCP structure.

Table 4.8 SCP Particle Size Measurement Results

		Volume (voxels)
Individual Interior particles	27 internal particles (3 x 3 x3)	67,312
		67,312
		67,312
		...
		67,312
		67,312
		67,312
		67,312
	Total→	1,817,424
Particles that touch the edge	98 external particles	67,134
		67,184
		...
		67,490
	Total→	6,596,576
Total Particle Volume		8,414,000
Density		0.534

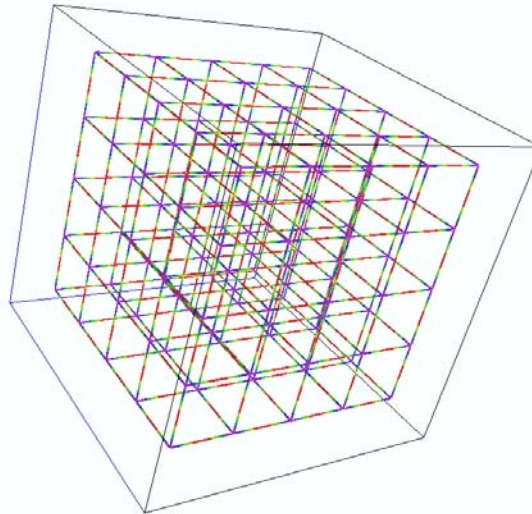


Figure 4.32 Medial Axis of the Particle Space in SCP

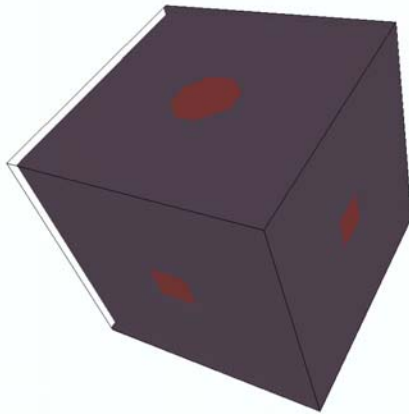


Figure 4.33 A Unit of SCP (red: throats of a particle; purple: surrounded pore space)

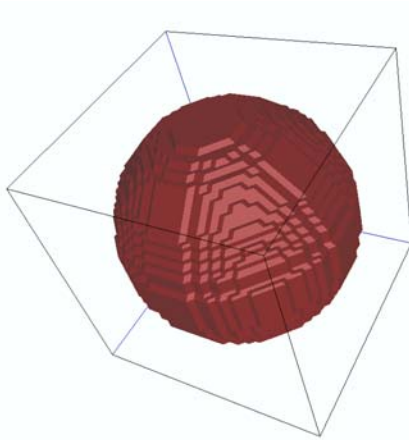


Figure 4.34 Individual Particle Visualization

The results from 3DMA are shown in Table 4.9. The total number of particles found by 3DMA is 125, which is the same as the total spheres used in the SCP structure. There are 27 internal particles in the volume with size of 67132 voxels, which means an equivalent radius of 25.2 pixel. The theoretical size of each particle (sphere) is 65450 voxels, which is about 2.9% different from the calculated value. The error in the measured radius is 0.94%.

Table 4.9 Comparison between Theoretical Values and 3DMA Measurement Results on Particle Size

		Theoretical Values	3DMA Values	Error (%)
Total Particle Size (voxels)		8,181,231	84,14,000	2.9
Each Unit Size (voxels)	50^3	125,000	N/A	N/A
Each Particle Size (voxels)	Unit Size *Density	65,450	67,312	2.9
Sphere Radius (pixel)		25	25.2	0.94

The particle size distribution of the SCP structure is shown in Figure 4.35. All of the particle sizes are between 67314 and 67490 voxels. The difference between the minimum particle size and the maximum particle size is about 0.53%. As indicated above, all of the internal particles have the same particle size.

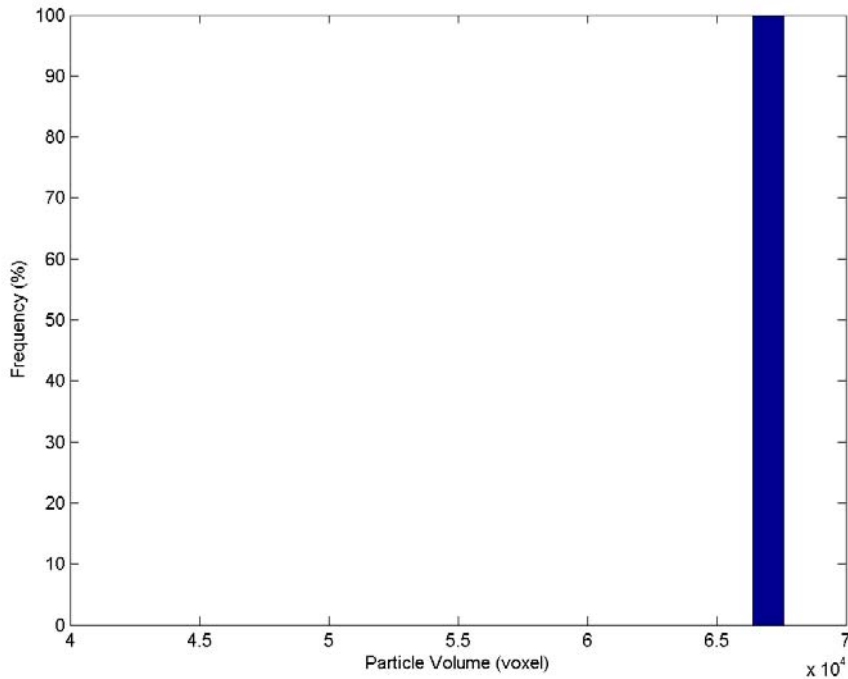


Figure 4.35 Particle Size Distribution of SCP

The particle size in the 3-D space can be visualized as shown in Figure 4.36. The size of each particle is represented by the radius of the sphere at the corresponding

position in the structure. Note that these sphere are not touching because they are not intended to represent individual particles, but the relative size of particles. In this case, all spheres are the same size because the particles are all the same size. The colors differentiate the levels of each sphere (red: high; blue: low) within the volume.

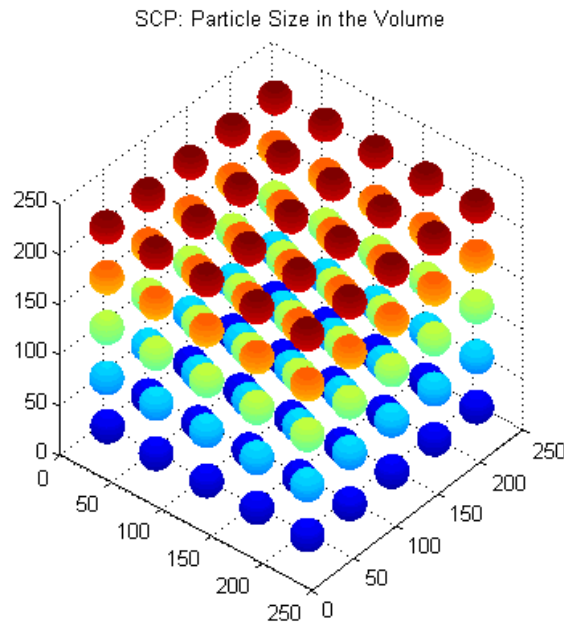


Figure 4.36 Visualization of Particle Size in SCP

From this chapter's analysis, it can be concluded that 3DMA can provide reasonable results during the characterization of a 3-D bi-phase structure. As previously noted 2-D image analysis sometimes can not present similar information as 3-D analysis. The condition is likely to be exacerbated when considering idealized structures with regular packings. In the next chapter, both 2-D and 3-D analyses will be applied to the four specimens (AP0, AP14, MT0, and MT14) to study the preparation-induced variation and shearing-induced evolution of the specimen microstructure.

CHAPTER V

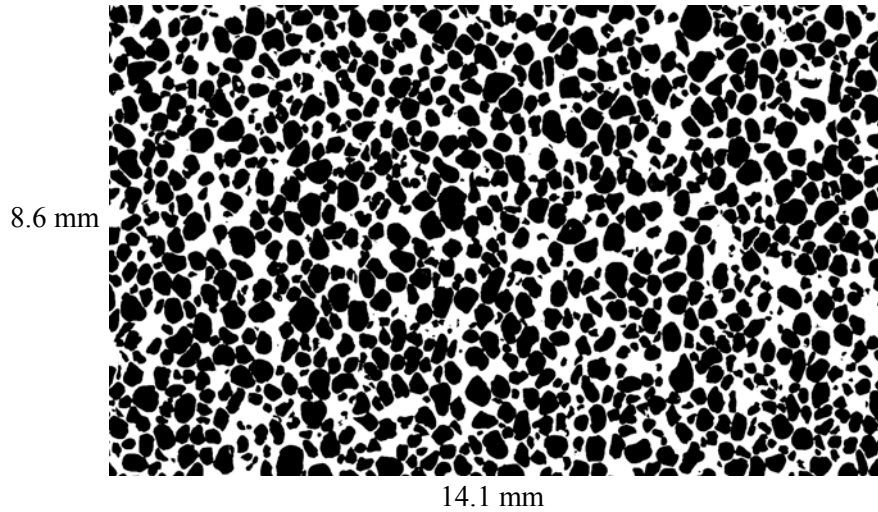
2-D CHARACTERIZATION OF SPECIMEN MICROSTRUCTURE

5.1 Introduction

To study preparation-induced variation and shearing-induced evolution of the structure of triaxial sand specimens, air-pluviated and moist-tamped specimens were subjected to axial compression loading until a predetermined global axial strain was achieved. The influence of specimen preparation method on soil structure variation was investigated in this study by comparing two specimens prepared by air-pluviation and moist-tamping (AP0 and MT0). Comparisons between the structures of un-sheared and sheared specimens (AP0 and AP14; MT0 and MT14) were also made to examine the shearing-induced evolution in the structure. The comparisons focused on microstructure variation and evolution from the perspective of void structure. In this chapter, the microstructure studies used the 2-D images from the four specimens obtained following the epoxy impregnation and serial grinding described in Chapter 3. Four samples were characterized in two-dimensions in terms of void ratio, pore size and throat size. Complimentary three-dimensional analysis is presented in Chapter 6. It is noted that this study focused on dense specimens ($D_R=75\%$) only.

The void ratio of a 2-D image was calculated by dividing the total area of voids by the total area of sand particles in an image as illustrated in Figure 5.1. The 2-D mean void ratio is the average void ratio from 600 slices for each sample. The 2-D mean void

ratios for AP0, AP14, MT0 and MT14 are 0.575, 0.715, 0.575 and 0.704 respectively. The global measurements of void ratio during preparation of specimens AP0 and MT0 are 0.582 and 0.580, respectively.



Area: 1800 x 1100 square pixels

 Sand Particle

 Void (Epoxy)

Void Ratio of the Image = Total Area of Voids/Total Area of Sand Particles

Figure 5.1 Void Ratio of an ASTM Graded Sand Image

5.2 Local Void Ratio

5.2.1 Introduction

The solid area weighted local void ratios of the 2-D slices were calculated for the four specimens (AP0, AP14, MT0 and MT14) by following the procedure described in Chapter 4. The results were also compared with the measurement results for air-pluviated and moist-tamped specimens from previous studies by Jang (1997) and Park (1999).

5.2.2 Local Void Ratio Measurement

In this research, for each specimen, the local void ratio distribution was calculated based on 60 selected slices. These slices correspond to vertical surfaces in the original triaxial specimens. The results of local void ratio distribution of the four specimens were compared with the data for the air pluviated specimens and moist tamped specimens of Jang (1997) and Park (1999) at the same global strain level (Figure 5.2 – Figure 5.9). It can be observed from the plots that specimen j30 ($\epsilon=14\%$) has a larger mean value than specimen j18 ($\epsilon=0\%$). Similarly the mean local void ratio of m18 ($\epsilon=14\%$) is higher than that of m11 ($\epsilon=0\%$). Both these pairs of specimens from the Jang (1997) and Park (1999) studies reflect the dilation that occurred during shearing. The same behavior is seen in specimens AP0/AP14 and MT0/MT14 from the present study.

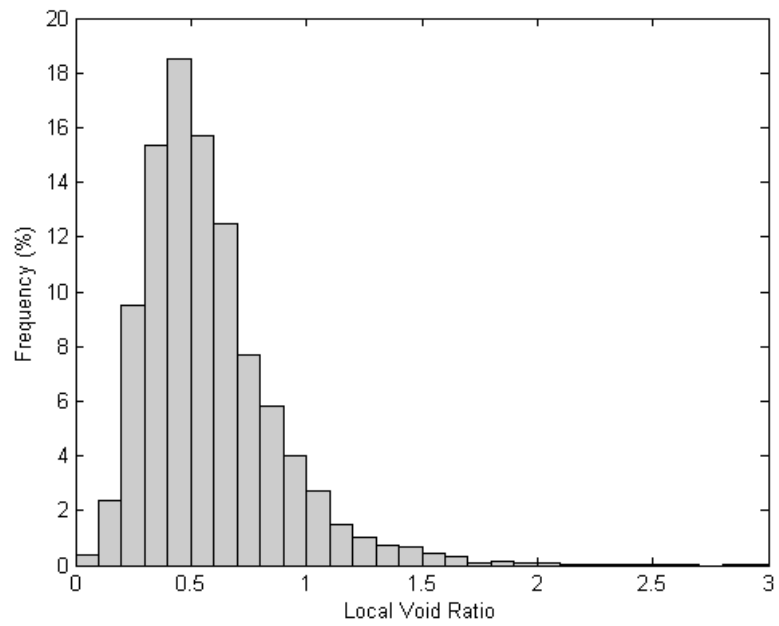


Figure 5.2 Local Void Ratio Distribution of AP0

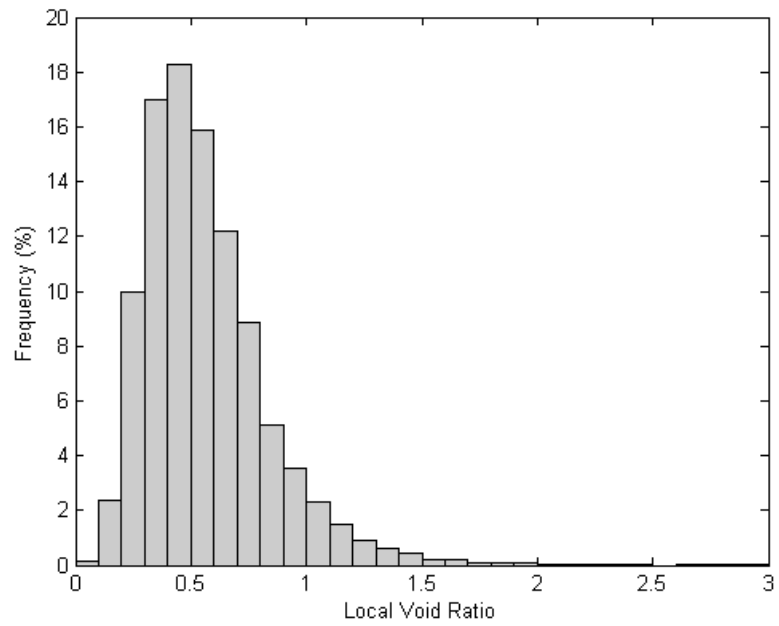


Figure 5.3 Local Void Ratio Distribution of j18 (Air-pluviated, unsheared) (Jang, 1997)

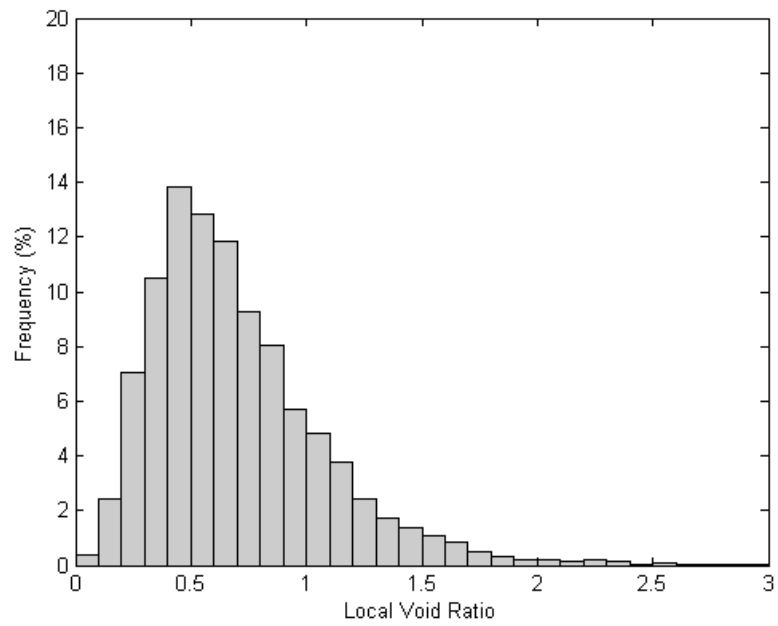


Figure 5.4 Local Void Ratio Distribution of AP14

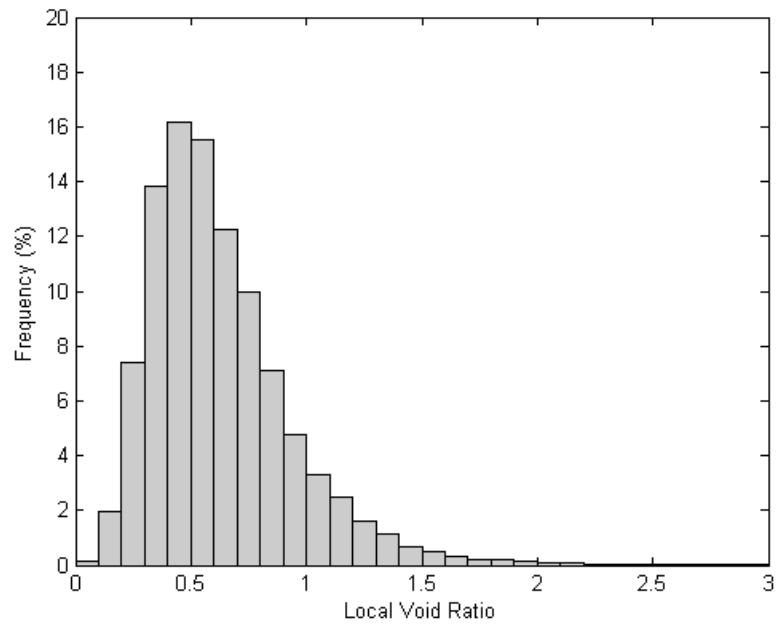


Figure 5.5 Local Void Ratio Distribution of j30 (Air-pluviated, sheared) (Jang, 1997)

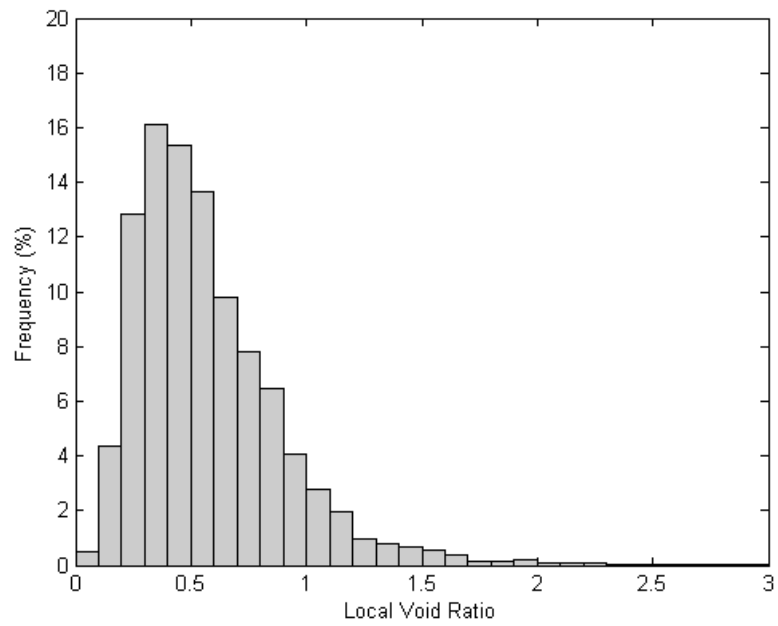


Figure 5.6 Local Void Ratio Distribution of MT0

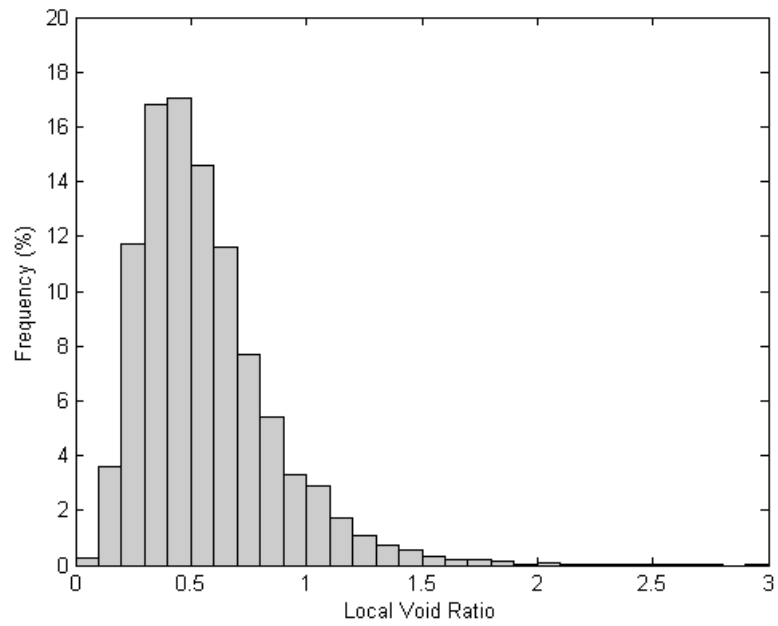


Figure 5.7 Local Void Ratio Distribution of m11 (Moist-tamped, unsheared) (Park, 1999)

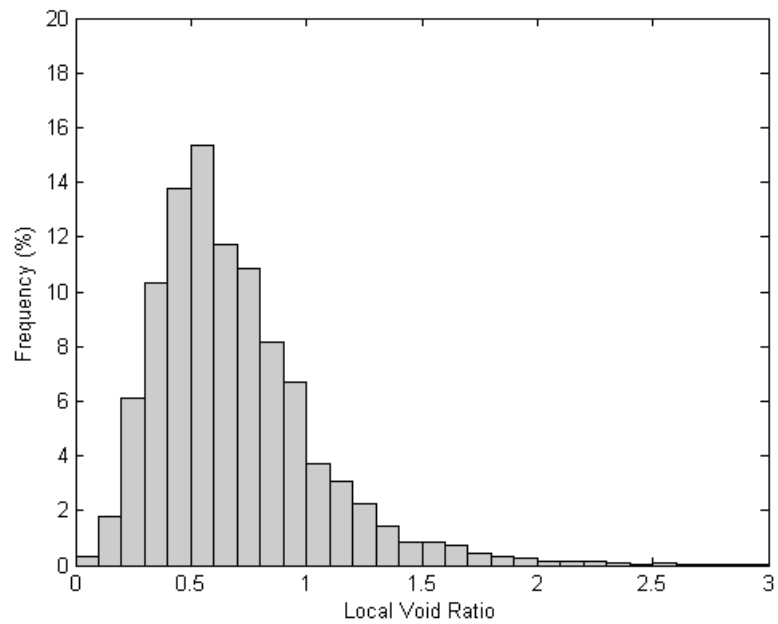


Figure 5.8 Local Void Ratio Distribution of MT14

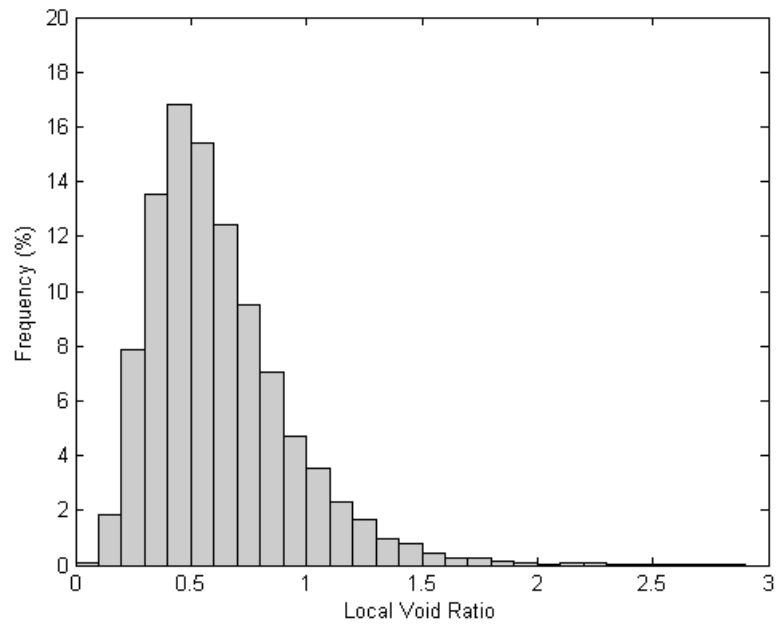


Figure 5.9 Local Void Ratio Distribution of m18 (Moist-tamped, Sheared) (Park, 1999)

To further study the relationship between the local void ratio and the standard deviation, estimated solid area weighted mean local void ratio, and standard deviation

were calculated for each specimen. The results are plotted in Figure 5.10 and Figure 5.11. It is shown in Figure 5.10 that local void ratio distribution of MT0 has a higher standard deviation than AP0 at the same mean local void ratio. The air pluviation line and the moist tamping trend lines derived by Jang (1997) and Park (1999) for as-consolidated specimens are also plotted in the same graph. It can be observed that AP0 and MT0 agree well with the previous data. Similarly, AP14 and MT14 are plotted in Figure 5.11 along with the air pluviation and moist tamping trend lines from the previous studies (Jang, 1997; Park, 1999) for as-sheared specimens. It can be seen that the standard deviations of the local void ratio of specimens AP14 and MT14 are slightly higher than the predicted trend line values but are at a comparable distance from the trend lines as the Jang (1997) and Park (1999) individual data points were.

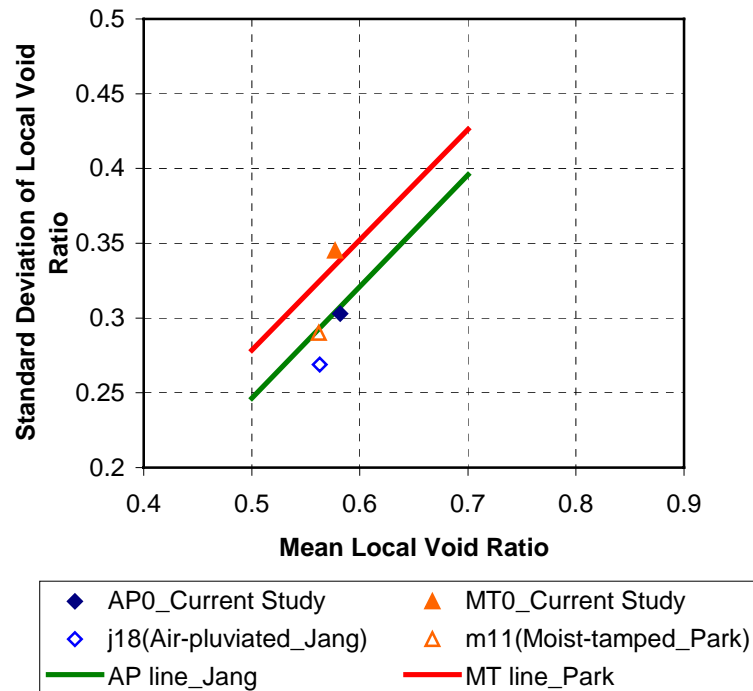


Figure 5.10 Mean Local Void Ratio vs. Standard Deviation of Local Void Ratio of Air-Pluviated and Moist-Tamped Specimens

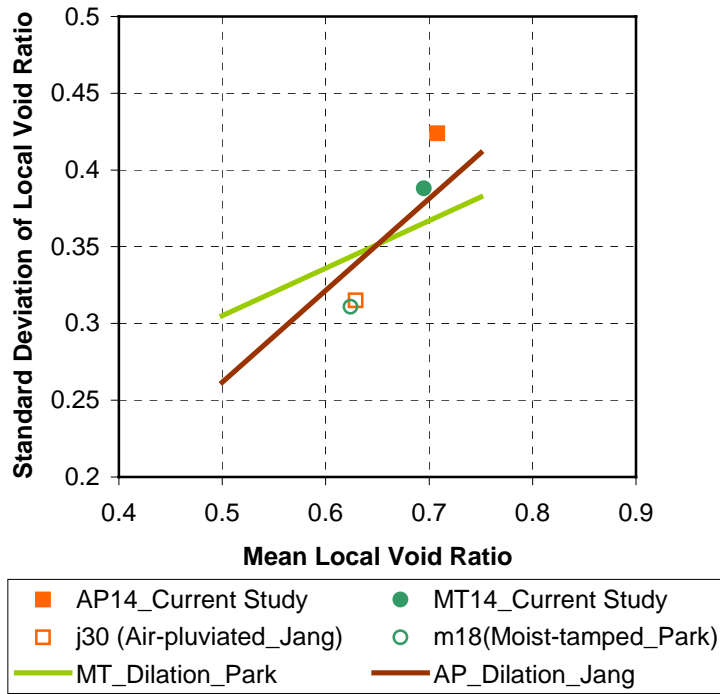


Figure 5.11 Mean Local Void Ratio vs. Standard Deviation of Local Void Ratio of Air-Pluviated and Moist-Tamped Specimens During Axial Compression Test

5.2.3 Statistical Analysis

The concept of entropy can also be employed in the analysis of local void ratio distribution. The parameter, local void ratio entropy, was defined by Park (1999) as:

$$H = -\sum_{i=1}^N p_i \ln p_i \quad (5.1)$$

where p_i is the frequency of a void ratio interval in histogram

N is the number of void ratio interval

The entropy for each sample was plotted in Figure 5.12 and compared with previous data. It is found that local void ratio distribution entropy of as-sheared specimen is higher than as-consolidated specimen. The lines derived from previous studies (Jang, 1997; Park, 1999) are for as-consolidated specimens. The difference between the data

may be attributed to the difference sizes of images and the resulting differences in number of polygons.

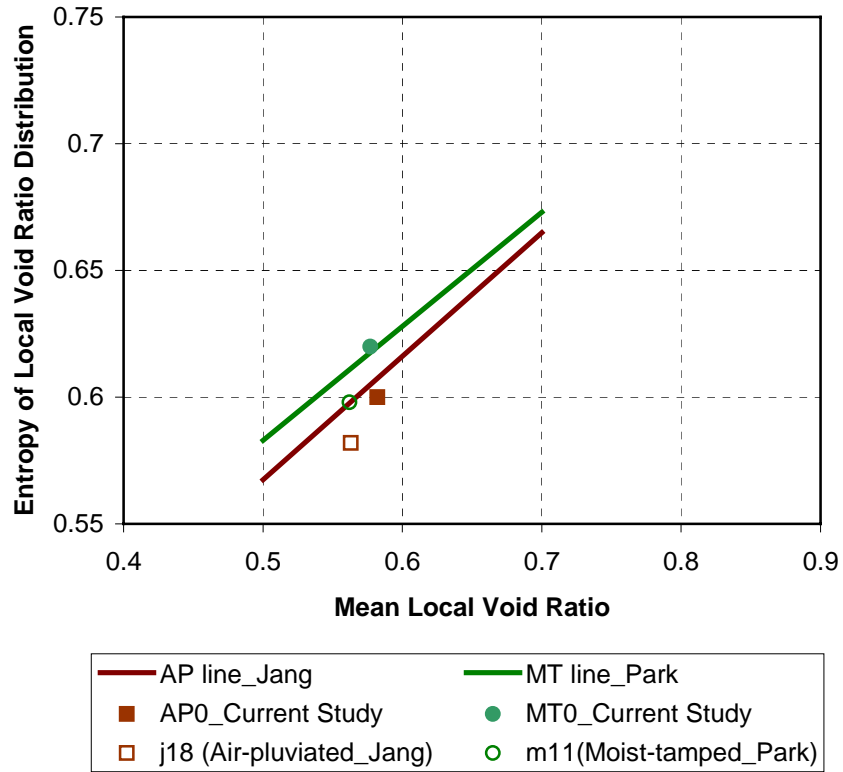


Figure 5.12 Relationship between Mean Local Void Ratio and Entropy

Statistical modeling of a probability distribution was performed on the local void ratio distributions to identify the distribution type most appropriate for the ASTM graded sand specimens.

To explore possible statistical models (hypotheses), Pearson’s probability distributions space was used (Figure 5.13). Regions of several standard probability distributions are shown in the plane of β_1 and β_2 where

$$\sqrt{\beta_1} = \frac{E(X - \mu)^3}{(\sigma^2)^{3/2}} \tag{5.2}$$

is the skewness and

$$\beta_2 = \frac{E(X - \mu)^4}{\sigma^4} \quad (5.3)$$

is the kurtosis of the distribution. The function $E()$ is the expected value, while X is the variable of the distribution, μ is the mean and σ is the standard deviation of the distribution. When the β_1 and β_2 values of the pore sizes for the four samples were plotted against Pearson's space (Figure 5.13), it was found that gamma and lognormal distributions may be used to model local void ratio distribution.

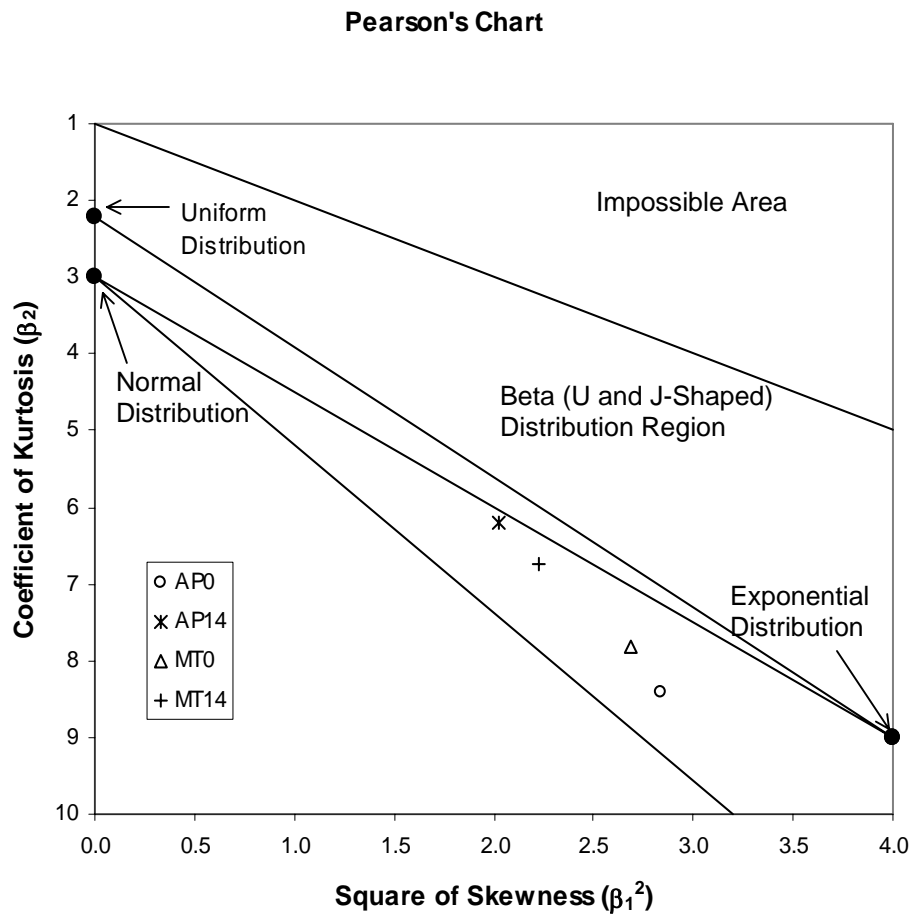


Figure 5.13 Evaluation of Local Void Ratio Distribution Models Using Space of Pearson's Probability Distributions (after Pearson and Hartley, 1972)

For a further analysis, the local void ratio distributions were tested for the hypotheses of the two continuous probability distributions: lognormal, and gamma distributions. These two distributions all have a positive variable ($x > 0$).

The gamma probability distribution function is expressed as

$$f(x) = \frac{\lambda}{\Gamma(k)} \cdot (\lambda \cdot x)^{k-1} \cdot \exp(-\lambda \cdot x) \quad x > 0 \quad (5.4)$$

$$f(x) = 0 \quad x \leq 0 \quad (5.5)$$

$$\text{where: } \Gamma(k) = \int_0^{\infty} x^{k-1} \cdot \exp(-x) \cdot dx \quad \text{for } k > 0 \quad (5.6)$$

is the gamma function. For this application, the variable x is the pore size in the distribution. The parameter k is usually called the shape parameter, and λ is called the scale parameter. These two parameters can be obtained by the following equations

$$E(x) = \frac{k}{\lambda} = \mu \quad \text{the estimated mean of a distribution, and} \quad (5.7)$$

$$V(x) = \frac{k}{\lambda^2} = \sigma^2 \quad \text{the estimated variation of the distribution} \quad (5.8)$$

Only two parameters, the mean and the standard deviation, of a distribution are needed to obtain the gamma probability function to model the distribution.

The lognormal distribution is related to the normal distribution. If x has normal distribution and $x = \ln y$, then y is said to have a lognormal distribution. The formula of a lognormal distribution function is:

$$f(x) = \frac{1}{\sigma_y \cdot x \sqrt{2\pi}} e^{-\left[\frac{1}{2\sigma_y^2} (\ln x - \mu_y)^2 \right]} \quad (5.9)$$

The variable x in Eq. (5.10) is local void ratios in this study. The expected mean value (μ) and the standard deviation (σ) from lognormal distribution are:

$$\begin{aligned}\mu &= \exp\left[\mu_y + \frac{1}{2}\sigma_y^2\right] \\ \sigma^2 &= (e^{\sigma_y^2} - 1) \cdot \exp\left[\mu_y + \frac{1}{2}\sigma_y^2\right]\end{aligned}\tag{5.10}$$

So, two parameters (μ_y and σ_y) are needed to define the lognormal distribution.

To objectively test the goodness of fit of the hypotheses, the Kolmogoroff-Smirnov test was used in this study. The Kolmogoroff-Smirnov test is a distribution-free test that can be applied to a large class of models. It is based on the comparison of the cumulative distribution functions of the empirical distribution $\hat{F}_A(x)$ and the hypothesis distribution $\hat{F}_B(x)$. The test of fit is measured by the maximum absolute difference between $\hat{F}_A(x)$ and $\hat{F}_B(x)$

$$M = \max_x |\hat{F}_A(x) - \hat{F}_B(x)|\tag{5.11}$$

The value M is the maximum vertical distance between the cumulative curves of $\hat{F}_A(x)$ and $\hat{F}_B(x)$ when they are plotted together on a graph. It can be concluded based on the M values (Table 5.1) calculated for the four samples that, lognormal distribution is the most plausible distribution for local void ratio distributions of the four samples in this study.

Table 5.1 Gamma and Lognormal Distribution Parameters of Local Void Ratio Distributions of the Four Samples

Sample	Gamma			Lognormal		
	κ	λ	M	μ_v	σ_v	M
AP0	4.365	0.130	0.064	-0.682	0.497	0.033
AP14	3.624	0.196	0.049	-0.489	0.560	0.024
MT0	3.625	0.158	0.056	-0.706	0.561	0.027
MT14	4.170	0.168	0.056	-0.482	0.519	0.029

5.3 2-D Pore Size Distributions

5.3.1 Introduction

As described in Chapter 4, 2-D pore size can be calculated from the skeleton of the pore space and the Euclidean Distance Map of the 2-D image. From the skeleton of the pore space, all of the nodes with three or more branches were chosen as the “center” of all the pores. In this section, 2-D pore size analysis was applied on the four samples AP0, AP14, MT0 and MT14 to study the specimen preparation method effects and shearing-induced structure evolution.

5.3.2 Pore Size Measurement

The 2-D pore size (pore diameter) distributions of AP0 and MT0 are plotted in Figure 5.14. From the plot, it can be observed that MT0 has more small pores, which is indicative of more variations inside moist tamped specimens. These variations are consistent with the layering that results from use of the preparation method (Frost and Park, 2003). Even though the difference between the frequency distributions for specimens prepared using air pluviation and moist tamping methods in Figure 5.14 may not seem to be significant, it is noted that it is almost the same magnitude (or even higher

in some ranges) as the difference observed in Figure 5.15 for air-pluviated specimens at different global strain levels (0% and 14%) and thus different global void ratios (0.575 and 0.715). Similar comparison between the local void ratio distributions for air pluviation and moist tamping specimens were discussed by Frost and Jang (2000). Data for specimens AP0 and AP14, and MT0 and MT14 were plotted in Figure 5.15 and Figure 5.16 respectively for comparison. It is observed that the distribution for both AP14 and MT14 are shifted to the right in the distribution graph, which means AP14 and MT14 have more large pores than AP0 and MT0. In other words, the pore size distribution plots are consistent with specimens that have dilated. It can be seen however that the amount of change in AP14 is significantly greater than for MT14. This is consistent with the fact that dilation in AP14 is more global in nature whereas in MT14 it is more limited to the shear band that formed and this effect is not isolated in the measurements presented in Figure 5.16.

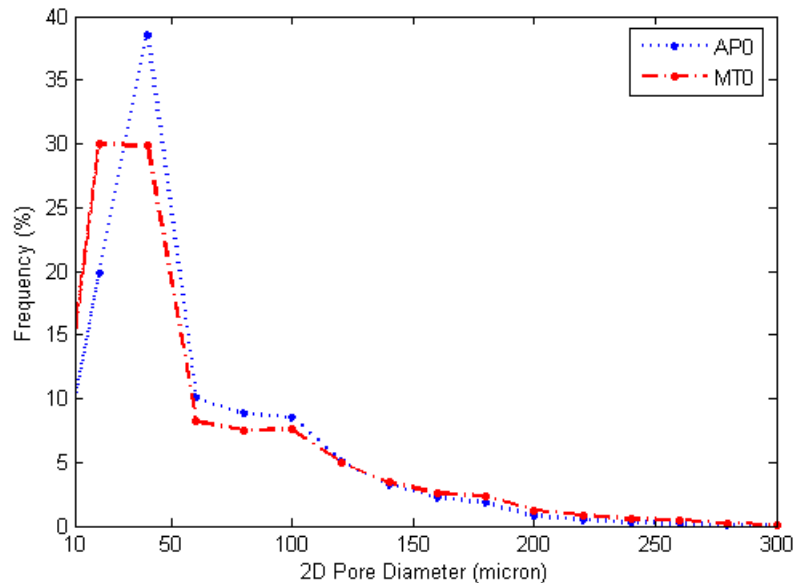


Figure 5.14 2-D Pore Diameter Distribution of AP0 and MT0

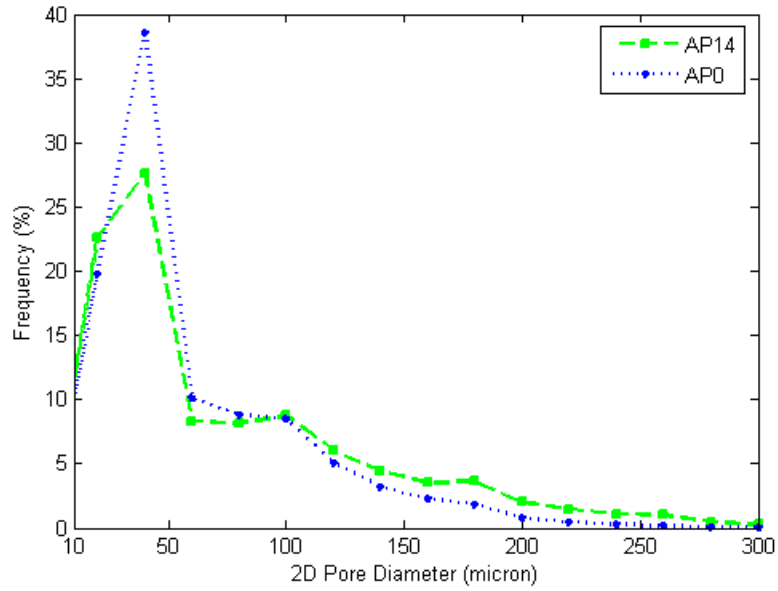


Figure 5.15 Comparison of 2-D Pore Diameter Distribution of AP0 and AP14

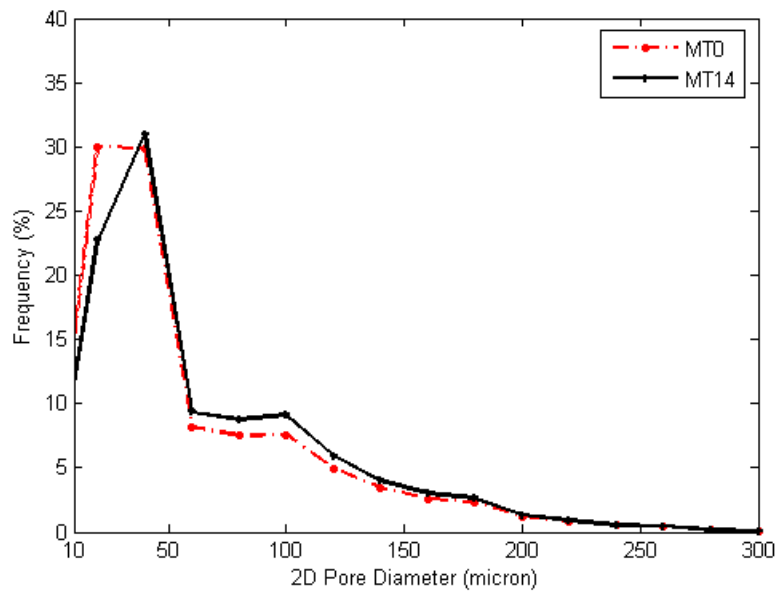


Figure 5.16 Comparison of 2-D Pore Diameter Distribution of MT0 and MT14

The mean, standard deviation and coefficient of variation of the pore size for each sample were calculated and listed in Table 5.2 and plotted in Figure 5.17. The mean pore

size of AP0 is slightly larger than MT0. The coefficient of variation of the moist-tamped specimen is 0.530, which is larger than the 0.427 of the air pluviated specimen. It can be concluded that the air-pluviated specimen is more uniform than moist tamped specimen. This conclusion is consistent with the findings of previous studies (Jang, 1997; Park, 1999) on the microstructure of the specimens based on local void ratio distribution. Sample MT14 has a higher mean pore size and lower coefficient of variation than sample AP14. This is consistent with the fact that air pluviated specimen AP14 shows global dilation, which means an increased mean and standard deviation. However, moist tamped specimen MT14 shows localized dilation in the shear band, which resulted in less change in mean and standard deviation globally. Both the pore sizes of AP14 and MT14 are greater than the corresponding specimens prepared with the same method (AP0 and MT0, respectively).

Table 5.2 2-D Pore Diameter (micron)

Sample	μ	σ	CV (%)	H _v
AP0	111.969	47.7787	42.7	0.614
AP14	139.061	66.1165	47.6	0.772
MT0	109.448	58.0046	53.0	0.714
MT14	120.676	56.2977	46.7	0.719

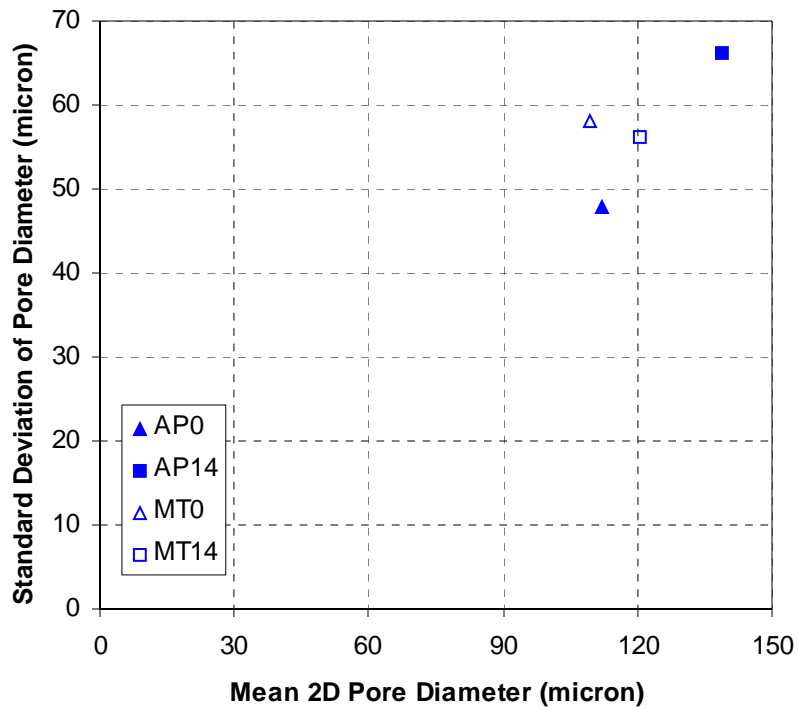


Figure 5.17 Mean Pore Size vs. Standard Deviation of 2-D Pore Diameter

5.3.3 Statistical Modeling of Pore Size Distribution

The same statistical analysis as discussed in Section 5.2 was applied to pore size results also. An example of pore size distribution and fitted lognormal distribution is shown in Figure 5.18. Pore diameter distributions of the four samples in Pearson's space are shown in Figure 5.19. It can be seen that beta, lognormal and gamma distribution may be the plausible models for pore size distribution.

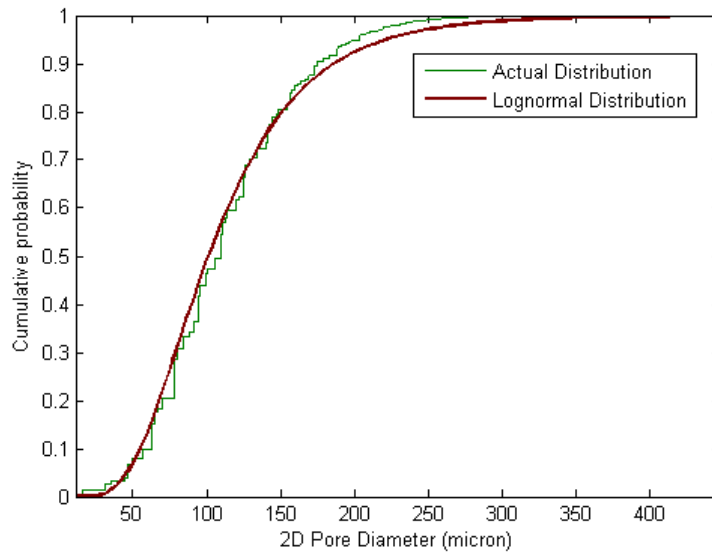


Figure 5.18 Cumulative Probability of the Actual Distribution of 2-D Pore Diameter of AP0 and the Fitted Lognormal Distribution

Pearson's Chart

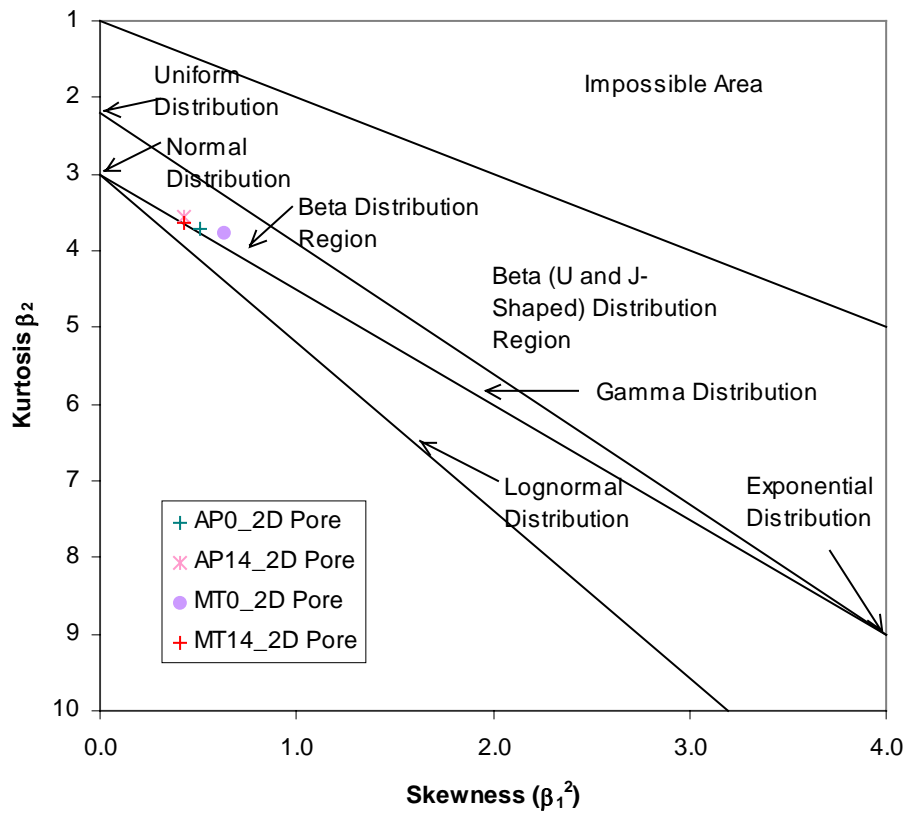


Figure 5.19 Evaluation of Pore Diameter Distribution Models Using Space of Pearson's Probability Distributions (after Pearson and Hartley, 1972)

The beta probability distribution is defined over the range [a, b] by

$$f(x) = C(x - a)^\alpha (b - x)^\beta \quad (5.12)$$

where $\alpha > -1$ and $\beta > -1$, and the normalizing constant C is

$$C = \frac{(\alpha + \beta + 1)!}{\alpha! \beta! (b - a)^{\alpha + \beta + 1}} \quad (5.13)$$

if α and β are integers.

The expected value and the variation of the beta distribution are

$$E[beta] = a + \frac{\alpha + 1}{\alpha + \beta + 2} (b - a) \quad (5.14)$$

$$V[beta] = \frac{(b - a)^2 (\alpha + 1)(\beta + 1)}{(\alpha + \beta + 2)^2 (\alpha + \beta + 3)} \quad (5.15)$$

The parameters α and β can be obtained from the expected value $E[x] = \bar{x}$ and standard deviation $\sigma = \sigma[x]$ of the variables from

$$\alpha = \frac{X^2}{Y^2} (1 - X) - (1 + X) \quad (5.16)$$

$$\beta = \frac{\alpha + 1}{X} - (\alpha + 2) \quad (5.17)$$

where $X = (\bar{x} - a)/(b - a)$ and $Y = \sigma/(b - a)$.

To objectively test the goodness of fit of the hypotheses, the Kolmogoroff-Smirnov test was also used and the maximum difference between the observed cumulative density and the estimated cumulative density from the model was calculated for each sample. The parameters for each model are shown in Table 5.3. Based on the results of the test, it was found that lognormal distribution with consistently lower M values, is the most plausible model for 2-D pore size distribution.

Table 5.3 2-D Pore Diameter Statistical Parameters

Sample	Beta			Gamma			Lognormal		
	α	β	M	κ	λ	M	μ_y	σ_y	M
AP0	2.289	9.402	0.088	6.319	18.056	0.072	4.656	0.430	0.052
AP14	2.206	8.501	0.057	5.212	27.431	0.045	4.864	0.481	0.034
MT0	1.808	8.402	0.096	4.732	24.482	0.077	4.643	0.499	0.052
MT14	2.376	17.769	0.076	5.541	22.500	0.060	4.733	0.463	0.042

5.4 Throat Size Distributions

5.4.1 Introduction

2-D throat size of the pore space is measured based on the skeleton and the branch analysis on the 2-D slices. From the skeleton of the pore space, all of the nodes with three or more branches were chosen as the “center” of all the pores. Each branch connected to this node is identified as a throat. The Euclidean Distance Map (EDM) of the 2-D image was obtained, in which each pixel has the value of the distance from the node of the skeleton to the pore/particle boundary. Each foreground (black) pixel in the binary image is replaced with a gray value equal to that pixel's distance from the nearest background (white) pixel. This distance is defined as the pore radius. The minimum distance along each branch is the throat size (throat radius). The statistical parameters such as mean, standard deviation, and coefficient of variation are calculated for each sample and compared.

5.4.2 2-D Throat Size Measurement

2-D throat size distributions of the four samples are shown in Figure 5.20, Figure 5.21 and Figure 5.22. It can be observed from Figure 5.21 and Figure 5.22 that the dilated

specimens have more large throats. AP0 and MT0 (Figure 5.20) throat diameters display differences in the distribution of throat sizes between 50 and 100 micron. Furthermore, the smallest throats in MT0 are the most frequent.

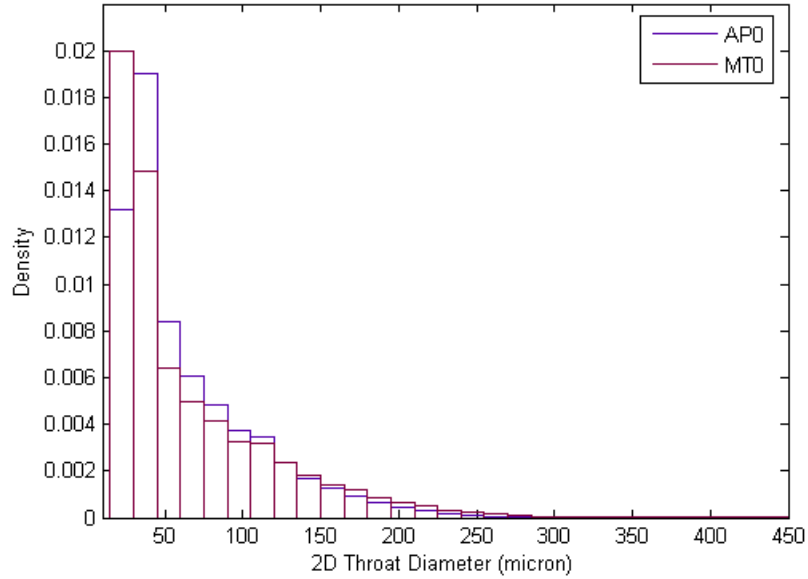


Figure 5.20 2-D Throat Diameter Distributions of AP0 and MT0

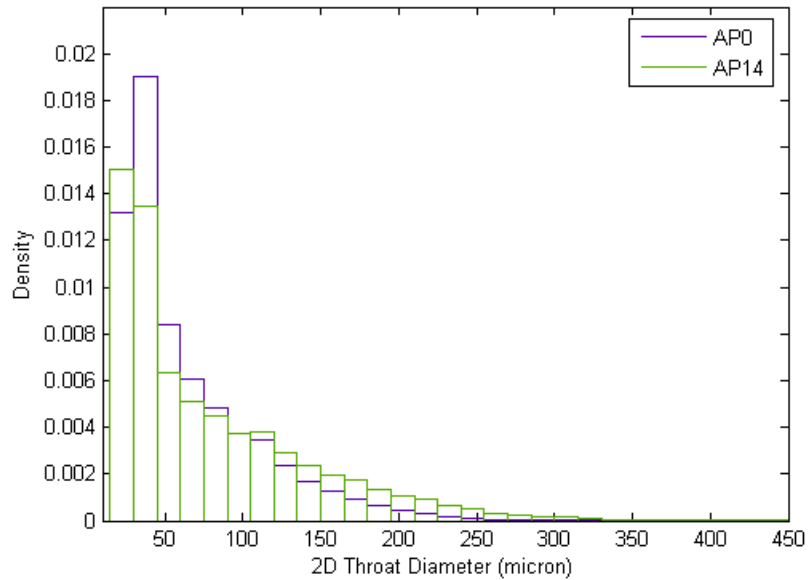


Figure 5.21 2-D Throat Diameter Distributions of AP0 and AP14

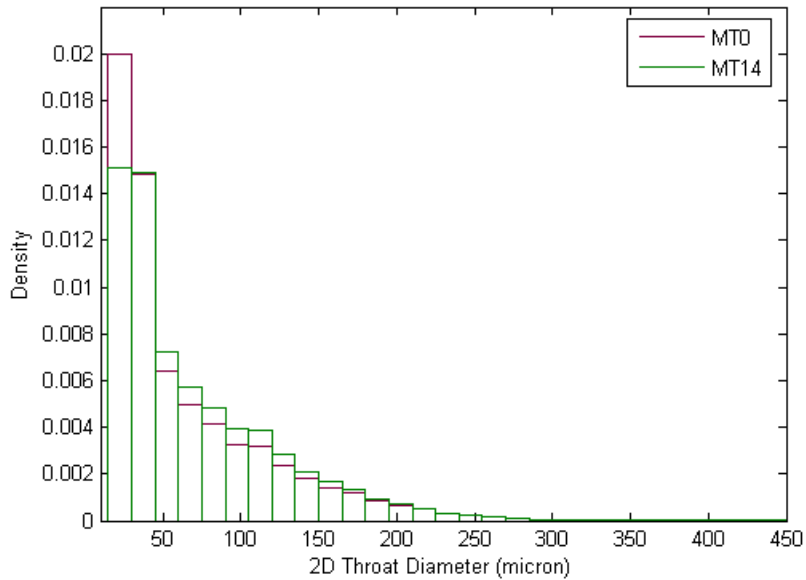


Figure 5.22 2-D Throat Size Distribution of MT0 and MT14

The throat size measurement results for the four samples are listed in Table 5.4. It is noted that throat size shows similar trends as the pore size and local void ratio measurements. For example, AP14 and MT14 have higher mean throat size than AP0 and MT0 respectively, indicative of dilation in the specimens. Furthermore, AP0 shows a smaller coefficient of variation than AP14. However, for moist tamped specimens, MT0 shows a larger coefficient of variation than MT14.

Table 5.4 Statistical Parameters of 2-D Pore Throat Diameter (micron)

Sample	μ	σ	CV (%)	Hv
AP0	61.231	45.962	75.1	0.672
AP14	76.922	64.723	84.1	0.767
MT0	62.139	54.168	87.2	0.698
MT14	67.839	53.917	79.5	0.751

The entropy of throat size distribution of AP0 is 0.672 which is lower than 0.698 of MT0. This means that the AP0 throat size distribution has a lower degree of disorder. The entropy of the throat size distribution of AP14 is the largest among the four samples.

5.5 Effects of Preparation Method and Shearing-Induced Evolution of Structure

5.5.1 Effects of Preparation Method

The effects of preparation method on the structure of the specimen were studied by comparing the 2-D pore size, local void ratio, and 2-D throat size of the samples. The entropy for local void ratio distribution, pore size distribution and throat size distribution consistently shows that MT0 specimen has a higher degree of disorder than the AP0 one. In addition, a comparison of the standard deviations of the local void ratio distribution, the pore size distribution and the throat size distribution between AP0 and MT0 shows high dispersion of each distribution for MT0. It can be consequently concluded that air pluviated specimens have more uniform soil structure in terms of pore size, throat size and local void ratio distribution.

5.5.2 Shearing-Induced Structure Evolution

Shearing induced structure evolution is studied by comparing specimens AP0 and AP14 and specimens MT0 and MT14. Both the coupons of AP14 and AP0 used in this study were cut from the center of the whole specimen. AP14 is located in the dilation region of the specimen. This is confirmed by that fact that the void ratio of AP14 is higher than AP0. For the three parameters studied in this chapter, 2-D pore size, 2-D throat size and local void ratio distribution, AP14 always has a larger coefficient of

variation than AP0. In addition, from the distribution plots of the three parameters, it can be observed that the curves shift towards the right and the peaks decrease as axial strain increases (from 0% to 14%).

The void ratio of MT14 is larger than MT0, which confirms it is located in the dilation region inside the whole specimen. The distribution curves display similar trend as AP0 and AP14. However, the change in entropy from MT0 to MT14 is less than that from AP0 to AP14, which is consistent with the localization happened in MT14 specimen. This is also confirmed by the lower mean pore size and mean throat size of MT14.

CHAPTER VI

3-D CHARACTERIZATION OF SPECIMEN MICROSTRUCTURE

6.1 Introduction

The two-dimensional image analysis studies discussed earlier have provided valuable insight into the microstructure of triaxial test specimens. In addition, the results presented have confirmed the findings of earlier studies, albeit using larger serially acquired images in the present study. As noted earlier, no 3-D studies on the pore structure of triaxial test specimens have been performed to date. There are quantitative tools, such as the stereology method, that can be used to measure some geometric parameters (e.g., porosity and specific surface area) from 2-D images and used to estimate equivalent 3-D parameters (Underwood, 1970). However, some geometric and morphological information regarding a three-dimensional structure cannot be inferred from observations on two-dimensional sectioning planes (Fredrich, 1999; Moreau et al., 1999; Tewari and Gokhale, 2000). Hence, three-dimensional characterization is of interest, not only to provide better quantification of the initial microstructure of a soil specimen but also to improve the understanding of the structure changes in soil specimens when loaded.

In this chapter, particles and pores in the 3-D reconstructed microstructure were visualized using the software packages VoxBlast and 3DMA. Three-dimensional microstructure analyses were also performed on the four samples (AP0, AP14, MT0 and

MT14) using 3DMA. Parameters, such as void ratio, pore throat size, pore radius, and tortuosity were calculated for each reconstructed 3-D structure. The results were also compared with those from 2-D image analysis.

It is important to point out that, due to the issues discussed in Chapter 4 regarding the inability of the algorithms used in 3DMA to partition the pore space correctly when none or few contacts exist between particles, 2-D dilation and 3-D morphological operations were applied to the structure before using the program to the 3-D reconstructed structure, so that the software can process the data correctly. As a result, while the relative values of measured parameters are expected to be reasonable, the absolute values are expected to be offset from the true measures due to the dilation and morphology operations used. In this study, a volume of size 600 x 600 x 600 voxels was used for pore size, throat size and tortuosity calculations.

6.2 Visualization of Particles and Pores

After 3-D reconstruction of the microstructure, it is possible to visualize single particles and pores using VoxBlast. In this section, six particles of different sizes and two pores are visualized. Six views (Positions are shown in Figure 6.1) of each particle are shown in Figures 6.2 to 6.7 as examples of the individual particles produced by the reconstruction process. All particles are shown at the same scale and reflect the full range of particle sizes in the reconstructed specimens. Particle 6 (Figure 6.7) was the largest particle identified in specimen AP14. It can be seen that all of the particles are rounded or sub-rounded. The particle shown in Figure 6.4 (Particle 3) is slightly more angular than the others.

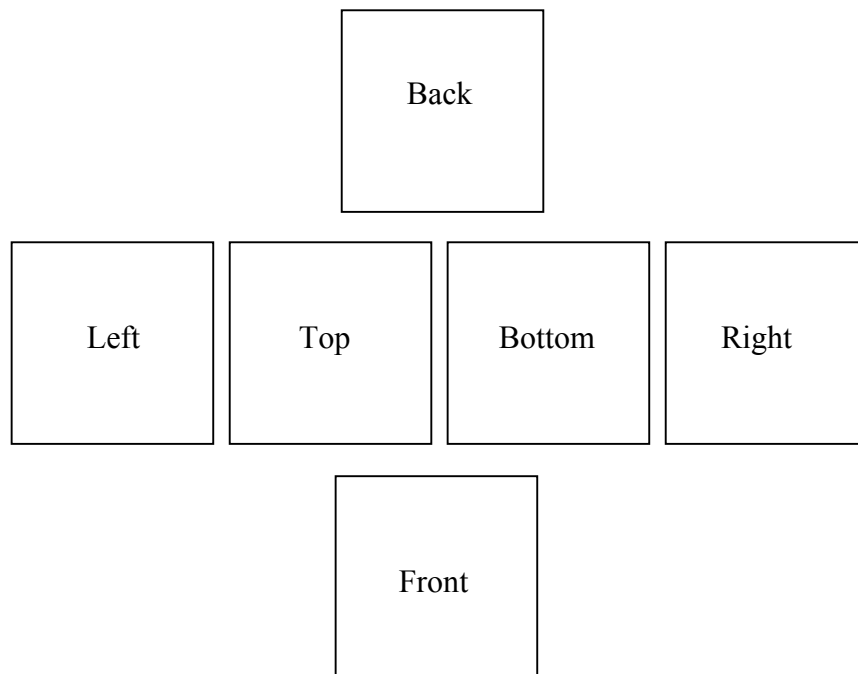


Figure 6.1 Illustration of the View Locations of Particles in Figures 6.2 to 6.7

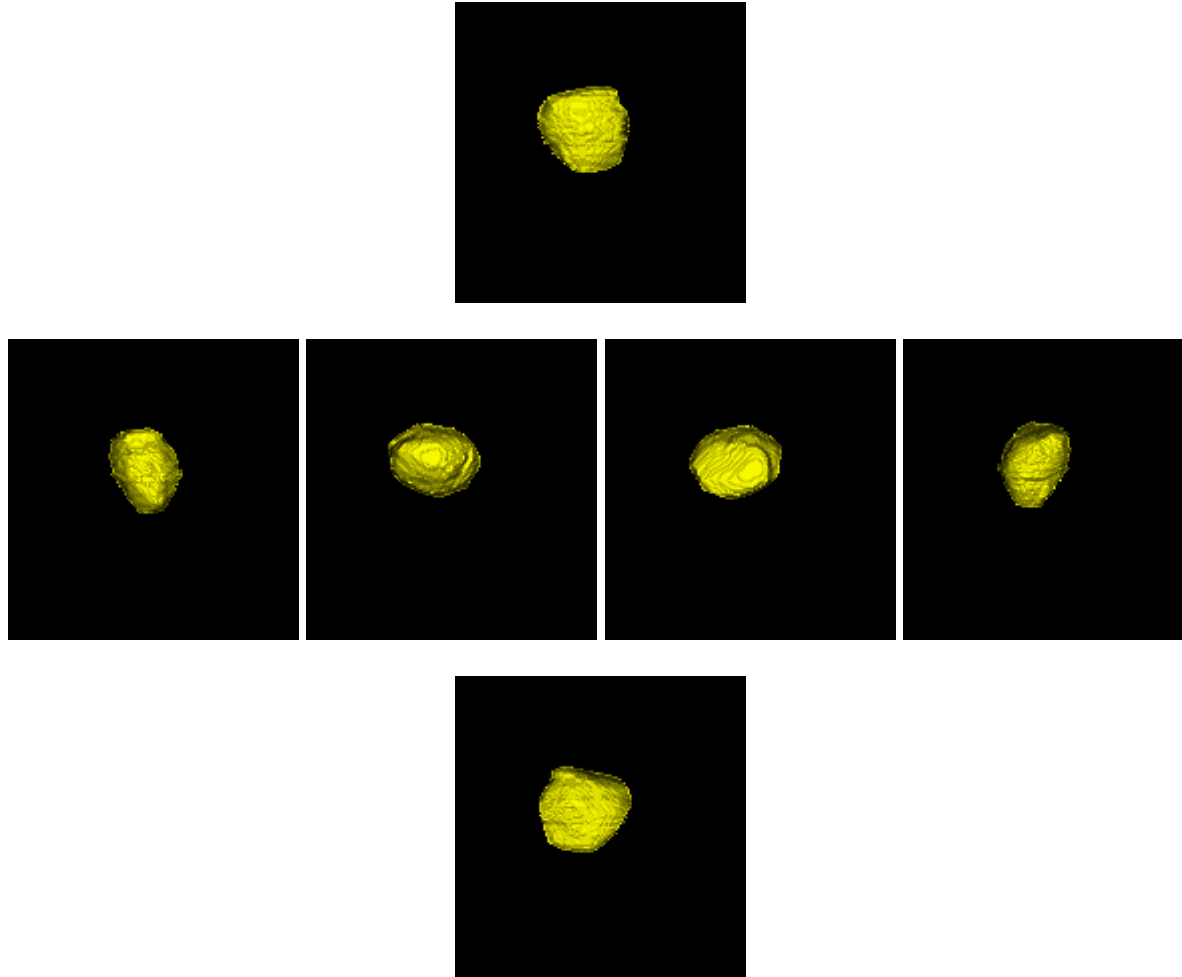


Figure 6.2 Particle 1

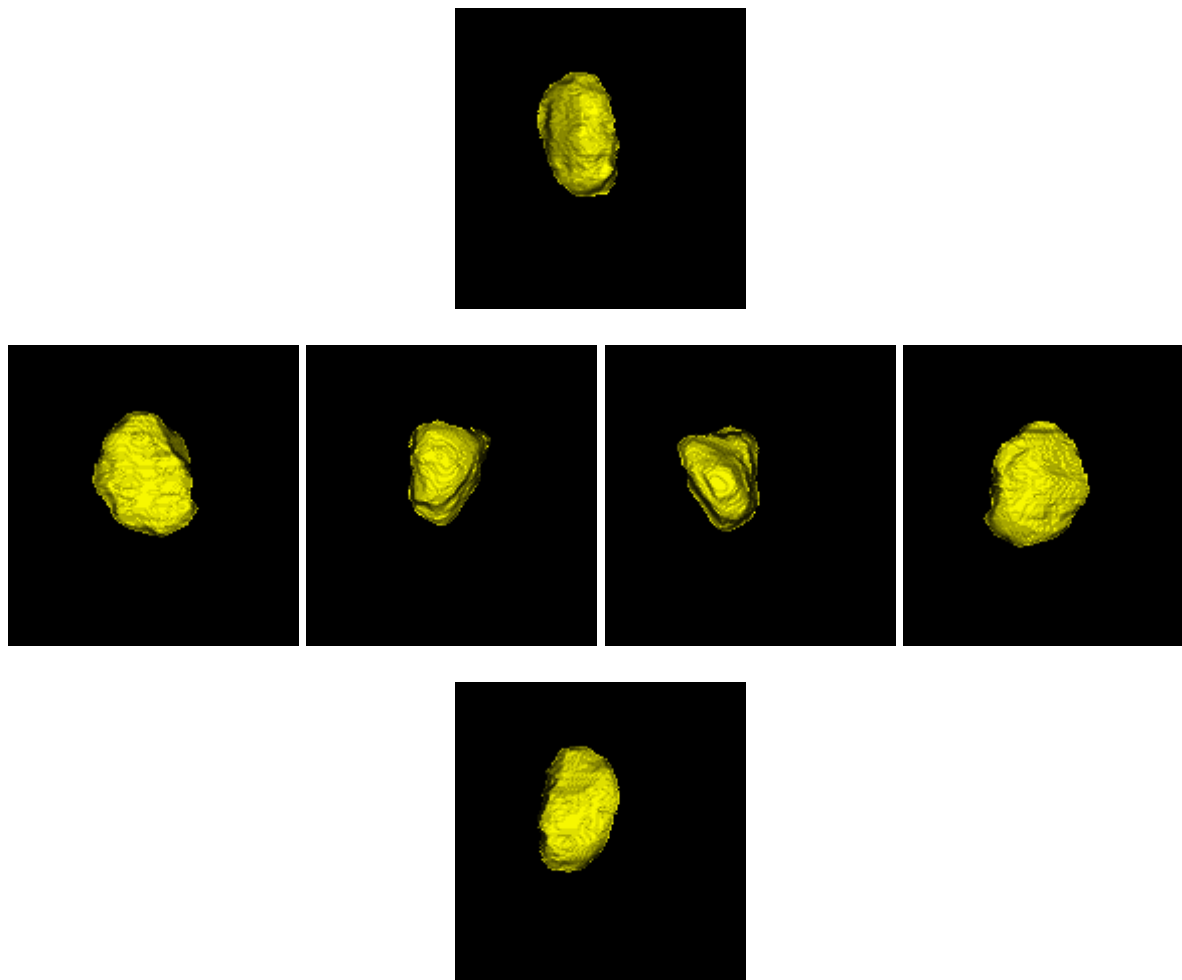


Figure 6.3 Particle 2

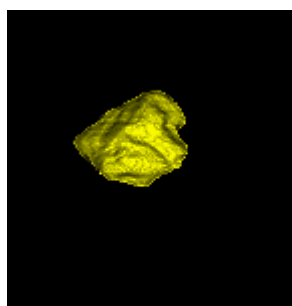
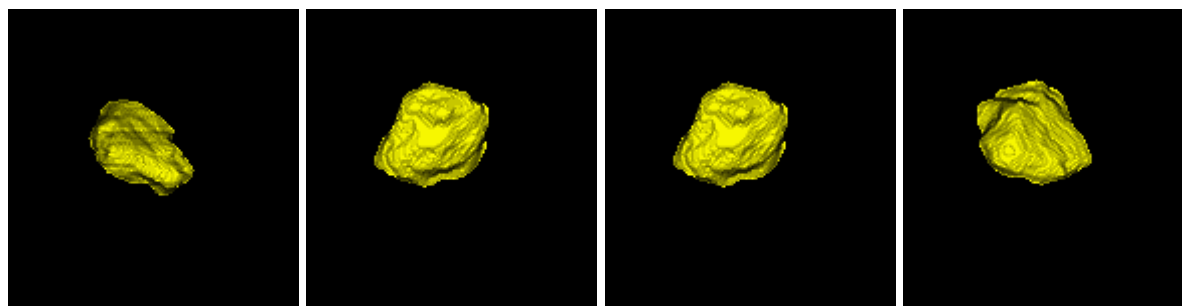
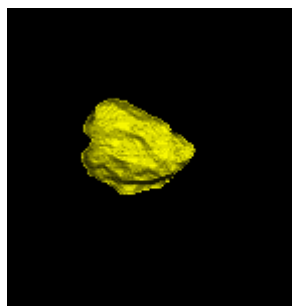


Figure 6.4 Particle 3

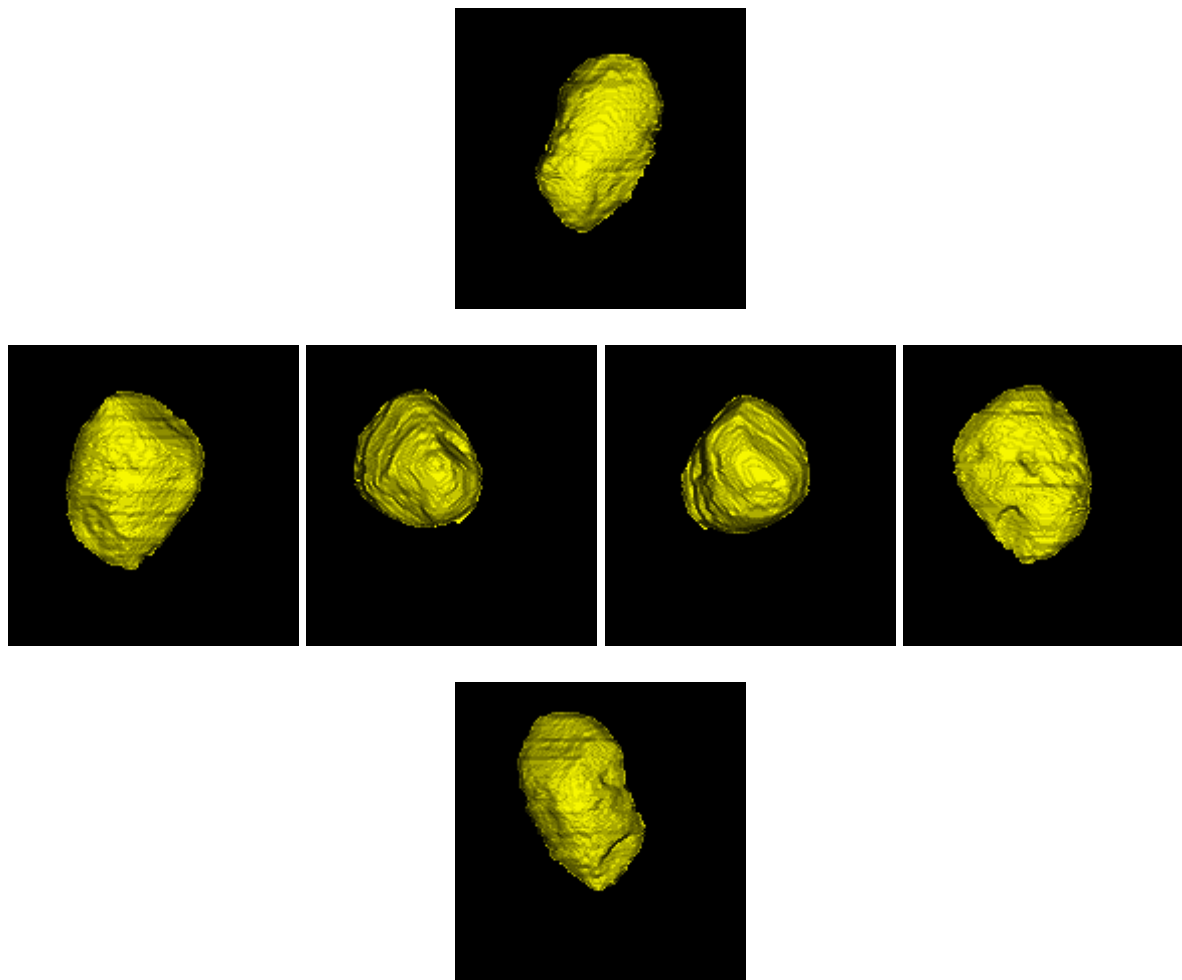


Figure 6.5 Particle 4

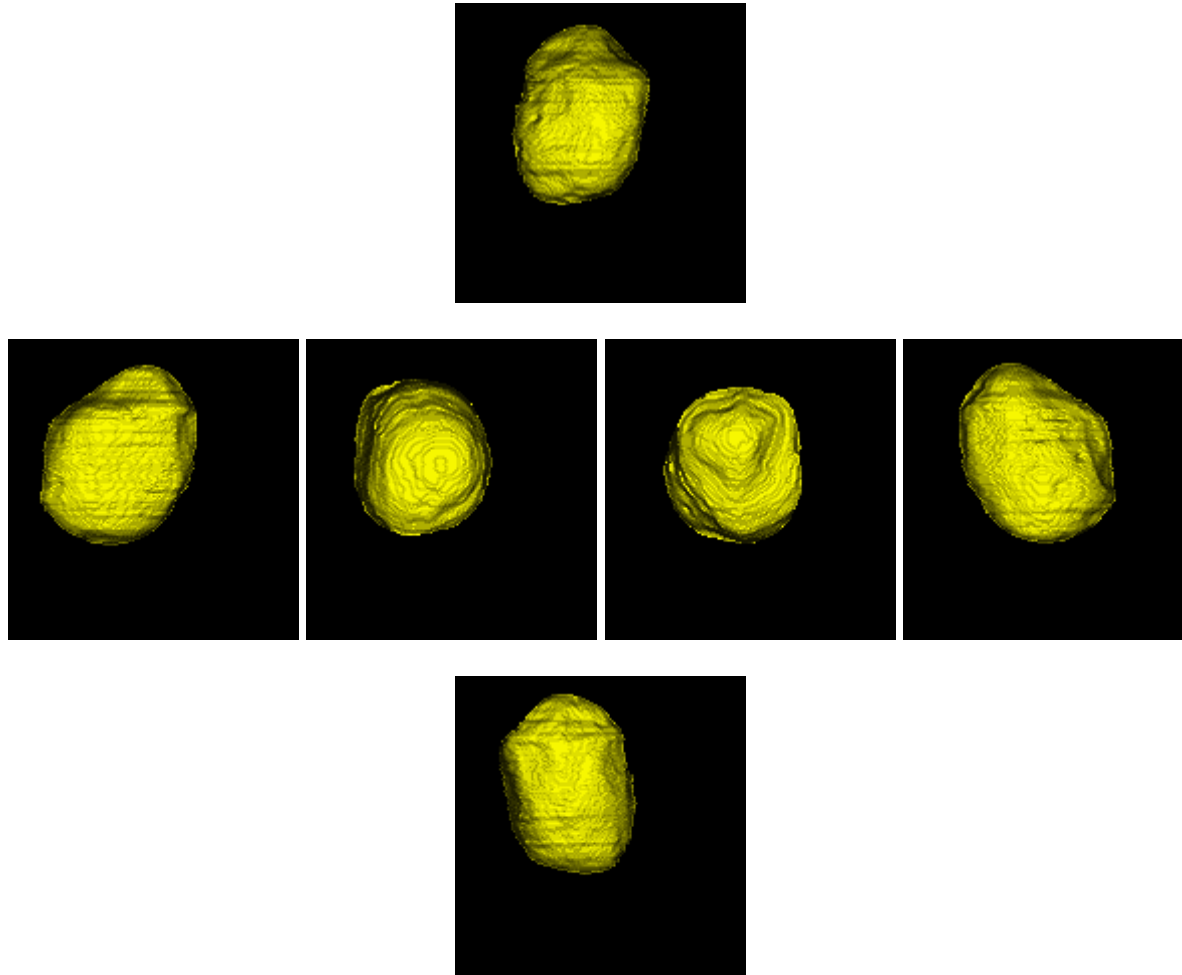


Figure 6.6 Particle 5

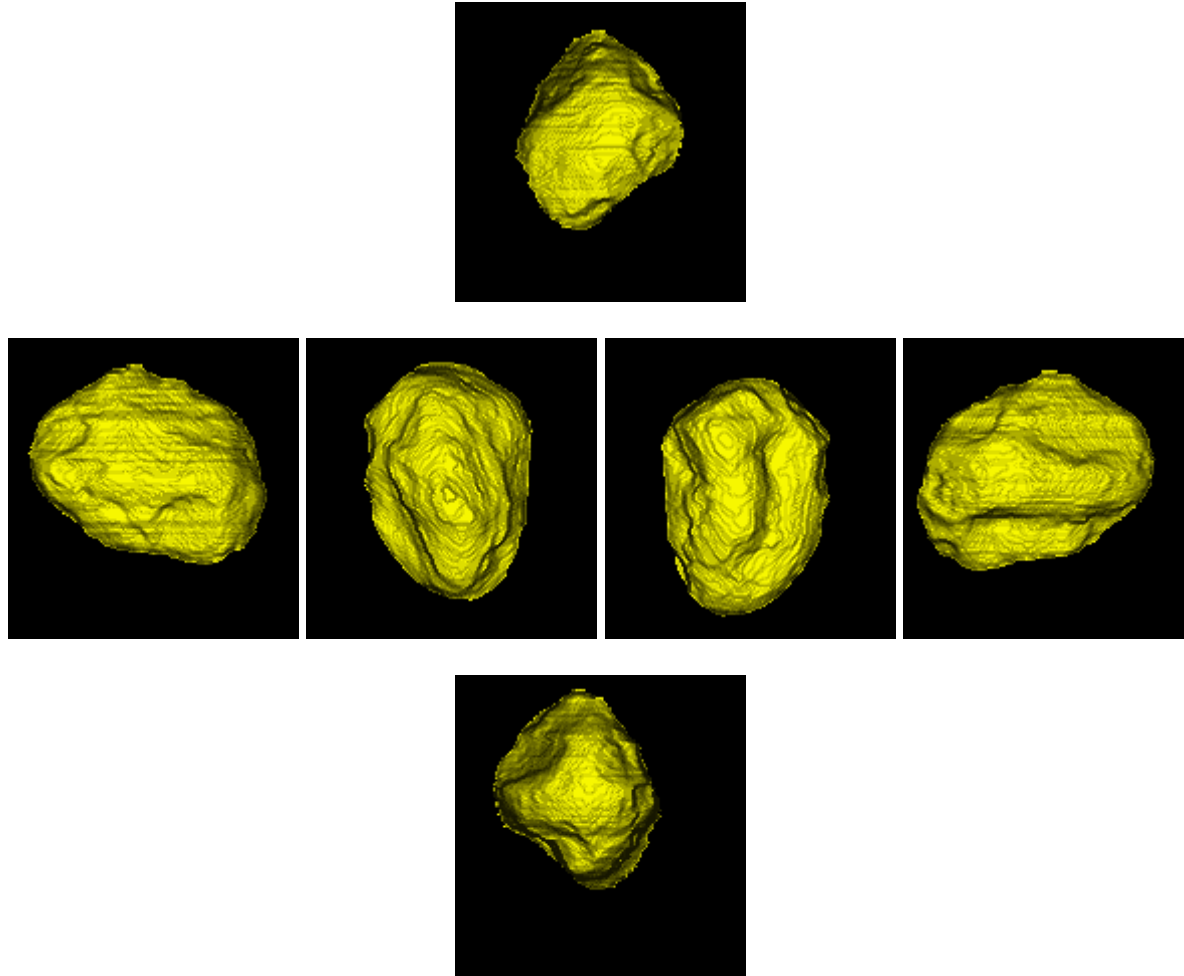


Figure 6.7 Particle 6

An example pore structure is presented in Figures 6.8 and 6.9. An isometric view looking down on the pore is shown in Figure 6.8 with an increasing number of slices being used in images (i) through (ix). The number of slices in these images increases from 10 to 90. It can be seen that in image (ix) the bottom of the particle immediately above the pore has just begun to appear. Accordingly the height of the pore is about 60 slices (about 480 micron) which is larger than the mean particle diameter. The front view of the same shown in Figure 6.8 (ix) is shown in Figure 6.9 (i), and illustrates the pore path characteristics in the horizontal direction as additional slices are removed from the front of the volume. Images (i) through (xii) sequentially show the volume as 10 slices are removed from the front in each successive view. The pore can be seen to extend from about image (iii) to image (xi) reflecting a length in this orientation of about 80 slices (640 micron). Accordingly the pore in Figures 6.8 and 6.9 is seen to have an elongation ratio of about 1.5. A second pore structure is shown in Figure 6.10 and 6.11. A similar assessment of the pore in the various images suggests it has a length of about 80 voxels (640 micron) also. The width is estimated to be between 200 and 300 micron and the height is estimated to be between 400 and 500 micron also. The throat connecting the pore to an adjacent pore behind the volume shown can be clearly seen in all the images in Figure 6.10. Due to the convex particles surrounded the pore structures, it can be seen from all of the different views of the pore structures, that the pore shapes can be generally described as concave. This is confirmed by the typical pore body generated by 3DMA after pore space partitioning. Figure 6.12 (a) is a typical single pore body defined by 3DMA with the medial axis through it shown in Figure 6.12 (b).

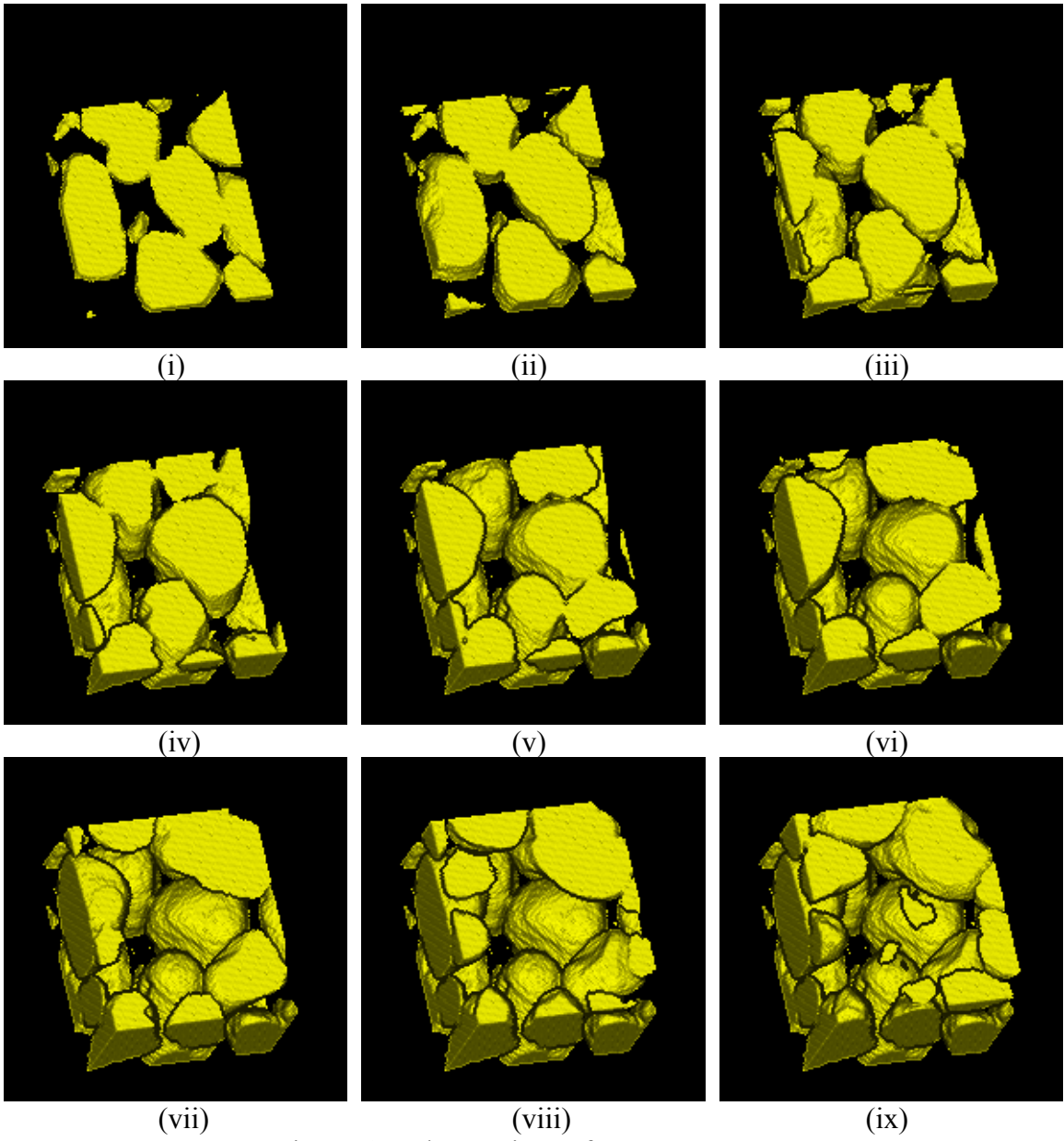


Figure 6.8 Observations of Pore Structure 1

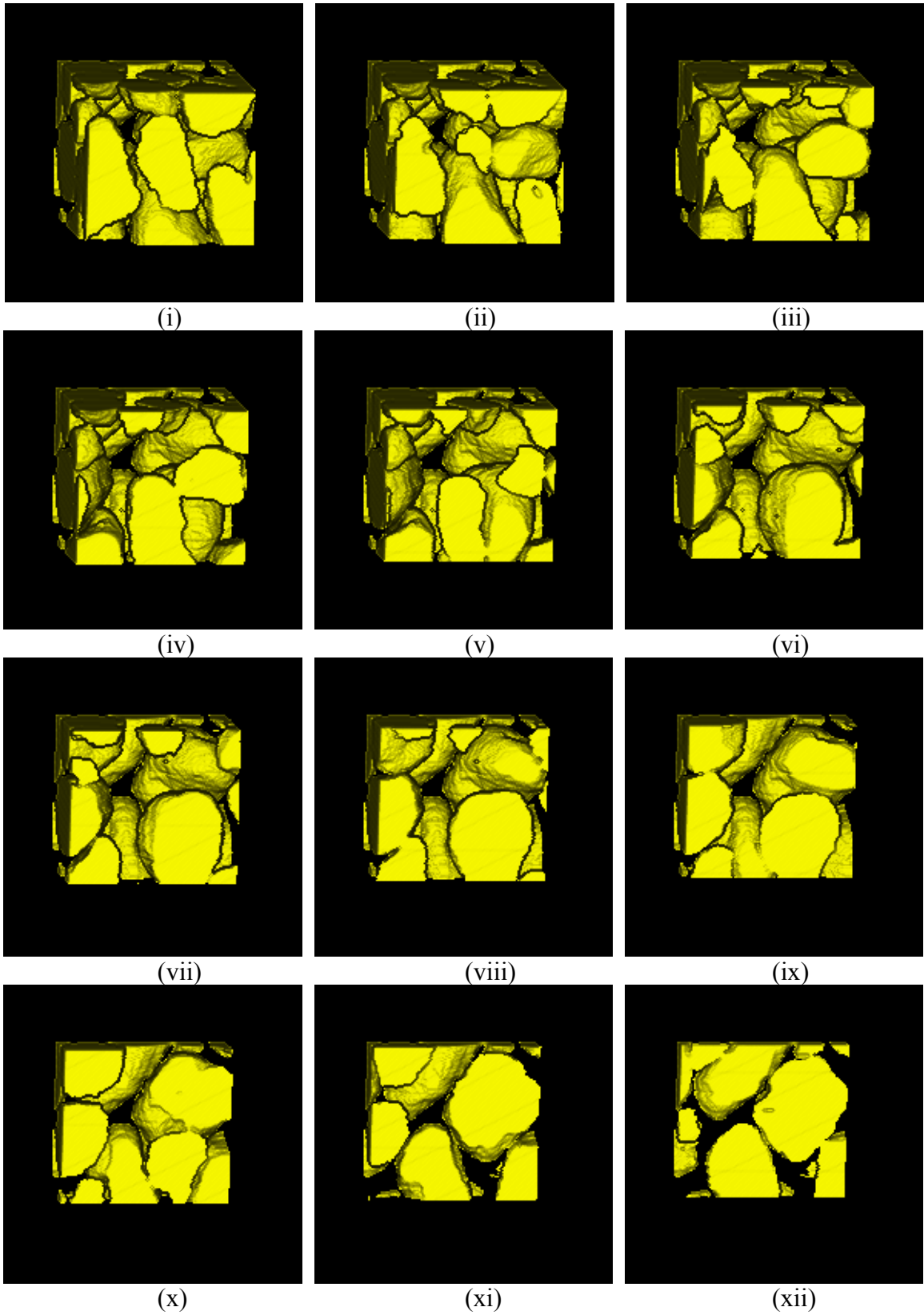


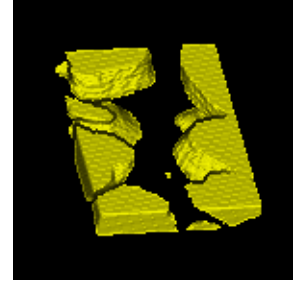
Figure 6. 9 Front Views of Pore Structure 1 at Different Depths



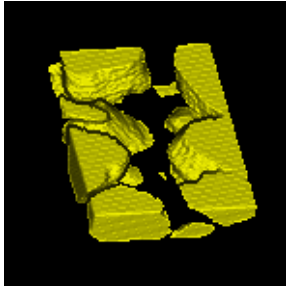
(i)



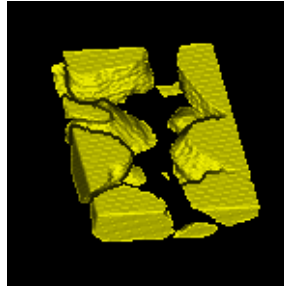
(ii)



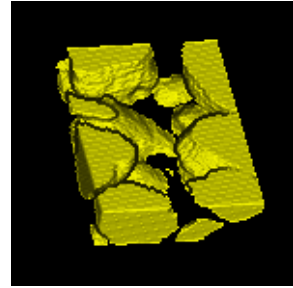
(iii)



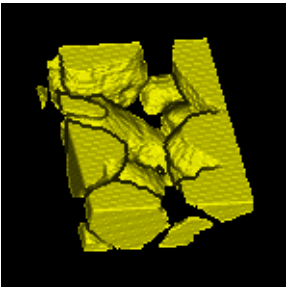
(iv)



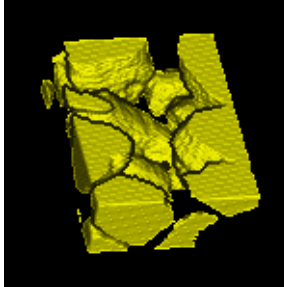
(v)



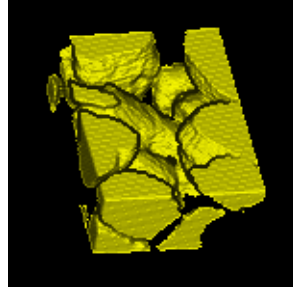
(vi)



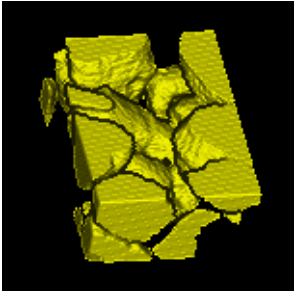
(vii)



(viii)



(ix)



(x)

Figure 6.10 Observations of Pore Structure 2

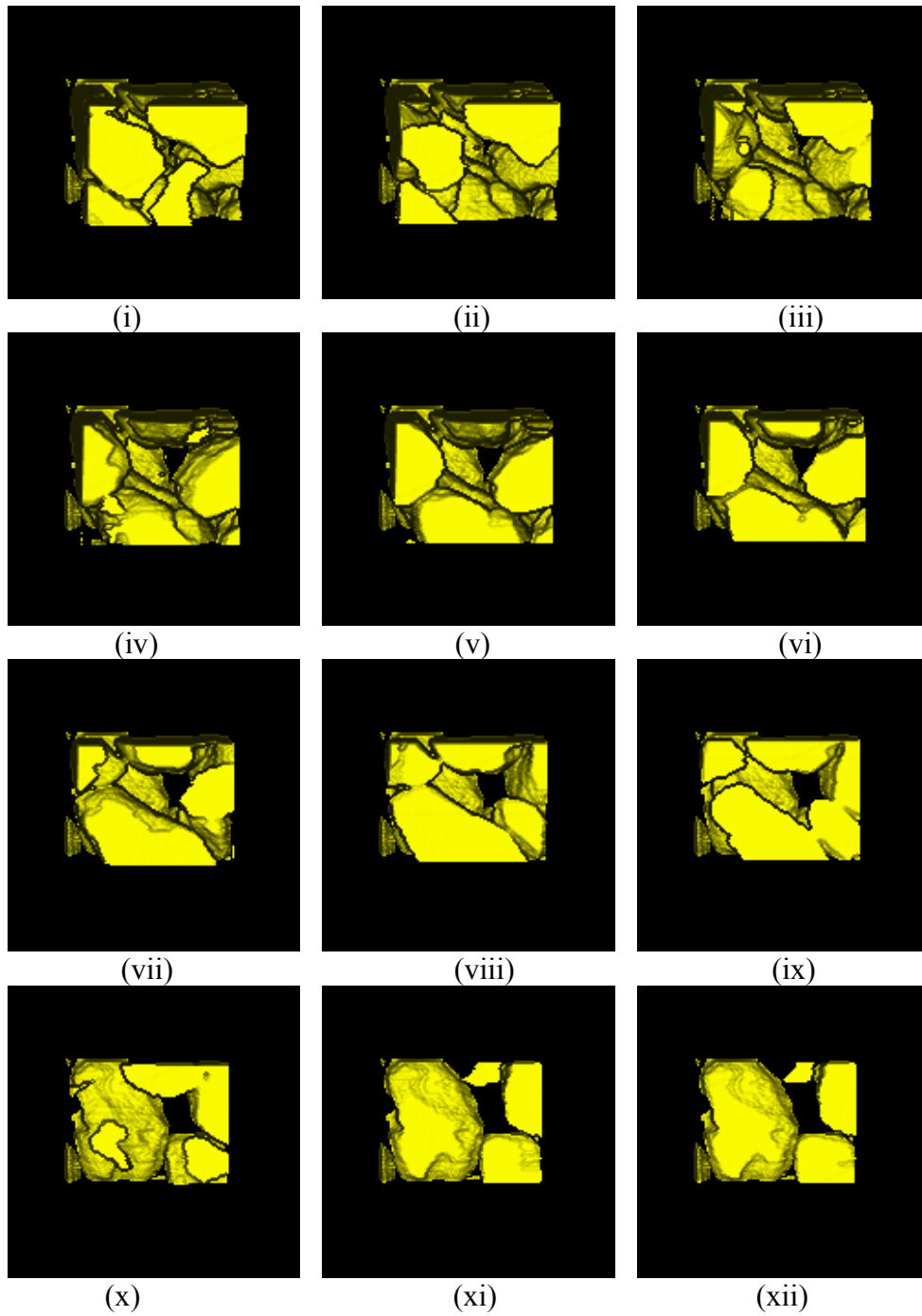
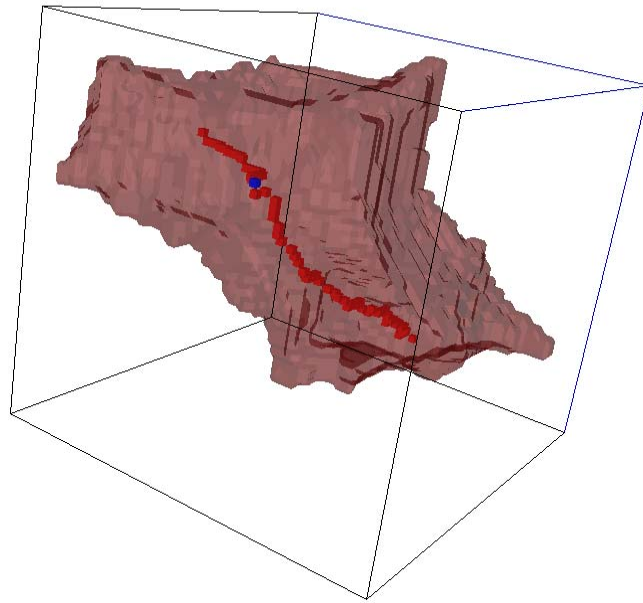
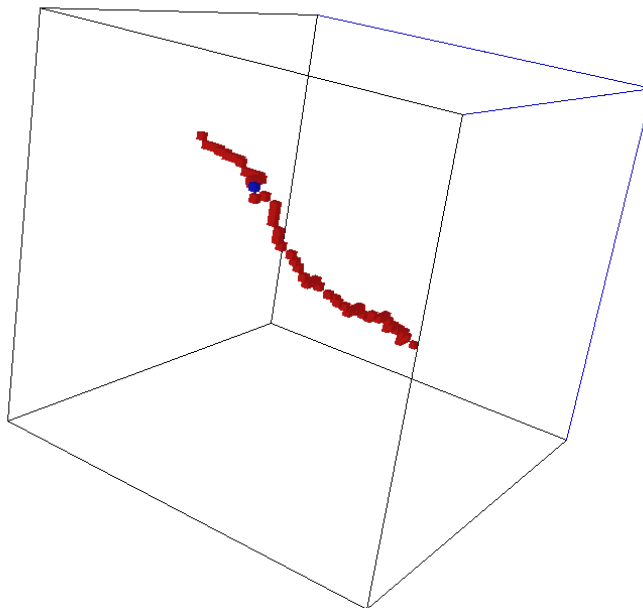


Figure 6.11 Front Views of Pore Structure 2 at Different Depths



(a)



(b)

Figure 6.12 Visualization of Pore Structure and Medial Axis (a) Visualization of a Single Pore Body and Medial Axis from 3DMA; (b) Visualization of Medial Axis of a Single Pore Body from 3DMA

6.3 Void Ratio

The void ratio of a 3-D structure is based on voxel count. 3-D void ratios of the four samples used in this research along with the 2-D void ratios reported earlier are listed in Table 6.1 for comparison. They are also plotted against each other as shown in Figure 6.13. Since the resolution in x, y and z directions used in 3-D reconstruction of the microstructure of the specimens in this study is the same, the results of void ratio from 2-D and 3-D are expected to be the same as displayed. If different resolutions were used, then variations could be expected.

Table 6.1 Porosity Information of Four Samples

Sample	2-D porosity	3-D porosity	2-D Void Ratio	3-D Void Ratio	Experimental Measurement of Void Ratio
AP0	0.365	0.365	0.575	0.576	0.582
AP14	0.417	0.417	0.715	0.716	N/A
MT0	0.365	0.365	0.575	0.575	0.580
MT14	0.413	0.415	0.704	0.709	N/A

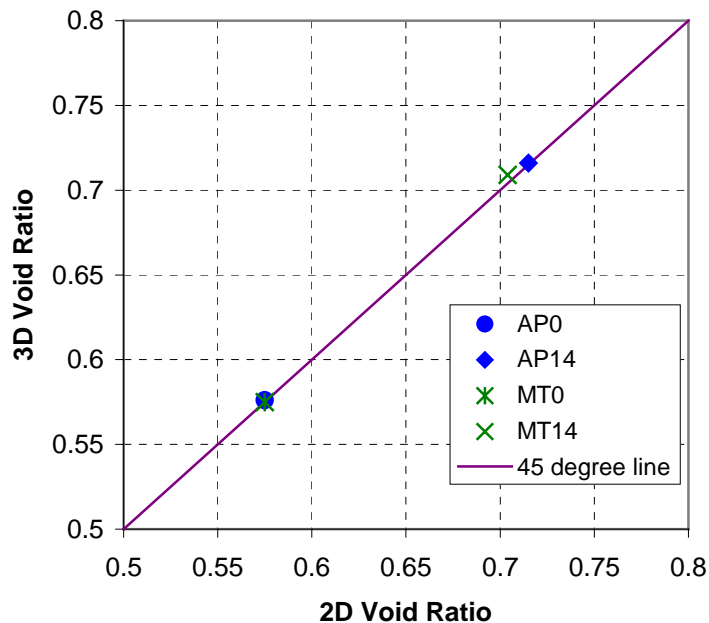


Figure 6.13 2-D and 3-D Void Ratio of Four Samples AP0, AP14, MT0 and MT14

Specimen AP14 which was cut from a specimen that was globally dilating shows the highest void ratio (0.716) amongst the four specimens. The void ratio of MT14 is 0.709. The slightly smaller value may be consistent with the fact that the coupon taken from the moist tamped specimen sheared to $\epsilon=14\%$ was not globally sheared to the same extent due to the localization that was observed.

6.4 3-D Throat Size

As described in Chapter 4, 3-D pore throats, which are used to partition the pore space, were identified by using the “wedge finding” algorithm. An example of the distribution of the throat surfaces identified by 3DMA is shown in Figure 6.14.

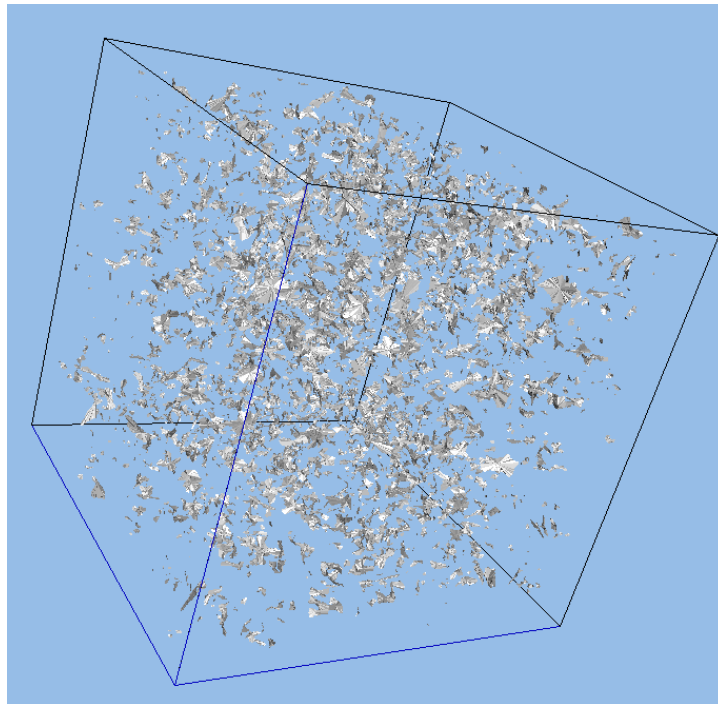


Figure 6.14 Throat Surfaces of AP0 (600 x 600 x 600 voxels)

The 3-D throat size distributions of AP0 and MT0 are displayed in Figure 6.15 to allow preparation induced structure variation to be studied. AP0 has more small throats. The mean throat surface area of AP0 is 6690 micron². The mean throat size for MT0 is 8996 micron².

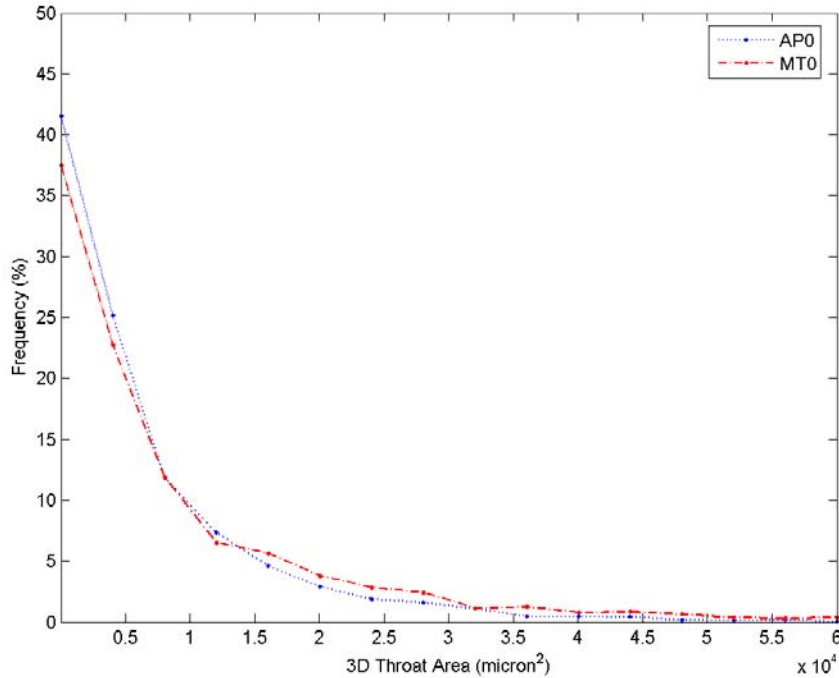


Figure 6.15 Comparison of 3-D Throat Size of AP0 and MT0

The 3-D throat size distribution of AP0 and AP14 is shown in Figure 6.16. It can be observed from the graph that AP14 has more large throats than AP0. The mean pore throat size of AP0 is smaller than for the corresponding sheared sample AP14 (11,527 micron²). This is consistent with the fact that sample AP14 is from the dilated region inside the globally sheared specimen. The difference of the 3-D throat size distribution between MT0 and MT14 (Figure 6.17) is not as distinct as AP0 and AP14. In fact, the mean throat size of MT0 is only slightly larger than that of MT14. This finding is attributed to the fact that density and thus throat-size layering can occur with moist

tamping and thus direct comparison between MT0 and MT14 may not be appropriate since spatial variability and not material shearing may be dominating the differences in the observed values of the volumes being evaluated.

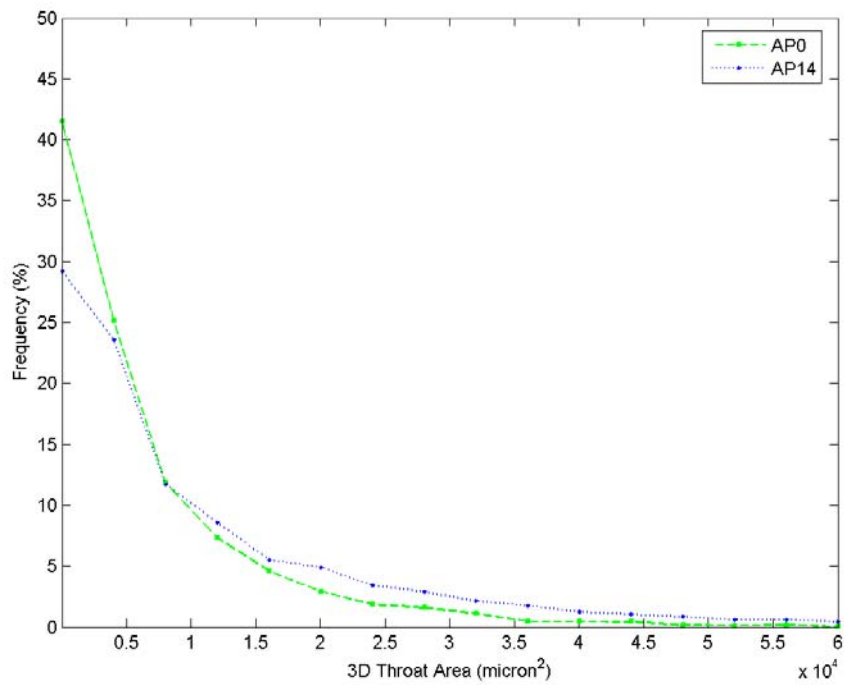


Figure 6.16 Comparison of 3-D Throat Size of AP0 and AP14

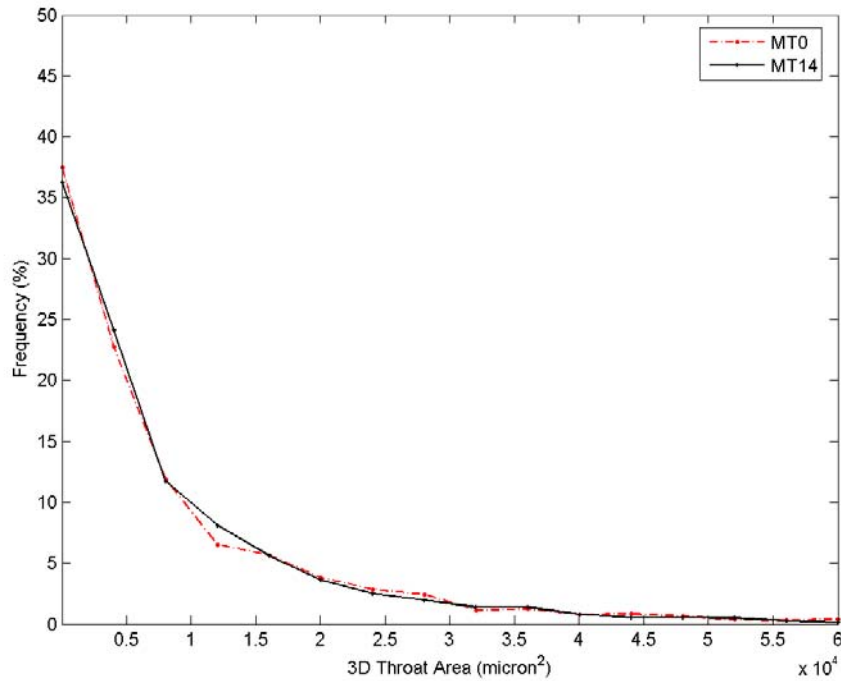


Figure 6.17 Comparison of 3-D Throat Size of MT0 and MT14

6.5 3-D Pore Size

After the throats are constructed, the pore space is partitioned into a series of pore bodies separated by the throat surfaces (Lindquist, 1999). Pore body network statistics were obtained for the partitioned structure.

AP0 and MT0 were compared in Figure 6.18 in terms of 3-D pore size distribution to study preparation-induced variation. The distinct differences between AP0 and MT0 occurred for pore diameters between 100 and 150, and 200 and 400 microns. Between 100 and 150 microns, AP0's values are higher. However, in the range of 200 and 400 microns, MT0 has higher number of pores. This suggests that capillary effects in moist tamping leads to more larger pores in the 200 to 400 micron diameter range. The differences in the distributions in these two ranges (100 ~ 150 microns and 200 ~ 240

microns) are comparable (or even larger) than the differences shown in Figures 6.19 and 6.20 for shearing induced evolution in the microstructure. Similar observations were also made by Frost and Jang (2000).

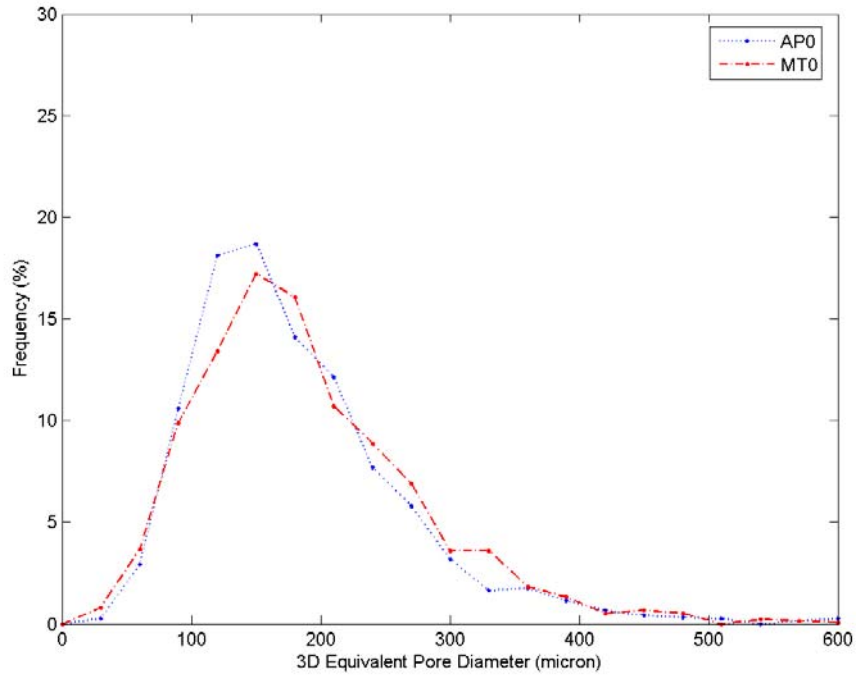


Figure 6.18 Comparison of 3-D Pore Size Distribution of AP0 and MT0

To study shearing induced evolution of the microstructure, the 3-D pore diameter distributions for AP0/AP14 and MT0/MT14 were plotted in Figures 6.19 and 6.20, respectively. It can be seen in the plots that there are more large size pores identified by 3DMA in sample AP14 than in AP0. This is consistent with the fact that AP14 is located in the uniformly dilated region of the specimen. In contrast, MT0 is also shifted to the right in Figure 6.20. The frequency peaks are further away from each other in MT0 and MT14 than in AP0 and AP14. This trend is opposite to the 2-D pore size measurement results. The possible causes of this result are the algorithm used in the software to

partition the pore space (Lindquist, 2005) and the 3D morphological operations performed on the non-uniform structure.

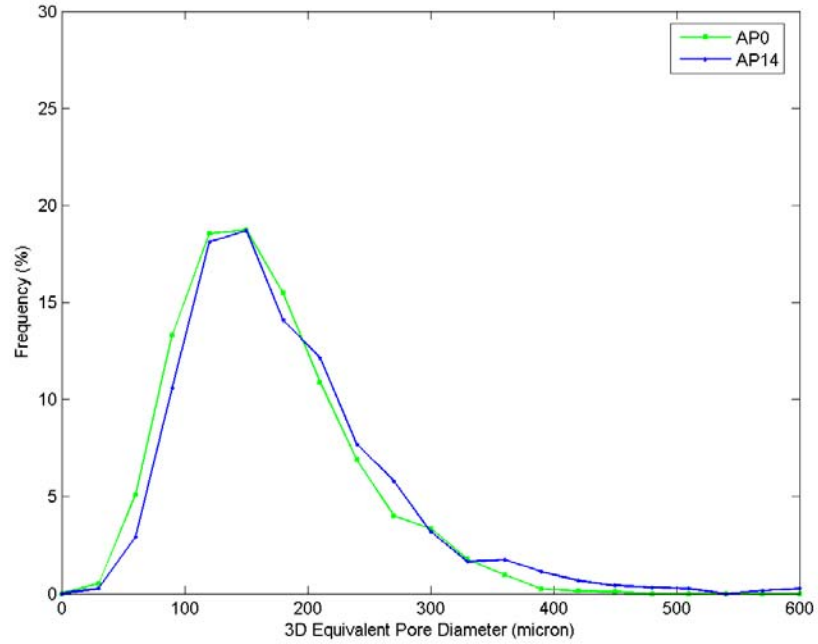


Figure 6.19 Comparison of 3-D Pore Size Distribution of AP0 and AP14

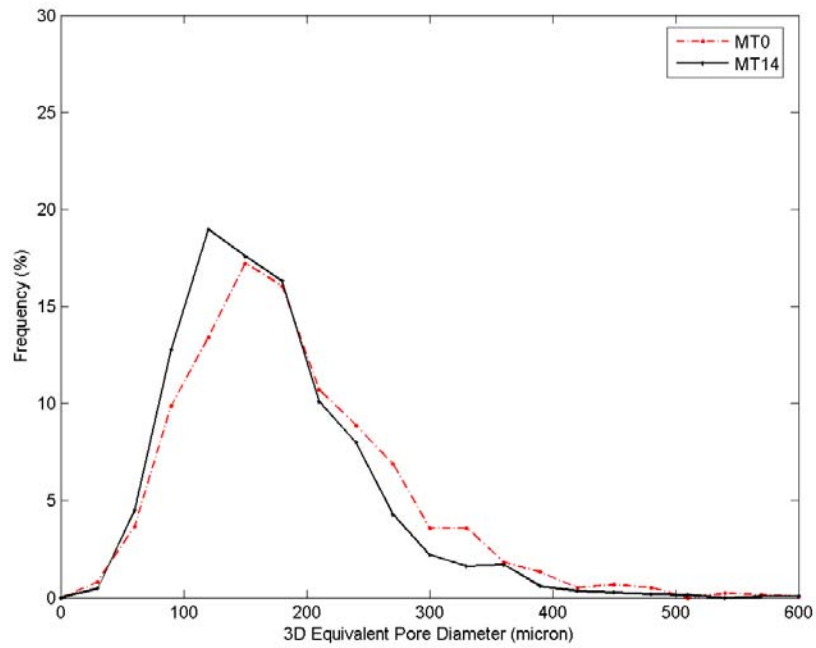


Figure 6.20 Comparison of 3-D Pore Size Distribution of MT0 and MT14

The mean, standard deviation, and coefficient of variation of pore size distribution and number of pores of each sample are listed in Table 6.2. Mean pore size is plotted against the standard deviation of pore size for each sample in Figure 6.21. Standard deviation increases with the mean pore size. The coefficient of variation of sample AP0 is the lowest of the four, which is indicative of the most uniform structure. In addition, the coefficient of variation of MT0 is higher than MT14. This may again be due the preparation induced variations inside the moist tamped specimen.

Table 6.2 Mean, Standard Deviation, and Coefficient of Variations of 3-D Pore Diameter of Four Samples

Sample	μ	σ	Number of Pores	CV (%)
AP0	165	67.489	2152	41.0
AP14	182	83.505	1953	45.9
MT0	189	85.782	1364	45.3
MT14	170	74.165	2405	43.7

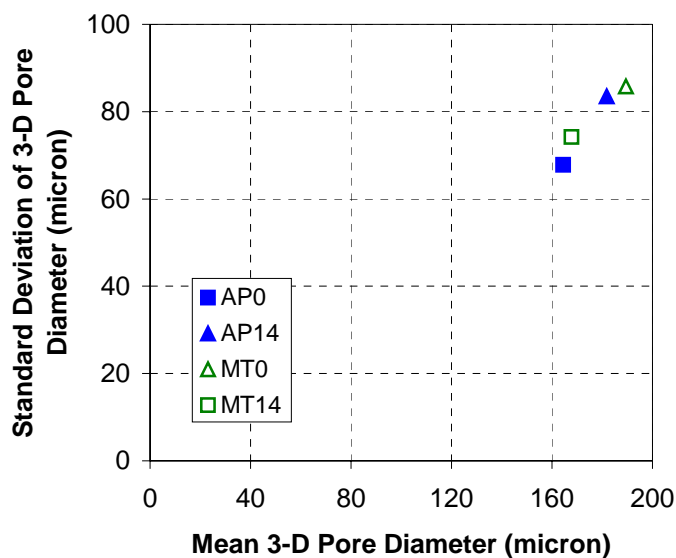


Figure 6.21 Mean 3-D Pore Diameter vs. Standard Deviation of 3-D Pore Diameter

6.6 Tortuosity

6.6.1 Tortuosity Measurement

Tortuosity is also used in this study to quantify the pore structure in the triaxial test specimens. The tortuosities of paths between two faces of interest through the medial axis network were calculated. Tortuosity is defined as the ratio between the shortest path length and the Euclidean distance between the end voxels of the shortest path.

6.6.2 Size Analysis

To study the effect of volume size (especially the length between the two faces of interest) on the tortuosity calculation for real sand specimens, tortuosity measurements were performed on a serial of sub-volumes as shown in Figures 6.22 and 6.23.

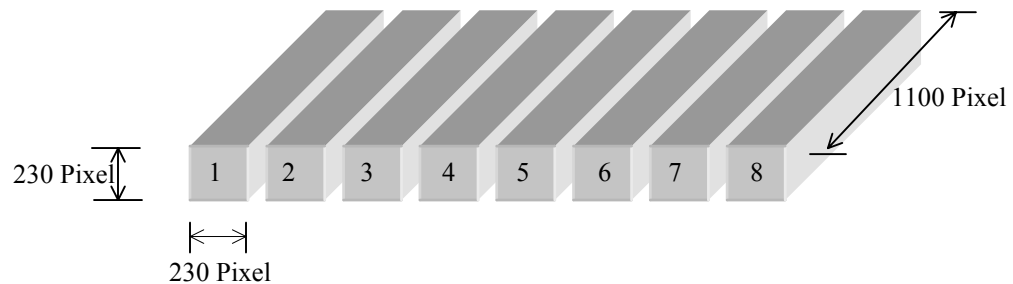


Figure 6.22 Sub-Volumes of Same Size: 230 x 1100 x 230



Figure 6.23 Sub-Volumes of Various Lengths ($L \times 1100 \times 230$; $L=i \times 230$, $i=1 \dots 7$)

The first analysis was performed on 8 sub-volumes cut from AP0, each with the same size of 230 x 1100 x 230 voxels. The second analysis was performed on 8 sub-volumes from AP0 with different lengths (230, 460, 690, 920, 1150, 1380, 1610 and 1800 pixels). The mean tortuosity for each sub-volume of size 230 x 1100 x 230 is very similar, as shown in Figure 6.24.

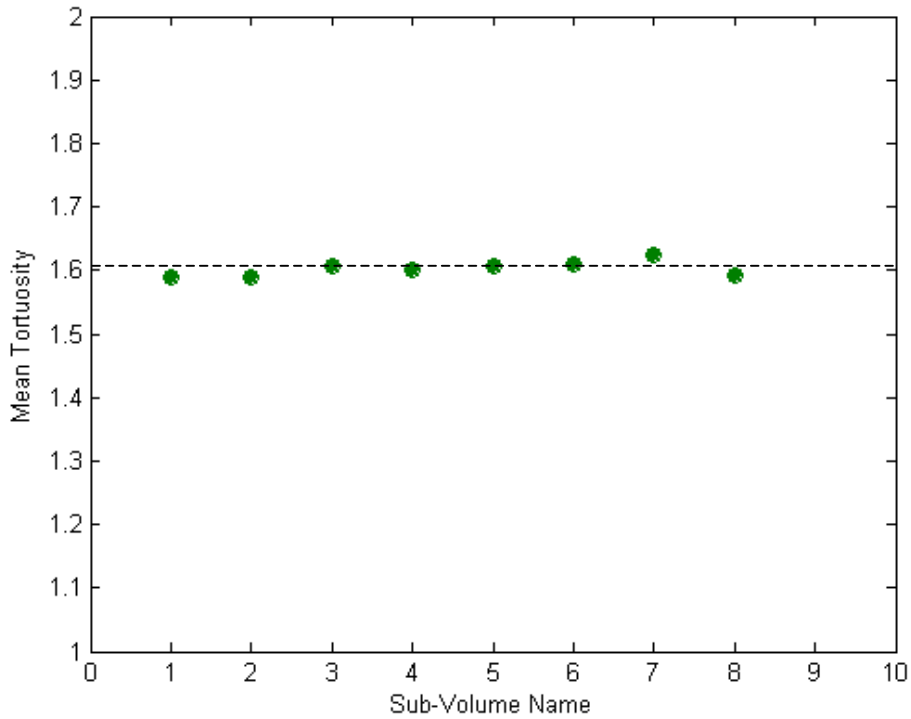


Figure 6.24 Tortuosity of 8 Sub-Volumes of AP0 with Size 230 x 1100 x 230 Voxel

The shortest path length and mean tortuosity are shown in Figure 6.25 and Figure 6.26 as a function of volume size. The mean shortest path length for each volume increases linearly with the total length of the volume. The tortuosity varies when the total face to face length in the volume is less than 500 pixels.

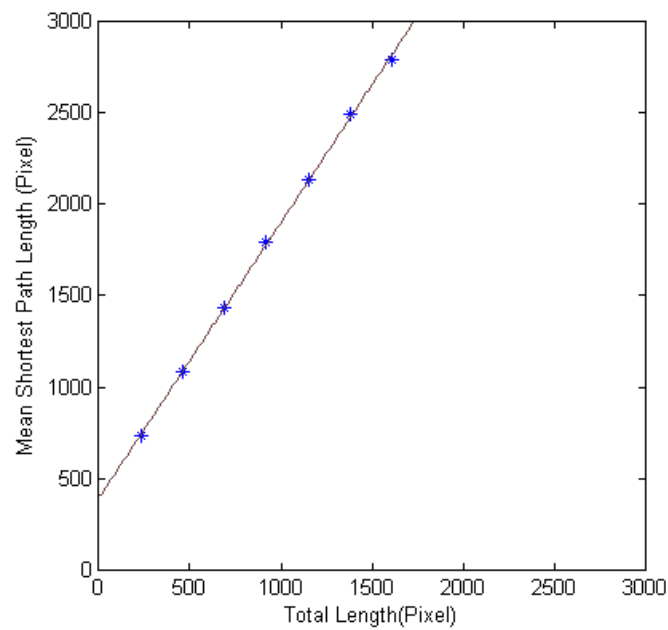


Figure 6.25 Mean Shortest Path Lengths for Each Sub-Volume of Various Length (230, 460, 690, 920, 1150, 1380, 1610 and 1800 Pixel)

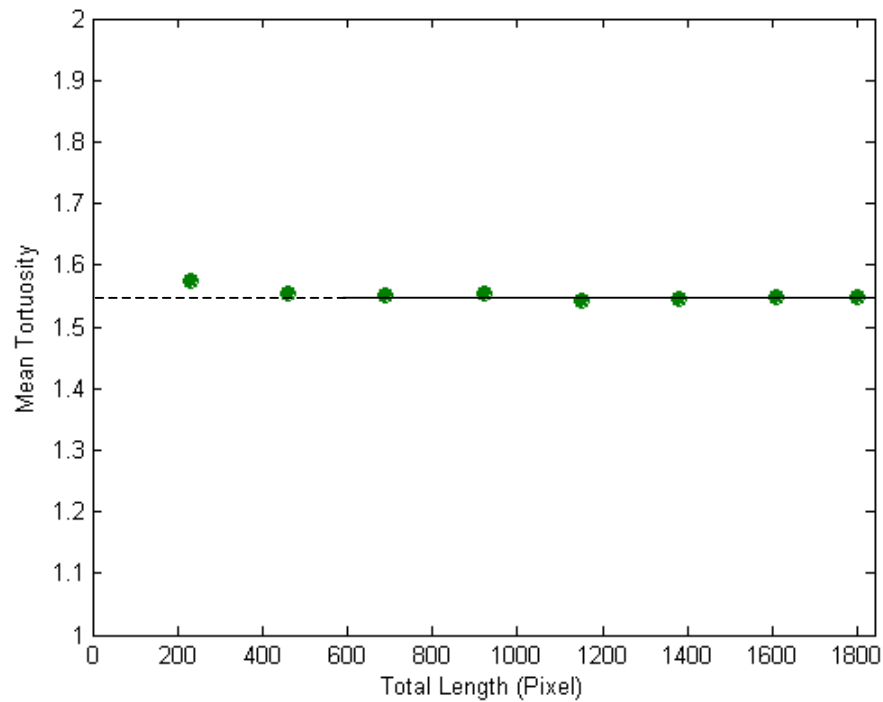


Figure 6.26 Mean Tortuosity for Each Sub-Volume of Various Length (230, 460, 690, 920, 1150, 1380, 1610 and 1800 Pixel)

The corresponding mean tortuosity, standard deviation of tortuosity and the coefficient of variation for each sub-volume are listed in Table 6.3 and Table 6.4. It is found that the coefficient of variation of tortuosity for the 8 same-size sub-volumes are between 4.060 and 4.639. However, for the 8 sub-volumes with different lengths, the coefficient of variation decreases from 4.463 to 1.023 when the length of the volume increases from 230 to 1800 pixels.

Table 6.3 Mean, Standard Deviation and Coefficient of Variation of R_L of Sub-Volume of Size 230x1100x230 Voxels

R_L	V230 1	V230 2	V230 3	V230 4	V230 5	V230 6	V230 7	V230 8
μ	1.591	1.558	1.607	1.601	1.607	1.611	1.633	1.593
σ	0.071	0.063	0.071	0.074	0.074	0.069	0.072	0.066
CV (%)	4.481	4.060	4.433	4.639	4.626	4.284	4.405	4.163

Table 6.4 Mean, Standard Deviation and Coefficient of Variation of R_L of Sub-Volume with Different Length (Width=1100 Pixel; Height=230 Pixel)

R_L	V230	V460	V690	V920	V1150	V1380	V1610	V1800
μ	1.591	1.574	1.555	1.550	1.553	1.542	1.545	1.547
σ	0.071	0.049	0.039	0.034	0.026	0.022	0.019	0.016
CV (%)	4.463	3.088	2.524	2.203	1.682	1.448	1.200	1.023

Based on the above volume size analysis, the critical length of the sample for tortuosity measurement was identified as 500 pixels. In the subsequent section, a 600 x 600 x 600 sub-volume from each sample as was used for pore size and throat size measurements was also used for tortuosity measurements.

6.6.3 Anisotropy of Tortuosity

To study the tortuosity anisotropy for each specimen, tortuosities in the x, y and z directions were calculated. The results from the four samples are compared and plotted in

Figures 6.27 and 6.28. The mean and standard deviation of tortuosity for each sample are summarized in Tables 6.5 and 6.6.

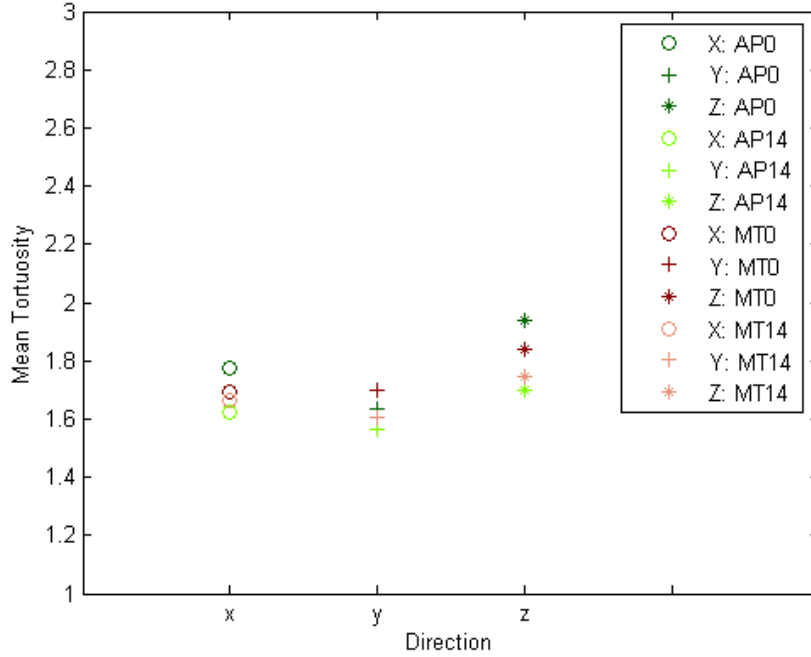


Figure 6.27 Tortuosity in x, y, and z Direction

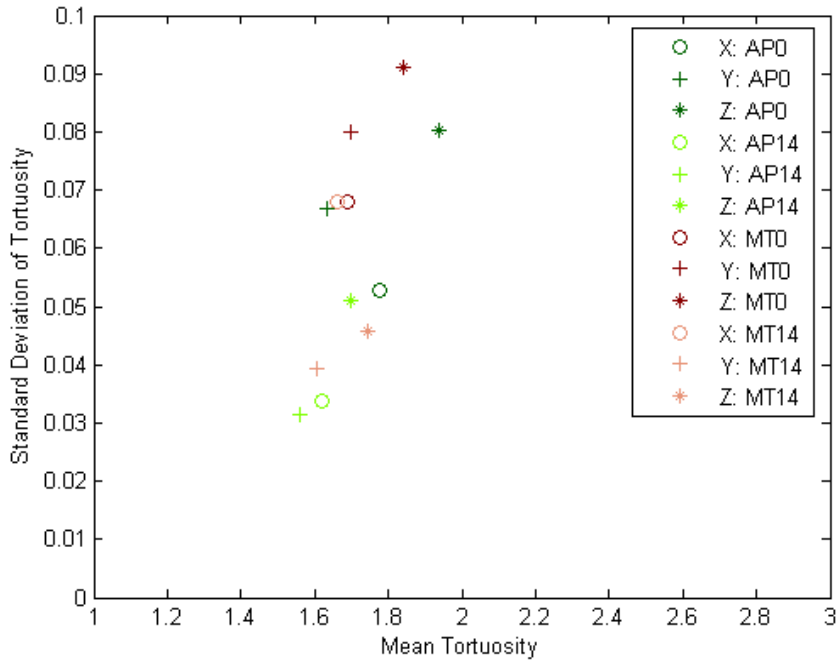


Figure 6.28 Mean Tortuosity vs. Standard Deviation of Tortuosity

Table 6.5 Mean Tortuosity

μ	AP	AP14	MT0	MT14
X	1.776	1.622	1.690	1.623
Y	1.632	1.562	1.697	1.607
Z	1.937	1.697	1.839	1.746

Table 6.6 Standard Deviation of Tortuosity

σ	AP	AP14	MT0	MT14
X	0.053	0.034	0.068	0.068
Y	0.067	0.032	0.080	0.039
Z	0.080	0.051	0.091	0.046

Figure 6.27 shows that for the four samples, the mean tortuosity in z direction is always higher than in the x and y directions. This is due to the 2-D image dilation operation applied on the x-y plane. It can also be observed from the figure that the mean tortuosity in x direction (vertical surfaces) is always higher than the y direction (horizontal surfaces). This may be indicative of the anisotropy of the tortuosity. However at this stage, the tortuosity in z direction (horizontal surfaces) was not compared with the other two directions due to the fact that 2-D image dilation in x-y plane has significant effects on the tortuosity in z direction. This can be observed from the data in the next section when studying the effects of the operations applied on the images. The mean tortuosity of AP0 is higher than MT0 in x and z direction, but always higher than AP14 in any direction. This means the tortuosity decreases with the increasing pore size. MT14 has lower mean tortuosity in any direction than MT0.

Figure 6.28 shows the standard deviation of tortuosity versus mean tortuosity. It can be seen from the figure that the standard deviation of moist tamped specimens are always higher than air pluviated specimens in any direction. Furthermore, the standard deviations of the as-prepared specimens are higher than those of as sheared specimens.

6.6.3 Effects of Dilation Cycles on Tortuosity Measurement

The morphological operations used in this study were 2-D dilations of different number of cycles and 3-D image close. The effects of number of dilation cycles on the structure were studied by comparing the tortuosities that resulted from different number of dilation cycles in the three orthogonal directions. The results for sample AP0 are shown in Figure 6.29. It is observed that when the number of dilation cycles is less than 3, there is no significant effects on the tortuosity in x and y direction. However, the tortuosity increases with the number of cycles dramatically in z direction. Tortuosity comparison between no dilation and 4 cycles of dilation is shown in Table 6.9. It is noted that before dilation is applied, the tortuosity of as-prepared samples is lower than as-sheared samples. However, after 4 cycles dilation, the results are opposite. This means in the dilated sample, the tortuosity decreased.

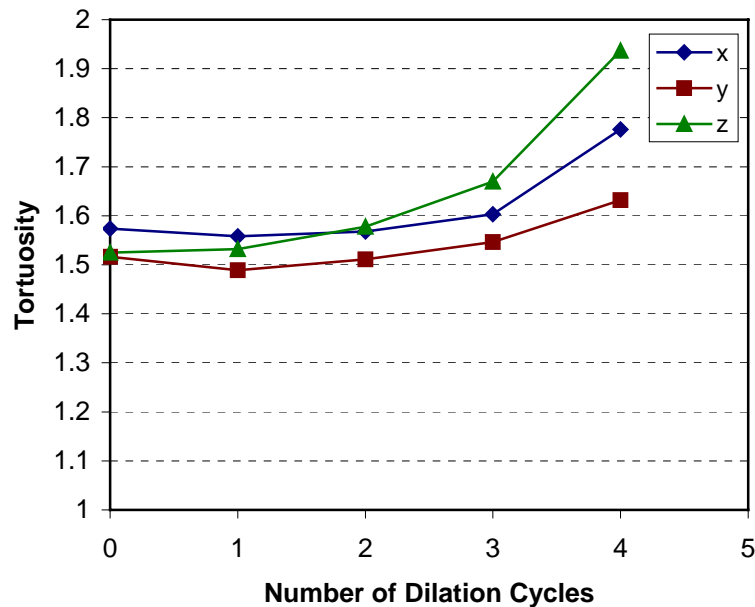


Figure 6.29 Effects of Number of Dilations Cycles on Tortuosity Measurement of AP0

Table 6.7 Tortuosity Comparison

μ	AP0	AP0 (4)	AP14	AP14 (4)	MT0	MT0 (4)	MT14	MT14 (4)
X	1.574	1.776	1.601	1.622	1.551	1.697	1.595	1.623
Y	1.516	1.632	1.539	1.562	1.529	1.69	1.549	1.607
Z	1.525	1.937	1.55	1.697	1.52	1.839	1.55	1.746

Note: AP0, AP14, MT0, and MT14: No dilation applied; AP0 (4), AP14 (4), MT0 (4), and MT14 (4): 4 cycles of dilation and morphological operation applied;

6.7 Effects of Preparation Methods and Shearing on Microstructure

3-D pore size and throat size distribution analysis show that the mean pore size and the mean throat size of moist-tamped specimens are larger than those of air-pluviated specimens, even though the initial global void ratio in the two samples are the same. This is attributed to the preparation-induced variations inside the moist-tamped specimen which resulted in large pores existing in some regions inside the coupon cut from the moist-tamped specimen.

3-D throat size and pore size distribution analyses show that the mean throat size and mean pore size of as-prepared sample AP0 are smaller than that of the as-sheared sample AP14. This is consistent with the corresponding 2-D analysis and with the fact that the global dilation occurred in the air-pluviated specimen during shearing. The mean tortuosity in AP0 is smaller than AP14, which is indicative of tortuosity decreasing with increasing pore size. In other words, the tortuosity in the dilated air-pluviated specimen increased in comparison with the corresponding as-prepared specimen.

3-D throat size and pore size distribution analyses show different results for moist-tamped specimens in comparison with the 2-D results. In 3-D analysis, the mean pore size and mean throat size of MT0 are smaller than those of MT14. However, it is noted that the number of pores in MT14 is larger than in MT0. This is consistent with the

fact that the void ratio of MT14 is larger than MT0. The moist-tamped specimens show different behavior trends than air-pluviated specimens. The factors contributing to this are summarized as follows. AP0 and AP14 coupons were both cut from the center of air-pluviated specimens that should result in more uniform initial structures. However, due to the preparation-induced variations, the moist-tamped specimens are likely to be more dissimilar initially and thus interpretation may be more complicated. These variations may also affect the dilation and image close process applied to the image data before measurement is performed.

CHAPTER VII

SUMMARY, CONCLUSIONS AND RECOMMENDATIONS

7.1 Summary and Conclusions

This is the first study to perform 3-D reconstruction and characterization in sand microstructure of triaxial test specimens. To study the preparation-induced variation and shearing-induced evolution of the structure of triaxial test specimens, two sets of specimens were prepared using air pluviation and moist tamping respectively to similar initial global void ratios. One of the air-pluviated and one of the moist-tamped specimens were preserved at this stage (0% global axial strain) using resin impregnation. The other air-pluviated and moist-tamped specimens were sheared to 14% global axial strain under axial compression loading.

A serial sectioning technique for triaxial tests sand has been successfully implemented to reconstruct the three-dimensional microstructure of actual sand specimens. Each coupon was mounted in a polishing fixture after being extracted from the whole specimen and then subjected to serial grinding and polishing. To obtain a 3-D image dataset that has the same resolution in x, y and z directions, the removal thickness used in this study is the same as the resolution used for 2-D image capturing. This is important for further microstructure analysis in both two-dimensions as well as three-dimensions. At each removal and image capture step, a mosaic technique was applied by capturing a series of 2-D images on a given section with some overlap. While the

process requires significant time and effort, it is relatively inexpensive and effective. In addition, by combining the serial sectioning method with the mosaic technique, it is considered to be the best method currently available to obtain high resolution and large field of view of specimens simultaneously. Three dimensional microstructure models are computationally constructed by assembling the digitally acquired section images. The resulting volumetric model was quantitatively characterized. Individual pore structures and particles were visualized.

The research software package 3DMA was used in this study to characterize the reconstructed structure in three dimensions. Before the program was utilized with the coupons sectioned from the four triaxial test specimens, two simulated structures of idealized sphere packings (simple cubic packing (SCP) and face-centered packing (FCP)), were used to validate the program operation. Furthermore, a series of 2-D analysis were performed on the 2-D slices of the SCP and FCP structures. Results indicate that the program works well on the two-phase structures in which the particles have contacts with each other. Particles which do not overlap (i.e. do not share voxels) lead to computational difficulties in how the program identifies throats and pores. This deficiency led to the need for some image preprocessing, which included 2-D dilation and 3-D morphological closure on the real structures before the program could be utilized to assess the test specimens.

The effects of preparation method on the structure of the specimen were studied by comparing the 2-D pore size, local void ratio, and 2-D throat size of the samples. The entropy of local void ratio distribution, pore size distribution and throat size distribution consistently show that the MT0 specimen has a higher degree of disorder than the AP0

specimen. In addition, the comparison of standard deviation of local void ratio distribution, pore size distribution and throat size distribution between AP0 and MT0 shows high dispersion of each distribution in MT0. Consequently it can be concluded that air-pluviated specimens have more uniform soil structure in terms of pore size, throat size and local void ratio distribution.

Shearing-induced structure evolution was also studied in two dimensions by comparing specimens AP0 and AP14 as well as specimens MT0 and MT14. Both the coupons of AP14 and AP0 used in this study were cut from the center of the whole specimen. AP14 is located in the dilation region of the specimen. This is confirmed by the fact that the void ratio of AP14 is higher than AP0. For the 2-D analysis, pore size, throat size and local void ratio distribution were studied. AP14 always has a larger coefficient of variation than AP0. In addition, from the distribution plots of the three parameters, it can be observed that the distributions shift towards the right and the frequency of peaks decreases as axial strain increases (from 0% to 14%). The void ratio of MT14 is larger than MT0, which confirms it is located in the dilation region inside the whole specimen. The 2-D pore size and throat size distribution curves display similar trend as AP0 and AP14. However, the change in entropy from MT0 to MT14 is less than that from AP0 to AP14, which is consistent with the localization occurring in the MT14 specimen. This is also confirmed by the lower mean pore size and mean throat size of MT14.

3-D pore size and throat size distribution analysis shows that the mean pore size and mean throat size of the moist-tamped specimen are larger than that of the air-pluviated specimen, even though the initial global void ratio in the two samples are the

same. This may be due to the preparation-induced variations inside the moist-tamped specimen which resulted in large pores existing in some regions within the coupon cut from the specimen.

3-D throat size and pore size distribution analyses shows that the mean throat size and mean pore size of as-prepared sample AP0 are smaller than the as-sheared sample AP14. This is consistent with the corresponding 2-D analysis and with the fact that the global dilation occurred in the air-pluviated specimen after shearing. The mean tortuosity in AP0 is smaller than AP14, thus it can also be concluded that tortuosity decreases with increasing pore size. In other words, the tortuosity in the dilated air-pluviated specimen increased in comparison to the corresponding as-prepared specimen.

3-D throat size and pore size distribution analyses show different results for moist-tamped specimens in comparison with 2-D results. In 3-D analysis, the mean pore size and mean throat size of MT0 are smaller than those of MT14. However, it is noted that the number of pores in MT14 is larger than in MT0. This is consistent with the fact that the void ratio of MT14 is larger than MT0. Moist-tamped specimens show different behavior from air-pluviated specimens. The factors contributing to this are summarized as follows. AP0 and AP14 coupons were both cut from the center of the specimen since air-pluviation results in more uniform initial structures, the results are likely to be comparable. However, due to the preparation-induced variations (such as layering), analysis of the response of moist-tamped specimens is more complicated. In addition, even though sample MT14 is not located in the shear band, it is close to where localization occurred. This might be the reason that it is showing some structure evolution behavior that 2-D analysis did not capture. Tortuosity analysis of MT14 and

MT0 shows that in the dilated specimen that corresponds to larger void ratio, the tortuosity decreases with increasing void ratio.

In addition to 3-D pore size, throat size and tortuosity that can be measured from the 3-D reconstructed microstructure, pore structure parameters such as, contact number, connectivity and genus can also be obtained. By integrating these parameters into the models for predicting hydraulic conductivity of porous media, it is possible to predict the hydraulic properties of soils based on the pore structure parameters quantified from the 3-D reconstructed microstructure.

7.2 Recommendations

As demonstrated in this research, it is quite complicated to develop/apply algorithms that can be used to quantify the real microstructure of pore space in three dimensions. This is also essential to extracting data from the reconstructed structure. There are a lot of issues involved, such as memory usage, algorithm efficiency and accuracy. Medial axis analysis itself is a good tool that captures the 3-D structure characteristics with a simplified structure. However, additional effort is needed to improve the algorithm logic so that it can quantify the structure correctly and efficiently. Memory usage is a common issue when dealing with large 3-D data. Even with the rapid advancements in computer hardware, it is still important to develop algorithms that can either simplify the problem or process the data in an efficient manner.

In this study, particle characterization in 3-D is limited by the fact that some particles are touching while others are not. A good algorithm is needed to segment the particles in 3-D such that particle size and orientations can be measured. Current 2-D or

3-D available segmentation algorithms work well for spherical shape objects. Even though the sand particles used in this study are mostly rounded or sub-rounded, errors still occur when applying such algorithms to segment the particles.

Only one coupon was cut from each specimen in this study. It is possible to study the whole specimen by taking several coupons from different locations of interests. On particular, for shear band study, using several coupons taken adjacent to the shear band as well as right through the shear band may help further study of localization in moist tamped specimens.

REFERENCES

- Abràmoff, M. (2004). "Bio-Medical Imaging in Java." <http://bij.isi.uu.nl/>.
- Ammann, J. J., Hein, L. R. and Nazar, A. M. (1996). "Three-Dimensional Reconstruction of Fracture Surface." Materials Characterization, 36: 379-386.
- Baldwin, C. A., Sederman, A. J., Mantle, M. D., Alexander, P. and Gladden, L. F. (1996). "Determination and Characterization of the Structure of a Pore Space from 3D Volume Images." Journal of Colloid and Interface Science, 181: 79-92.
- Brey, E. M., King, T. W., Johnston, C., McIntire, L. V., Reece, G. P. and Patrick, C. W. J. (2002). "A Technique for Quantitative Three-Dimensional Analysis of Microvascular Structure." Microvascular Research, 63: 279-294.
- Bryon, D. N., Atherton, M. P. and Hunter, R. H. (1995). "The Interpretation of Granitic Textures from Serial Thin Sectioning, Image Analysis and Three-Dimensional Reconstruction." Mineralogical Magazine, 59: 203-211.
- Bystrzycki, J. and Prezetakiewicz, W. (1992). "3-Dimensional Reconstruction of Annealing Twins Shape in FCC Metals by Serial Sectioning." Scripta Materialia, 27: 893-896.
- Chawla, N., Ganesh, V. V. and Wunsch, B. (2004). "Three-Dimensional (3D) Microstructure Visualization and Finite Element Modeling of the Mechanical Behavior of Sic Particle Reinforced Aluminum Composites." Scripta Materialia, 51: 161-165.
- Chen, C.-C. (2000). Shear Induced Evolution of Structure in Water-Deposited Sand Specimens. School of Civil and Environmental Engineering. Georgia Institute of Technology. Atlanta, GA, Ph.D. Dissertation: 497pp
- Coles, M. E., Hazlett, R. D., Spanne, P., Soll, W. E., Muegge, E. L. and Jones, K. W. (1998). "Pore Level Imaging of Fluid Transport Using Synchrotron X-Ray Microtomography." Journal of Petroleum Science and Engineering, 19: 55-63.
- Cooper, D. M. L., Turinsky, A. L., Sensen, C. W. and Hallgrimsson, B. (2003). "Quantitative 3d Analysis of the Canal Network in Cortical Bone by Micro-Computed Tomography." The Anatomical Record (Part B: New Anat.), 274B: 169-179.
- Delerue, J.-F., Perrier, E., Yu, Z. Y. and Velde, B. (1999). "New Algorithm in 3D Image Analysis and Their Application to the Measurement of a Spatialized Pore Size Distribution in Soils." Phys. Chem. Earth (A), 24(7): 639-644.

Denison, C., Carlson, W. D. and Ketcham, R. A. (1997). "Three-Dimensional Quantitative Textural Analysis of Metamorphic Rocks Using High-Resolution Computed X-Ray Tomography: Part I. Methods and Techniques." Journal of Metamorphic Geology, 15(1): 29-44.

Dowd, B. A., Campbell, G. H., Marr, R. B., Nagarkar, V., Tipnis, S., Axe, L. and Siddons, D. P. (1999). Developments in Synchrotron X-Ray Computed Microtomography at the National Synchrotron Light Source. SPIE Conference on Developments in X-Ray Tomography II, Denver, Colorado, SPIE

Dullien, F. A. L. (1992). Porous Media: Fluid Transport and Pore Structure. Academic Press, Inc., San Diego, CA.

Fisher, R., Perkins, S., Walker, A. and Wolfart, E. (2003). "Morphology - Skeletonization/Medial Axis Transform." 2005, from <http://homepages.inf.ed.ac.uk/rbf/HIPR2/skeleton.htm>.

Fredrich, J. T. (1999). "3D Imaging of Porous Media Using Laser Scanning Confocal Microscopy with Application to Microscale Transport Processes." Physics and Chemistry of the Earth Part A: Solid Earth and Geodesy, 24(7): 551-561.

Frost, J. D. (1989). Studies on the Monotonic and Cyclic Behaviors of Sand. Purdue University. Ph. D. Dissertation:

Frost, J. D. and Jang, D.-J. (2000). "Evolution of Sand Microstructure During Shearing." Journal of Geotechnical and Geoenvironmental Engineering, 126(2): 116-130.

Frost, J. D. and Kuo, C.-Y. (1996). "Automated Determination of the Distribution of Local Void Ratio from Digital Images." Geotechnical Testing Journal, 19(2): 107-117.

Frost, J. D. and Park, J. Y. (2003). "A Critical Assessment of the Moist Tamping Technique." Geotechnical Testing Journal, 26(1): 57-70.

Herman, S., Timmerman, A., Vanderborght, J. and Feyen, J. (2002). Quantitative Characterization of the Pore Network and Soil Structure Using Microfocus X-Ray Computer Tomography. 17th WCSS, Thailand.

Ismail, S. N. A. (1975). "Micromorphometric Soil Porosity Characteristics by Means of Electro-Optical Image Analysis (Quantimet 720)." Soil Survey Papers, 9.

Jang, D.-J. (1997). Quantification of Sand Structure and Its Evolution During Shearing Using Image Analysis. School of Civil and Environmental Engineering. Georgia Institute of Technology. Atlanta, Ph.D. Dissertation: 259pp

Ketcham, R. A. and Carlson, W. D. (2001). "Acquisition, Optimization and Interpretation of X-Ray Computed Tomographic Imagery: Applications to the Geosciences." Computers and Geosciences, 27: 381-400.

Kriete, A., Ed. (1992). Visualization in Biomedical Microscopies: 3-D Imaging and Computer Applications. New York, NY, USA, VCH Verlagsgesellschaft, Weinheim (Federal Republic of Germany).

Kuo, C.-Y. (1994). Quantifying the Fabric of Granular Materials an Image Analysis Approach. School of Civil and Environmental Engineering. Georgia Institute of Technology. Atlanta, Ph.D. Dissertation: 254pp

Kuo, C. Y. and Frost, J. D. (1995). Quantifying the Fabric of Granular Materials - an Image Analysis Approach. Atlanta, GA, Georgia Institute of Technology.

Ladd, R. S. (1978). "Preparing Test Specimens Using Undercompaction." Geotechnical Testing Journal, GTJODJ, 1(1): 16-23.

Li, M., Ghosh, S., Richmond, O., Weiland, H. and Rouns, T. H. (1998). "Three-Dimensional Characterization and Modeling of Particle Reinforced Metal Matrix Composites Part I: Quantitative Description of Microstructural Morphology" Materials Science and Engineering, A265: 153-173.

Li, M., Ghosh, S., Rouns, T. N., Weiland, H., Richmond, O. and Hunt, W. (1998). "Serial Sectioning Method in the Construction of 3-D Microstructures for Particle-Reinforced Mmcs." Materials Characterization, 41: 81-95.

Lichtenbelt, B., Crane, R. and Naqvi, S. (1998). Introduction to Volume Rendering. Prentice Hall PTR, Upper Saddle River, NJ.

Lin, C. and Cohen, M. H. (1982). "Quantitative Methods for Microgeometric Modeling." Journal of Applied Physics, 53(6): 4152-4165.

Lin, C. L. and Miller, J. D. (2004). "Pore Structure Analysis of Particle Beds for Fluid Transport Simulation During Filtration." Int. J. Miner. Process., 73: 281-294.

Lindquist, W. B. (1999). 3DMAGeneral Users Manual, State University of New York, Stony Brook.

Lindquist, W. B. (2001). "Network Flow Model Studies and 3d Pore Structure." Contemporary Mathematics, 76S04: 1-12.

Lindquist, W. B. (2005). Personal Communication

- Lindquist, W. B. and Lee, S.-M. (1996). "Medial Axis Analysis of Void Structure in Three-Dimensional Tomographic Images of Porous Media." Journal of Geophysical Research, 101(B4): 8297-8310.
- Lindquist, W. B. and Venkatarangan, A. (1999). "Investigating 3d Geometry of Porous Media from High Resolution Images." Physics and Chemistry of the Earth (A), 25: 593-599.
- Lund, A. C. and Voorhees, P. W. (2003). "A Quantitative Assessment of the Three-Dimensional Microstructure of a γ - γ' Alloy." Philosophical Magazine, 83(14): 1719-1733.
- Lymberopoulos, D. P. and Payatakes, A. C. (1991). "Derivation of Topological, Geometrical, and Correlational Properties of Porous Media from Pore-Chart Analysis of Serial Section Data." Journal of Colloid and Interface Science, 150(1): 61-79.
- Maire, E., Fazekas, A., Salvo, L., Dendievel, R., Youssef, S., Cloetens, P. and Letang, J. M. (2003). "X-Ray Tomography Applied to the Characterization of Cellular Materials. Related Finite Element Modeling Problems." Composites Science and Technology, 63: 2431-2443.
- Mangan, M. A., Lauren, P. D. and Shiflet, G. J. (1997). " Three-Dimensional Reconstruction of Widmanstätten Plates in Fe-12.3mn-0.8c." Journal of Microscopy, 188(1): 36-41.
- Marschallinger, R. (1998). "A Method for Three-Dimensional Reconstruction of Macroscopic Features in Geological Materials." Computer and Geosciences, 24(9): 875-883.
- Menendez, B., David, C. and Nistal, A. M. (2001). "Confocal Scanning Laser Microscopy Applied to the Study of Pore and Crack Networks in Rocks." Computer and Geosciences, 27: 1101-1109.
- Mitchell, J. K., Chatoian, J. M. and Carpenter, G. C. (1976). The Influence of Sand Fabric on Liquefaction Behavior. Report to U.S. Army Corps of Engineers of Engineers Waterways Experiment Station. Vicksburg, Miss.
- Moran, C. J. and McBrantney, A. B. (1992). "Acquisition and Analysis of Three Component Digital Images of Soil Pore Structure." Journal of Soil Sciences, 43: 541-549.
- Moreau, E., Velde, B. and Terribile, F. (1999). "Comparison of 2D and 3D Images of Fractures in a Vertisol." Geoderma, 92: 55-72.
- Mulilis, J. P., Seed, H. B., Chan, C. K., Mitchell, J. K. and Arulanandan, K. (1977). "Effects of Sample Preparation on Sand Liquefaction." Journal of Geotechnical Engineering Division, ASCE, 103(GT2): 91-107.

Oda, M. (1976). Fabrics and Their Effects on the Deformation Behavior of Sand. Special Issue. Japan, Department of Foundation Engineering, Faculty of Engineering, Saitama University.

Odgaard, A., Andersen, K., Melsen, F. and Gundersen, H. J. G. (1990). "A Direct Method for Fast Three-Dimensional Serial Reconstruction." Journal of Microscopy, 159: 335-342.

Oren, P.-E. and Bakke, S. (2003). "Reconstruction of Berea Sandstone and Pore-Scale Modeling of Wettability Effects." Journal of Petroleum Science and Engineering, 39: 177-199.

Park, J. Y. (1999). A Critical Assessment of Moist Tamping and Its Effect on the Initial and Evolving Structure of Dilatant Triaxial Specimens. School of Civil and Environmental Engineering. Georgia Institute of Technology. Atlanta, Ph.D. Dissertation: 384pp

Perret, J., Prasher, S. O., Kantzas, A. and Langford, C. (1999). "Three-Dimensional Quantification of Macropore Networks in Undisturbed Soil Cores." Soil Sci. Soc. AM. J., 63: 1530-1543.

Prodanovic, M. (2005). Fluid Displacement in Rock Cores: A Study Based on Three Dimensional X-Ray Microtomography Images. Department of Applied Mathematics and Statistics. State University of New York, Stony Brook. Ph.D. Dissertation: 123

Ringrose-Voase, A. J. and Bullock, P. (1984). "The Automatic Recognition and Measurement of Soil Pore Types by Image Analysis and Computer Programs." Journal of Soil Sciences, 35: 673-684.

Russ, J. C. (1995). The Image Processing Handbook. CRC Press, Boca Raton, FL.

Shin, H. K. (2002). A Throat Construction Algorithm for Medial Axis Analysis of 3d Images of Vesiculated Basalts. Department of Applied Mathematics and Statistics. State University of New York, Stony Brook. Ph.D. Dissertation: 95

Singh, H. and Gokhale, A. M. (2005). "Visualization of Three-Dimensional Microstructures." Materials Characterization, 54(1): 21-29.

Spowart, J. E., Mullens, H. M. and Puchala, B. T. (2003). "Collecting and Analyzing Microstructures in Three Dimensions: A Fully Automated Approach." Journal of Microscopy, 55(10): 35-37.

Streicher, J., Weninger, W. J. and Muller, G. B. (1997). "External Marker-Based Automatic Congruencing: A New Method of 3D Reconstruction from Serial Sections." The Anatomical Record, 248: 583-602.

- Sutton, M. D., Briggs, D. E. G., Siveter, D. J. and Siveter, D. J. (2001). "Methodologies for the Visualization and Reconstruction of Three-Dimensional Fossil from the Silurian Herefordshire Lagerstätte." Palaeontologia Electronica, 4(1): 1-17.
- Tewari, A. (1999). Effect of Micro-Gravity on the Microstructural Evolution During Liquid Phase Sintering Materials Sciences and Engineering. Georgia Institute of Technology. Atlanta, Ph.D. Dissertation: 271pp
- Tewari, A. and Gokhale, A. M. (2000). "Application of Three-Dimensional Digital Image Processing for Reconstruction of Microstructural Volume from Serial Sections." Materials Characterization, 44: 259-269.
- Tsakiroglou, C. D. and Payatakes, A. C. (2000). "Characterization of the Pore Structure of Reservoir Rocks with the Aid of Serial Sectioning Analysis, Mercury Porosimetry and Network Simulation." Advances in Water Resources, 23: 773-789.
- Underwood, E. E. (1970). Quantitative Stereology. Addison Wesley, Reading, MA.
- Vogel, H. J. (1997). "Morphological Determination of Pore Connectivity as a Function of Pore Size Using Serial Sections." European Journal of Soil Science, 48: 365-377.
- Vogel, H. J. and Roth, K. (2001). "Quantitative Morphology and Network Representation of Soil Pore Structure." Advances in Water and Resources, 24: 233-242.
- Walker, P. J. C. and Trudgil, S. T. (1983). "Quantimet Image Analysis of Soil Pore Geometry: Comparison with Tracer Breakthrough Curves." Earth Processes and Landforms, 8: 465-472.
- Wong, Y. M., Thompson, R. P., Cobb, L. and Fitzharris, T. (1983). "Computer Reconstruction of Serial Sections." Computers and Biomedical Research, 16: 580-586.
- Yang, C.-T. (2002). Boundary Condition and Inherent Stratigraphic Effects on Microstructure Evolution in Sand Specimens. School of Civil and Environmental Engineering. Georgia Institute of Technology. Atlanta, GA, Ph. D. Dissertation: 522pp
- Yanuka, M., Dullien, F. A. L. and Elrick, D. E. (1984). "Serial Sectioning and Digitization of Porous Media for Two- and Three-Dimensional Analysis and Reconstruction." Journal of Microscopy, 135(2): 159-168.
- Yanuka, M., Dullien, F. A. L. and Elrick, D. E. (1986). "Percolation Processes and Porous Media: I. Geometrical and Topological Model of Porous Media Using a Three-Dimensional Joint Pore Size Distribution." Journal of Colloid and Interface Science, 112(1): 24-41.

Zhao, H. Q., MacDonald, I. F. and Kwiecien, M. J. (1994). "Multi-Orientation Scanning: A Necessity in the Identification of Pore Necks in Porous Media by 3-D Computer Reconstruction from Serial Section Data." Journal of Colloid and Interface Science, 162: 390-401.